

Design of High-Performance, Dual-Motor Liquid-Cooled,
Linear Series Elastic Actuators
for a Self-Balancing Exoskeleton

John Thomas Kendrick

Thesis submitted to the faculty of the Virginia Polytechnic Institute and State University in
partial fulfillment of the requirements for the degree of

Master of Science

In

Mechanical Engineering

Alan T. Asbeck, Chair

Robert L. West

Alfred L. Wicks

23 February 2018

Blacksburg, VA

Keywords: Linear Series Elastic Actuator, Liquid Cooling, Gait Analysis, Mechanical Design,
Finite Element Analysis, Bolted Joint Analysis, Humanoid Robot, Exoskeleton

Design of High-Performance, Dual-Motor Liquid-Cooled, Linear Series Elastic Actuators for a Self-Balancing Exoskeleton

John Thomas Kendrick

Abstract

As a valuable asset in human augmentation and medical rehabilitation, exoskeletons have become a major area for research and development. They have shown themselves to be effective tools for training and rehabilitation of individuals suffering from limited mobility. However, most exoskeletons are not capable of balancing without the assistance of crutches from the user. Leveraging technology and techniques developed for force controlled humanoid robots, a project was undertaken to develop a fully self-balancing, compliant lower-body robotic exoskeleton. Due to their many beneficial features, series elastic actuators were utilized to power the joints on the exoskeleton. This thesis details the development of four linear series elastic actuators (LSEA) as part of this project. All 12-degrees of freedom will be powered by one of these four LSEA's. Actuator requirements were developed by examining human gait data and three robot-walking simulations. These four walking scenarios were synthesized into one set of power requirements for actuator development. Using these requirements, analytical models were developed to perform component trade studies and predict the performance of the actuator. These actuators utilize high-efficacy components, parallel electric motors, and liquid cooling to attain high power-to-weight ratios, while maintaining a small lightweight design. These analyses and trade studies have resulted in the design of a dual-motor liquid-cooled actuator capable of producing a peak force 8500N with a maximum travel speed of 0.267m/s, and three different single-motor actuators capable of producing forces up to 2450N continuously, with a maximum travel speeds up to 0.767m/s.

Design of High-Performance, Dual-Motor Liquid-Cooled, Linear Series Elastic Actuators for a Self-Balancing Exoskeleton

John Thomas Kendrick

General Audience Abstract

Patients who suffer a severe back injury that results in paralysis from the waist down (paraplegia) commonly regain mobility in their daily lives by using a wheelchair. However, staying in a seated position for long periods can cause serious medical issues to arise. In order to address these issues, lower-body exoskeletons have been developed to help patients walk again. Exoskeletons are mechanical devices a person can wear to enhance their physical strength or endurance beyond their normal capability. These exoskeletons have shown themselves to be effective tools for training and rehabilitation of individuals suffering from limited mobility.

However, most exoskeletons are not capable of balancing the user while they walk. In order to maintain balance, the user must hold themselves up with crutches. As with a wheelchair, heavy dependence on crutches can lead to new medical issues for the patient. To solve this problem, technology and techniques created for humanoid robots were used to develop a fully self-balancing exoskeleton. This exoskeleton is known as the Orthotic Lower-body Locomotion Exoskeleton. This thesis details the development of four actuators to power all twelve joints of the exoskeleton. These actuators utilize high-efficiency components, multiple electric motors, and liquid cooling to maintain a small lightweight design and while obtaining very high-power outputs.

Table of Contents

Abstract	ii
General Audience Abstract	iii
Table of Contents	iv
List of Figures	vi
List of Equations	x
List of Tables	xii
List of Acronyms	xiv
1. Introduction	1
1.1. Overview/Motivation	2
1.1.1. Exoskeletons	3
1.1.2. Humanoid Research at Virginia Tech	4
1.1.3. Series Elastic Actuation	5
1.2. Thesis Organization	6
2. Exoskeleton Requirements Development	7
2.1. Walking Data Analysis	8
2.1.1. Human Gait Data	9
2.1.2. Humanoid Robot Walking Data	12
2.2. Joint Data Synthesis and Actuator Requirements	14
3. Series Elastic Actuator Component Selection	15
3.1. Motor Selection	15
3.1.1. Force Cooling DC Electric Motors	16
3.1.2. Determining Maximum Continuous Current	17
3.2. Gearing and Drivetrain Selection	20
3.2.1. Ball Screw Analysis	21
3.2.2. Two-Bar Linkage Analysis	22
3.2.3. Ball Screw Analysis	23
3.2.4. Drivetrain selection	25
3.3. Final Configuration Selection and Performance Analysis	27

4.	Elastic Element Analysis and Design	31
4.1.	Coil Spring Analysis	32
4.2.	Leaf Spring Analysis	33
4.3.	Spring Selection	37
4.4.	Finite Element Analysis and Finalized Design of Leaf Springs	37
4.4.1.	MKIV and MKIII Lite Spring	38
4.4.2.	MKIII Heavy Spring	42
4.5.	Spring Stiffness Analysis	44
4.6.	Comparison of Analytical Model and FEA	51
5.	Linear Series Elastic Actuator Mechanical Design	56
5.1.	Bearing and Transmission Housing Assembly	60
5.1.1.	Bearing Stack	62
5.1.2.	Overhung load analysis	64
5.1.3.	Belt Tensioning	66
5.2.	Cooling Jacket Assembly	68
5.2.1.	Jacket Design	70
5.2.2.	O-ring and Gasket Design	71
5.3.	Load Bearing Tube Assembly	74
5.4.	U-Joint and Yoke Assembly	75
5.5.	Fastener Analysis	76
6.	Conclusion	80
6.1.	Recommendations	81
6.2.	Future Work	84
	References	86
	Appendix A	92
	Appendix B	105
	Appendix C	111

List of Figures

Figure 1: Mihailo Pupin Exoskeleton [16], Hardiman [17], BLEEX [1], HAL-5 [18]	3
Figure 2: OLL-E High Level Work Breakdown Structure	7
Figure 3: DoF Naming Convention and Locations	8
Figure 4: Human Gait Phases [80]	9
Figure 5: 140kg Human Joint Velocity, Torque, and Power for One Gait Cycle	10
Figure 6: Joint Power Visualization for Human Knee	11
Figure 7: Heat Transfer Coefficients for various cooling methods and coolants [83]	16
Figure 8: Two-Bar Linkage Free-Body Diagram	22
Figure 9: Gear Train Solutions Matrix Color-Code to Display Viable Solutions	25
Figure 10: Knee Actuator Gear Train Combinations Solution Matrix	26
Figure 11: Performance Diagram for a Liquid Cooled Dual Motor LSEA (MKIII Heavy)	29
Figure 12: Performance Diagram for a Liquid Cooled Single Motor LSEA (MKIII Lite)	29
Figure 13: Performance Diagram for a LSEA with a Planetary Gear Box (MKIV Gear)	30
Figure 14: Validation of Knee Joint Requirements and MKIII Heavy Actuator Performance	30
Figure 15: Custom Bi-Directional Coil Spring by Helical	32
Figure 16: Shear Moment Diagrams for Leaf Spring in Pure Bending and Shear Loading	33
Figure 17: Free-Body Diagram of Cantilever Beam with Lever Arm	35
Figure 18: Exploded view of MKIV Spring Assembly	38
Figure 19: ABAQUS FEA Model of MKIV Spring Assembly	39
Figure 20: Deflection at U-Joint Center under $\pm 4800\text{N}$ Loading	40
Figure 21: von Mises Stress under $\pm 4800\text{N}$ Loading	40
Figure 22: Max Principal Stress under $\pm 4800\text{N}$ Loading	40
Figure 23: Stress Concentrations on MKIV Spring	41

Figure 24: ABAQUS FEA Model of MKIII Spring Assembly	42
Figure 25: Deflection at U-Joint Center under $\pm 7000\text{N}$ Loading	43
Figure 26: von Mises Stress under $\pm 7000\text{N}$ Loading	43
Figure 27: Max Principal Stress under $\pm 7000\text{N}$ Loading	43
Figure 28: Stress Concentrations on MKIII Spring	44
Figure 29: Deflection Path and Spring Stiffness of MKIII Spring due to $\pm 7000\text{N}$ Loading.....	45
Figure 30: Deflection Path and Spring Stiffness of MKIV Spring due to $\pm 4800\text{N}$ Loading.....	45
Figure 31: Free Body Diagram of Actuator and Parallel Leaf Spring	46
Figure 32: MKIII Spring Deflection Given Input Load and Angle	47
Figure 33: MKIV Spring Deflection Given Input Load and Angle.....	47
Figure 34: MKIII Spring Stiffness Given Input Load and Angle	48
Figure 35: MKIV Spring Stiffness Given Input Load and Angle.....	48
Figure 36: MKIII Bending Stress Given Input Load and Angle	49
Figure 37: MKIV Bending Stress Given Input Load and Angle	49
Figure 38: Deflection of Bolted Joint at the Base of the MKIV and MKIII Springs	52
Figure 39: Bending Stress in Active Span of MKIV Spring	53
Figure 40: Bending Stress in Active Span of MKIII Spring.....	53
Figure 41: Model Comparison of Magnitude of Deflection versus Input Angle.....	54
Figure 42: Model Comparison of Maximum Stress versus Input Angle	55
Figure 43: Overview of the Four LSEA's for the OLL-E Exoskeleton.....	56
Figure 44: Component Overview of the MKIII Heavy LSEA	57
Figure 45: Component Overview of the MKIV Geared LSEA	57
Figure 46: Upper and Lower Housings of the MKIII Heavy and MKIII Lite	60

Figure 47: Cross-section View of Actuator Bearing and Transmission Assembly Showing Compression and Tension Load Paths	61
Figure 48: Ball Screw Bearing Stack Configuration	62
Figure 49: Installation of Bearing Components (Left) and Thrust Nut (Right).....	63
Figure 50: Free Body Diagrams of Overhung Load and Load Connection Factor	64
Figure 51: Integral Dual Support Design for Drive Pulley.....	65
Figure 52: Belt Tensioner Designs for Single and Dual Motor Actuators	66
Figure 53: Belt Tensioner Components for Single Motor and Dual Motor Actuators	67
Figure 54: Cooling Jacket Component Overview.....	68
Figure 55: Cooling Jacket Mount and Seal Integration into Housing	69
Figure 56: Cooling Jacket Flow Path (Left), Open Design (Center), and Fin Design (Right)	70
Figure 57: Cross-Section of Fined Cooling Jacket and Lower Housing	71
Figure 58: O-Ring Calculation Diagram.....	72
Figure 59: Cross Section Load Bearing Tube (Left) Comparison to Prior Design (Right)	74
Figure 60: U-Joint and Yoke Assembly.....	75
Figure 61: Characteristic Dimension of Metric Thread.....	77
Figure 62: OLL-E Hip Joints Incorporating MKIV LSEA's and Hardware Backpack	80
Figure 63: Ball Screw Lower Bearing Fitment Issues (Left) Honing of Inner Race (Right)	81
Figure 64: Significant Play Found In U-Joint Trunnion and Bearing	82
Figure 65: Load Cell Integrate Into U-Joint for Reduced Length [41].....	82
Figure 66: Early Aluminum Prototype (Left) Finalized Design Prototype (Right).....	83
Figure 67: Custom Actuator Test Stand with MKIII Lite Mounted	84
Figure 68: Custom Motor Dynamometer and Liquid Cool Jacket Test Stand	85

Appendix A

Figure A 1: Summary of Human Gait Data 92

Figure A2: ESCHER Left Leg Data Walking at 0.48 m/s..... 93

Figure A3: ESCHER Left Leg Data Walking at 0.48 m/s..... 94

Figure A4: ESCHER Right Leg Data Walking at 0.48 m/s..... 95

Figure A5: ESCHER Right Leg Data Walking at 0.48 m/s..... 96

Figure A6: ESCHER Left Leg Data Walking at 0.20 m/s..... 97

Figure A7: ESCHER Left Leg Data Walking at 0.20 m/s..... 98

Figure A8: ESCHER Right Leg Data Walking at 0.20 m/s..... 99

Figure A9: ESCHER Right Leg Data Walking at 0.20 m/s..... 100

Figure A10: ESCHER Left Leg Data Walking Up Stairs..... 101

Figure A11: ESCHER Left Leg Data Walking Up Stairs..... 102

Figure A12: ESCHER Right Leg Data Walking Up Stairs 103

Figure A13: ESCHER Right Leg Data Walking Up Stairs 104

Appendix C

Figure C1: Brushless Motor Comparison Table 111

List of Equations

(2.1).....	8
(3.1).....	17
(3.2).....	18
(3.3).....	18
(3.4).....	18
(3.5).....	18
(3.6).....	18
(3.7).....	21
(3.8).....	21
(3.9).....	21
(3.10).....	22
(3.11).....	22
(3.12).....	22
(3.13).....	23
(4.1).....	31
(4.2).....	34
(4.3).....	34
(4.4).....	34
(4.5).....	35
(4.6).....	35
(4.7).....	35
(4.8).....	35
(4.9).....	35
(4.10).....	35
(4.11).....	35
(4.12).....	35
(4.13).....	35
(4.14).....	35

(4.15).....	36
(4.16).....	36
(5.1).....	64
(5.2).....	64
(5.3).....	65
(5.4).....	73
(5.5).....	73
(5.6).....	73
(5.7).....	77
(5.8).....	77
(5.9).....	78
(5.10).....	78
(5.11).....	78
(5.12).....	78
(5.13).....	78
(5.14).....	78
(5.15).....	78
(5.16).....	79
(5.17).....	79
(5.18).....	79

List of Tables

Table 1: Summary of 140kg Human Gait Peak Values	12
Table 2: Summary of Peak Values of 140kg ESCHER Walking at 0.48m/s Simulation.....	13
Table 3: Summary of Peak Values of 140kg ESCHER Walking at 0.02m/s Simulation.....	13
Table 4: Summary of Peak Values of 140kg ESCHER Waking Up Stairs Simulation.....	13
Table 5: Synthesis of Human and Humanoid Peak Data Points.....	14
Table 6: Theoretical Maximum Continuous Current and Power of Maxon Motors.....	19
Table 7: Ball Screw Static Load Safety Factor	23
Table 8: Ball Screw Permissible Axial Load	24
Table 9: Ball Screw Dangerous Rotational Speed	24
Table 10: Summary of Actuator Designs and Joint Locations	27
Table 11: Helical Bidirectional Coil Spring Properties	33
Table 12: Material Properties of Titanium Ti-6Al-4V (Grade 5), Annealed [97].....	36
Table 13: Leaf Spring Properties under 4400N Load.....	36
Table 14: MKIV Spring FEA Results.....	41
Table 15: MKIII Spring FEA Results.....	42
Table 16: MKIV Spring Model Results Comparisons.....	51
Table 17: MKIII Spring Model Results Comparisons.....	51
Table 18: Comparison of Linear SEA's from SAFFiR, THOR, ESCHER, and OLL-E.....	59
Table 19: Bearings Used in all MKIII and MKIV Actuators	62
Table 20: Overhung Load Results for Actuator Drive Components.....	65
Table 21: O-ring Calculation Dimensions and Tolerances.....	72
Table 22: O-Ring Calculation Results	73
Table 23: Torque Factors K_t [89].....	79

Appendix B

Table B1: 140kg Human Gait Peak Power and Corresponding Values	105
Table B2: 140kg Human Gait Peak Torque and Corresponding Values	105
Table B3: 140kg Human Gait Peak Velocity and Corresponding Values.....	105
Table B4: Peak Power, 140kg ESCHER Walking at 0.48 m/s.....	106
Table B5: Peak Torque, 140kg ESCHER Walking at 0.48 m/s.....	106
Table B6: Peak Velocity, 140kg ESCHER Walking at 0.48 m/s	107
Table B7: Peak Power, 140kg ESCHER Walking at 0.20 m/s.....	107
Table B8: Peak Torque, 140kg ESCHER Walking at 0.20 m/s.....	108
Table B9: Peak Velocity, 140kg ESCHER Walking at 0.20 m/s	108
Table B 10: Peak Power, 140kg ESCHER Walking Up Stairs.....	109
Table B 11: Peak Torque, 140kg ESCHER Walking Up Stairs	109
Table B 12: Peak Velocity, 140kg ESCHER Walking Up Stairs	110

List of Acronyms

Acronym	Definition
CAD	Computer Aided Design
CAE	Computer Aided Engineering
DARPA	Defense Advanced Research Projects Agency
DC	Direct Current
DoF	Degrees of Freedom
ESCHER	Electric Series Compliant Humanoid for Emergency Response
FEA	Finite Element Analysis
ISO	International Organization for Standardization
LSEA	Linear Series Elastic Actuators
NEMA	National Electrical Manufactures Association
NSF	National Science Foundation
OHL	Overhung Load
OLL-E	Orthotic Lower-body Locomotion Exoskeleton
OTS	Off the Shelf
SAFFiR	Shipboard Autonomous Firefighting Robot
SCI	Spinal Cord Injury Patients
SEA	Series Elastic Actuator
THOR	Tactical Hazardous Operations Robot

1. Introduction

As the field of robotics expands, exoskeletons for human augmentation and medical rehabilitation have come to the forefront of research and development. Systems such as the Berkeley Lower Extremity Exoskeleton (BLEEX) developed at the University of California, Berkeley, increases a user's strength and endurance for carrying heavy loads while walking [1]. This work would later culminate in development of the Human Universal Load Carrier (HULC™) for the U.S. Military by Lockheed Martin and Berkeley Bionics [2]. HULC™, along with Raytheon Sarcos XOS [3], were developed under the Defense Advanced Research Projects Agency (DARPA) Exoskeletons for Human Performance Augmentation program. These exoskeletons and others like them, focus on enhancing the capability of a physically fit and healthy user. These systems are mainly targeted for military and industrial applications.

In addition to growth in defense and industry, rapid growth of exoskeleton development in the medical industry has occurred as well. Devices and systems have been developed to help spinal cord injury (SCI), stroke patients, and those with limited mobility. Systems such as Lokomat [4] utilize an exoskeleton attached to a treadmill for physical therapy and rehabilitation in hospitals. Assistive devices have helped improve the health and quality of life of patients with a SCI or limited mobility. A few prominent examples of assistive devices on the market today are Rex [5], ReWalk™ [6], HAL [7], and Ekso™ [8]. These exoskeletons attach to the legs of the patient and move them in a walking motion. However, these exoskeletons, excluding Rex, require the user to have some form of outside assistance such as crutches to stand upright when walking. This is because current orthopedic exoskeletons only actuate 4 to 8 degrees of freedom (DoF), which is inadequate to allow for full self-balancing. A fully self-balancing exoskeleton would eliminate the need for crutches and allow for higher mobility.

This thesis details the development of four different linear series elastic actuators (LSEA) as part of a National Science Foundation (NSF) funded project to build a 12 degrees of freedom (DoF), self-balancing, compliant lower-body robotic orthotic. This exoskeleton is known as the Orthotic Lower-body Locomotion Exoskeleton or the OLL-E. Each degree of freedom on the OLL-E will be powered by one of the four LSEAs. These actuators utilize high-efficacy components, parallel electric motors, and liquid cooling to maintain a small lightweight design and attain high power to weight ratios.

1.1. Overview/Motivation

There are many medical conditions that can lead to limited mobility. These include muscle rigidity, muscle relaxation, or involuntary muscle contractions. Other medical conditions that can cause paralysis are cerebral palsy, stroke, muscular dystrophy, or polio syndrome. One of the most damaging and life altering events are spinal cord injuries (SCIs) and strokes. These events can lead to paralysis of one side of the body (hemiplegia), paralysis of the legs and lower body (paraplegia), or even paralysis of all four limbs (quadriplegia). Approximately 288,000 people in the USA have suffered a traumatic SCI, with 17,700 new cases reported each year [9]. The leading cause of SCI injures is automotive accidents, which account for 38% of all injuries [9]. Other common causes of SCI are violence, sporting accidents, and falls.

Individuals unable to recover from their SCI or suffer from other forms of reduced mobility typically use a wheelchair to go about their daily lives. Unfortunately, other medical issues can arise from long-term wheelchair use as well. Being in a seated position for long periods of time can lead to pressure sores [10], impaired bowel functions, decreased muscle tone, obesity, and reduced bone density [11]–[13]. Wheelchair users also rely heavily on their arms to move around. Extensive use of the arms for wheelchair propulsion and other weight-bearing activities can lead to the development of soft tissue disorders and degenerative changes in the shoulder joints [14]. Recent research has revealed lower-body exoskeletons can be a healthier alternative for wheelchairs users by mitigating the effects of being seated for prolong period of time and showing themselves to be effective tools for rehabilitation and training. However, over use of the arms and shoulders is still an issue that needs to be addressed.

Current orthopedic exoskeletons only actuate 4 to 8 DoF, which are incapable of self-balancing and require outside assistance to remain upright. As with wheelchair propulsion, crutches can result in the over use of the upper body, which can be detrimental to the user. Crutches also inhibit the patient's ability to perform manipulation tasks with their hands. The objective of this NSF project is to develop a fully actuated, self-balancing, lower-body exoskeleton. This will be achieved by powering 12-DoF on the lower body. These DoF will be powered by LSEA's, which are characterized by having an elastic element in series with the output of the actuator. This will allow for the implementation of high-fidelity force control and safe, compliant interactions between the user and the exoskeleton. These actuators must be able to meet the unique power and

packaging requirements of each joint of the OLL-E. Maintaining lower actuator weight and size is paramount in exoskeleton design. Large and bulky systems will inhibit mobility and high masses will reduce controllability and performance. Therefore, an analytical process was undertaken to develop well-defined requirements for the joints of the OLL-E and the actuators that power them.

1.1.1. Exoskeletons



Figure 1: Mihailo Pupin Exoskeleton [15], Hardiman [16], BLEEX [1], HAL-5 [17]

Exoskeletons have long been believed to be objects of science fiction, even as they appear on the market today. However, research on exoskeletons began in the 1960's with work at the Mihailo Pupin Institute in Belgrade by Miomir Vukobratovic[15] and the development of Hardiman by General Electric and Cornell University[16]. These early exoskeletons were powered by large electric motors or pneumatics with external power supplies and operating systems. Little progress was made until the 1990's when enhancements in computing power, battery technology, and electric motor design were sufficient to build a self-contained exoskeleton.

In the mid 1990's, the development of the first prototypes of the Hybrid Assistive Limbs (HAL) began at University of Tsukuba in Japan,[17], [18]. This research resulted in several generations of exoskeletons. HAL-3 and 4 were both lower-body exoskeletons developed to help the disabled and elderly with walking, standing up, sitting down, and traversing stairs. HAL-3 and 4 also implemented the use of Electromyography (EMG) technology to detect the users muscle contractions and follow their movements [19]–[22]. Research with these exoskeletons has culminated in the development of HAL-5 in 2005, which is a full-body exoskeleton for human

augmentation. HAL-5 allows the user to lift and carry heavy weights up to 40kg and leg press weights up to 140kg. The exoskeleton has a system weight of 23kg and an operating time of approximately 2 hours and 40 minutes. Like its predecessors, HAL-5 use bioelectrical signals to predict the user's intended movements and provide mechanical assistance.

In 2001, DARPA initiated the Exoskeletons for Human Performance Augmentation program. From this initiative came two notable exoskeleton systems, the Berkeley Lower Extremity Exoskeleton (BLEEX) developed by U.C. Berkeley [1] and XOS by Raytheon Sarco [3]. The XOS was a full-body exoskeleton that augmented the user's strength, allowing them to lift and carry heavy loads. However, XOS required a tether and external power supply to operate. BLEEX was the first self-contained exoskeleton capable of providing load-bearing assistance to its user. This was achieved with 14-DoF, 8 of which were powered by hydraulic cylinders and passive joints constrained with springs and elastomers [23]–[27]. It was determined that the 75kg BLEEX required 2.27 kW (3 HP) of hydraulic power and 220 W of electrical power to maintain a walking speed of 1.3 m/s. This required the hydraulic system of BLEEX to produce 20 LPM (5.2 gpm) of hydraulic flow at a pressure of 6.9 MPa (1000 psi). This power was produce by a small internal combustion engine attached to a hydraulic pump on the back of the exoskeleton [28].

In more recent times, multiple newly formed companies have started to produce exoskeletons for industrial and medical applications. While not classified as an exoskeleton, Lokomat® [4], [29] has been used to provide locomotor training in paraplegic patients. The ReWalk™ Personal Exoskeleton [6], [13] became the first exoskeleton to be approved by the Food and Drug Administration (FDA) for public use. Since then, the Indego™ Personal [30] and EksoGT™ [8], [31] have also received regulatory approval from the FDA [32]. Other notable products currently being developed are the Rex from REX Bionics [5], [33], ARKE™ from Bionik Laboratories [34], and Phoenix from SuitX [35]. However, these exoskeletons typically only power the hips and knees necessitating the use of crutches for walking and maintaining balance.

1.1.2. Humanoid Research at Virginia Tech

The Terrestrial Robotics Engineering and Controls (TREC) Lab at Virginia Tech has developed several generations of force-controlled humanoid robots. The first of these robots to be developed was the Shipboard Autonomous Firefighting Robot (SAFFiR) [36], [37]. This 12-DoF lower-body robot used the first generation of LSEA's developed in the TREC Lab. These actuators featured a

ball screw coupled to a brushless DC (Direct Current) motor through a timing pulley. The actuators also utilized configurable compliance that allowed the stiffness to be adjusted and tuned for each joint [38]. This was accomplished by mounting a titanium beam in a cantilever configuration between the frame of the robot and the actuator. Knowledge and experience gathered from SAFFiR was used to develop the Tactical Hazardous Operations Robot (THOR), which was Virginia Tech's entry into the DARPA Robotics Challenge (DRC) [39]. THOR was a humanoid robot, featuring an upper body with DYNAMIXEL arms and a lower body employing a new generation of lab developed LSEA's. These actuators featured many mechanical improvements and increased performance, with a force-to-weight ratio approximately 2x greater than the previous generation of SEA's [40]–[44]. The cantilever beam was relocated to be parallel with the actuator and utilized a lever arm to place the titanium beam in pure moment bending. With the DRC Finals approaching, the Electric Series Compliant Humanoid for Emergency Response (ESCHER) robot was developed [45]–[47]. ESCHER featured many enhancements in performance and capability over THOR. During the DRC finals, ESCHER traversed a 61m dirt course in 23 minutes unassisted. The actuators discussed in this thesis are a progression on the second generation of LSEA's developed in the TREC. This new third generation of LSEA features higher force, speed and power output, while maintaining a higher power-to-weight ratio than previous generations.

1.1.3. Series Elastic Actuation

Series elastic actuators have many beneficial features for robots that employ force control. These capabilities include energy storage, impact absorption, and high bandwidth force control [48]–[55]. The first SEA used a motor mounted to a ball screw with multiple coil springs for its elastic element. This LSEA was implemented on a 12-Dof lower body humanoid robot [56]. Since then, a multitude of SEA designs have been developed. However, SEA's primarily come in two configurations, linear actuators[41], [45], [49], [50], [54] and rotary actuators[57]–[60].

The elastic element greatly dictates the performance of an SEA. Systems with low elasticity have higher controllability at the cost of poor force control performance. Conversely, systems with high elasticity have excellent force control performance, but are more difficult to control. A larger variety of compliance configurations with different performance attributes have been explored since the development of the first SEA. These configurations include variable stiffness[61]–[63], variable damping[64], [65], nonlinear stiffness[66], and viscoelastic compliance[67]. Other

actuators have incorporated lockouts that allow the compliance to be turned on and off [60], permitting the use of position control and force control on the same system. Some actuators have compliant elements with adjustable stiffness, allowing fine tuning and adjustments to performance without the need to manufacture new components [38], [68], [69] .

Much of robotic design is focused on optimizing size, weight, and power. Increasing one of these attributes typically adversely affects the other two. Several design techniques have been used to increase the power output of actuators while maintaining low weight and/or small package size. One of these methods is to use two smaller motors working together in the place of one larger more powerful motor [70]–[73]. Another method of increasing the power output of electric actuators is to actively cool the DC motors. By effectively removing the heat from the motors, the power output can be increased. Liquid cooling has been utilized in several robotic applications, including team SCHAFT during the DARPA DRC [67], [73]–[77]. The LSEA’s discussed in this thesis combine many of these features into one optimized design, including the use of ball screws, dual motors, and liquid cooling.

1.2. Thesis Organization

This thesis focuses on the requirements development and design analyses used to derive the actuators for the OLL-E. Four unique linear SEA’s were designed to meet the varying requirements of each powered degree of freedom on the exoskeleton. Chapter 2 discusses the analytical approach used to develop the speed, torque, and power requirements for each joint of the OLL-E. This includes the examination of the human gait and simulation of the humanoid ESCHER. Chapter 3 reviews the analyses and in-house tools used to aid in the selection of components for a preliminary actuator design. Once major components were selected, the final process of detailed design and integration occurred. Chapter 4 covers the analyses and tools used to design the compliant element of the LSEA. These include finite element analysis (FEA), and a discussion of the nonlinear properties of the selected spring design. Chapter 5 reviews the mechanical design of the four LSEA’s and analyses used during the design processes. Finally, Chapter 6 contains the conclusion, recommendations for improving the actuator design, and future work that can be conducted utilizing these actuators.

2. Exoskeleton Requirements Development

To begin the development of the OLL-E, a concept exploration and requirements development process was undertaken. This top down approach decomposes the objectives of the project into concept requirements. These requirements are critical in the design process of a complex system as they will provide guidance for all analyses and design choices to follow. Concept requirements is a high-level term that encompasses both operational and performance requirements. Operational requirements dictate the performance objectives and processes needed by the end user. Performance requirements dictate the operational effectiveness of a capability that must be delivered by the system.

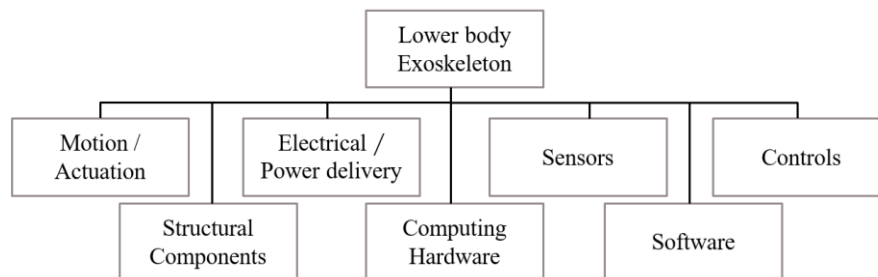


Figure 2: OLL-E High Level Work Breakdown Structure

Continuing this top-down approach, these high-level concept requirements must then be decomposed into detailed quantitative requirements. To accomplish this, the exoskeleton was first divided into subsystems using a work breakdown structure, as seen in Figure 2. At this point, requirements for each subsystem can be generated. Motion and actuation were identified as the impetus of several other subsystem requirements. It was crucial to develop well-defined requirements for the actuators so that other supporting subsystems could be defined.

The first step in generating actuator requirements was to identify the applicable performance requirements. The following list contains the critical performance requirements identified for actuation and motion:

- The OLL-E shall be capable of fully supporting the mass of a 70kg paralyzed person without outside assistance and be fully self-balancing
- The OLL-E shall have a mass of no more than 70kg
- The OLL-E shall be capable of walking speeds equivalent to or faster than the current humanoid robots developed at Virginia Tech.
- The OLL-E shall be capable of walking up stairs.

Next, criteria were chosen to quantify these performance requirements. The capability to fully self-balance is dictated by the number of controllable DoF. The ability to move the OLL-E’s mass at the desired speed can also be quantified. The amount of force required to accelerate a mass is described by Newton’s Second Law and the rate at which this force displaces a mass is described by the Power equation (2.1).

$$P = Fv = mav \tag{2.1}$$

Therefore, these performance requirements can be summarized by the number of DoF, mass, and joint power, where joint power can be further reduced to the criteria torque and angular velocity required at each joint. The joint power requirements for each of the DoF were generated from the analysis of bipedal walking.

2.1. Walking Data Analysis

To develop actuators capable of achieving the performance requirements, quantitative requirements for joint power needed to be generated. This was accomplished by performing analyses of both human gait and robot bipedal movement. Although both use bipedal locomotion, the gait varies greatly between humans and humanoid robots. The system on ESCHER utilizes mostly flat-footed walking that requires large displacements in the knee and hip joints. This is quite different from human walking where the ankle is mainly utilized in heel-strike and toe-off [78]. For this reason, analyses were performed on both human gait and robot bipedal movement.

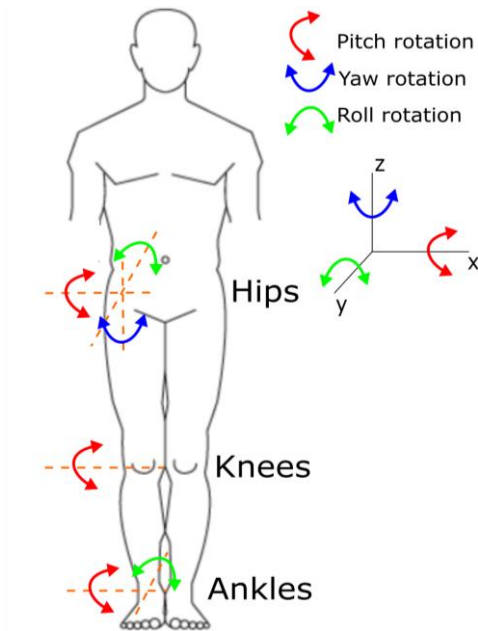


Figure 3: DoF Naming Convention and Locations

With a similar configuration to THOR and ESCHER, OLL-E will utilize 6 degrees of freedom per leg for a total of 12 powered degrees of freedom. The following naming convention will be used to describe these degrees of freedom. These joint movements will be described as: hip yaw, hip pitch, hip roll, knee pitch, ankle pitch, and ankle roll. These degrees of freedom are shown on a human in Figure 3, and is identical in layout when discussing humanoid robots as well.

2.1.1. Human Gait Data

The human gait cycle can be considered a pattern of movements that are repeated each step. The gait cycle is therefore typically described and analyzed within the confines of a single cycle, where all consecutive cycles are assumed to be identical [79]. The two main phases of the gait cycle are the Stance phase and the Swing phase. These two main phases can be seen in Figure 4. The stance phase consumes approximately 60% of the gait cycle and begins when the heel strikes the ground [80], [81]. During this time, the foot is in contact with the ground. The remaining 40% is the swing phase, which begins with toe off. During this time, the foot is swinging through the air and ends when the foot strikes the ground. At this point, the cycle is repeated. All human data were analyzed using this cycle, where 0% represents the initiation of the cycle and 100% represents the completion of the cycle.

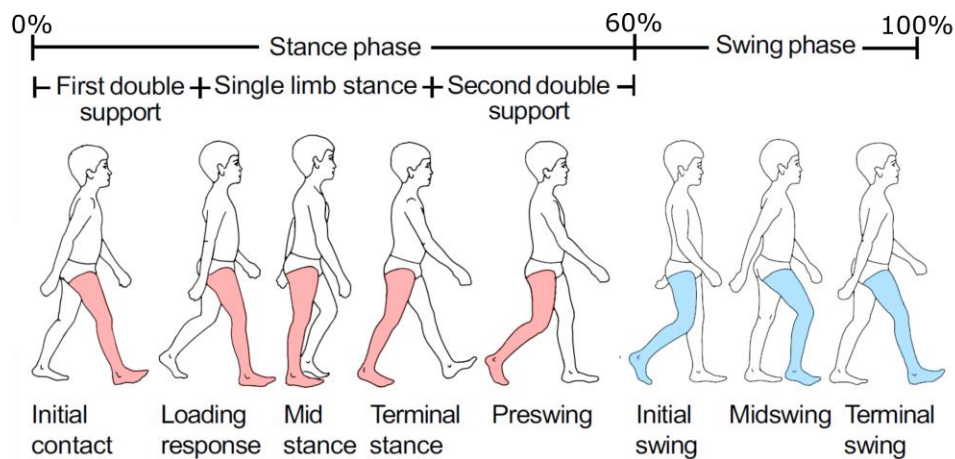


Figure 4: Human Gait Phases [79]

In order to gain insight to the power requirements for the OLL-E, the overall mass of the system must be taken into consideration. The OLL-E must be capable of walking while supporting its own weight as well as the user’s weight, for a combined mass of 140kg. Therefore, walking data from a human of the same mass should be utilized. However, due to this high combined mass, data based on the average human gait would not be sufficient to determine these power requirements.

Consequently, the torque and power requirements were obtained using mass dependent gait data [79]. These data were given in units of Nm/kg and W/kg respectively, for a human walking at approximately 1.0 m/s. The product of the combined system mass and these data were used to determine the torque and power requirements. Plots of the scaled torque and power data as well as joint-velocity can be seen in Figure 5.

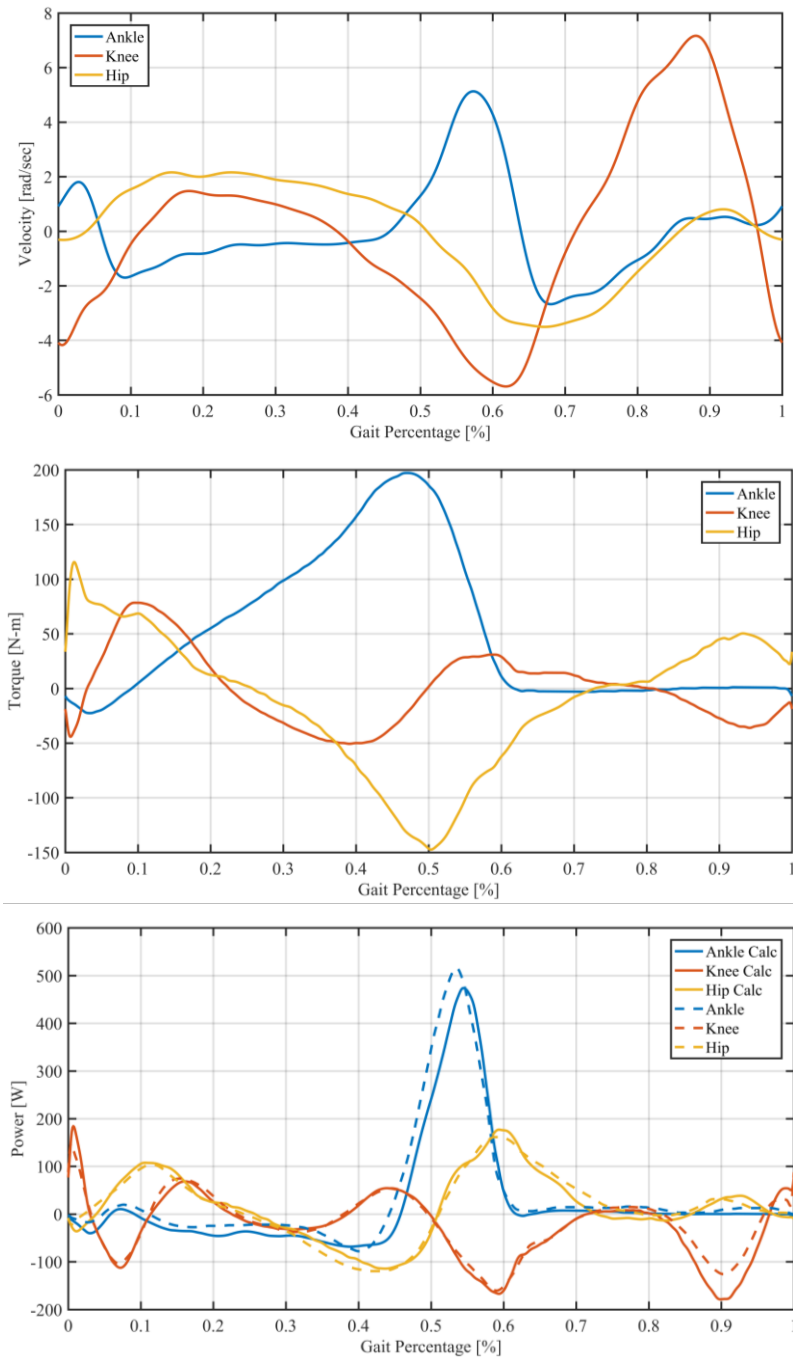


Figure 5: 140kg Human Joint Velocity, Torque, and Power for One Gait Cycle

It should be noted that the power plot in Figure 5 contains two power data sets for each joint. This was done to compare the provided power data sets with the power calculated from the velocity and torque data sets. Slight discrepancies can be noted between the two power curves of each joint. In order to maintain conservatism in the performance requirements, data that yield the highest peak values for each joint were utilized.

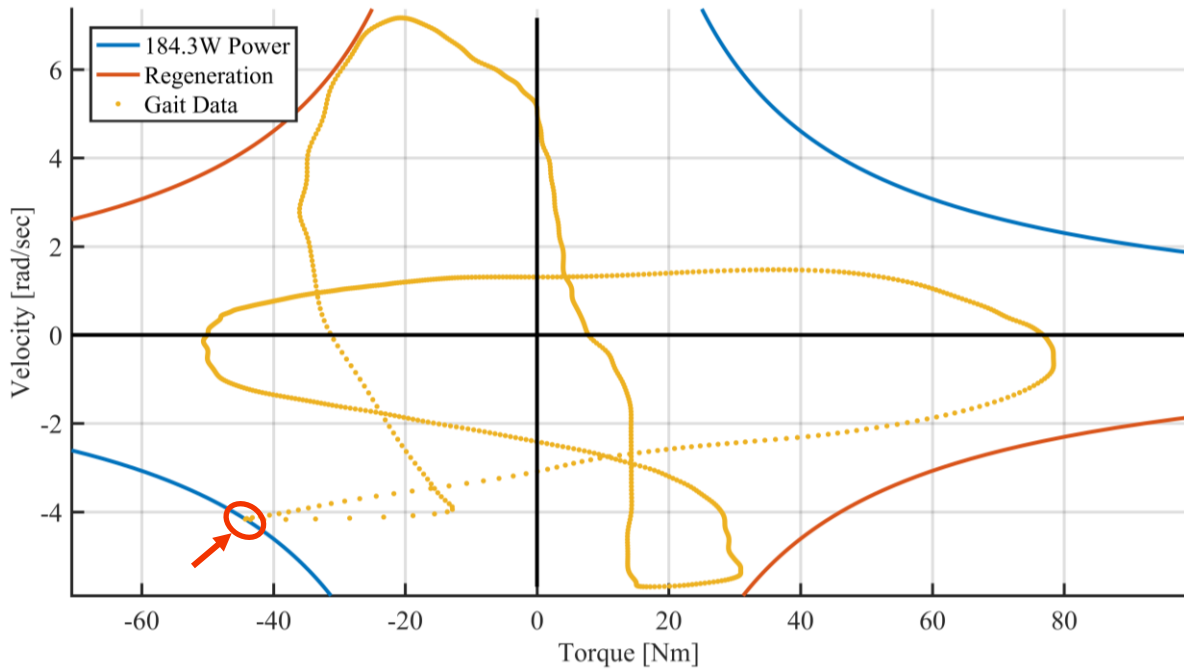


Figure 6: Joint Power Visualization for Human Knee

To a better understand the relationship of joint torque and velocity during the gait cycle, a power plot was created. This plot shows how energy is stored or used during the gait cycle for each joint. This is achieved by plotting torque versus its corresponding velocity. The first and third quadrants of the plot represents power used, while the second and fourth quadrant represent regeneration or energy gathered. An example of this plot for the human knee can be seen in Figure 6. Lines of constant power were also added to the plot. These lines help visualize the operational area of the joint and are placed in such a way that they intersect the peak power point, which is circled in red on Figure 6. In this example, an actuator capable of continuous operation $\pm 184\text{W}$ would be more than sufficient to power this joint. All of the plots generated for each joint can be found in Appendix A Figure A 1. Finally, the peak values of each joint their corresponding values in the gait cycle were then gathered for analysis and can be found Appendix B Table B1, Table B2, and

Table B3. These data represent the critical performance points during the gait cycle. These data were then further reduced to only the peaks values for each joint, as seen in Table 1.

Table 1: Summary of 140kg Human Gait Peak Values

Pitch Joint Name	Peak Power [W]	Peak Torque [Nm]	Peak Velocity [rad/s]
Human Hip	161.45	147.41	3.51
Human Knee	184.31	78.41	7.17
Human Ankle	515.92	197.17	5.13

This table summarizes the peak pitch-joint requirements for a 140kg human walking at 1.0 m/s. These peak values can be used as design criteria for each joint as all other operating points during the gait cycle are encompassed by these values. However, this analysis only examines human like walking and further analysis of bipedal walking was required to ensure a robust set of requirements was generated.

2.1.2. Humanoid Robot Walking Data

Analysis of humanoid robot walking was performed utilizing the lab’s robot ESHCER. Both live test data and simulations were available for ESHCER. Again, these data would only be useful if they were generated with ESHCER having the same 140kg mass of the OLL-E. For this reason, simulations were conducted in the software package Gazebo. Gazebo allows for the simulation of the dynamic behaviors of robots and the sensor data they expect to receive while operating. The full dynamic model of ESHCER was modified to an approximation of the OLL-E. The masses of ESHCER’s lower body segments were equally scaled up until the overall mass was 140kg. All other characteristics of the body segments were maintained. Three different scenarios were then simulated; walking at 0.48 m/s, walking at 0.20 m/s, and stepping up 8-inch steps. These scenarios were considered to be at the extremes of ESHCER’s physical operational capabilities. The data were plotted and analyzed in the same method as the human-gait data. All of the plots generated from these data can be found in Appendix A. All of the peak data points with their corresponding values can be found in Appendix B. As with the human data, the peak values for each scenario were gathered and are summarized, as seen in Table 2, Table 3, and Table 4.

Table 2: Summary of Peak Values of 140kg ESCHER Walking at 0.48m/s Simulation

Combined Joint Maximum Values	Peak Power [W]	Peak Torque [Nm]	Peak Velocity [rad/s]
Hip Yaw	26.22	59.63	0.65
Hip Roll	69.06	175.80	0.74
Hip Pitch	707.48	200.00	5.08
Knee	780.04	394.66	5.74
Ankle Pitch	150.41	186.25	3.15
Ankle Roll	65.75	71.96	1.95

Table 3: Summary of Peak Values of 140kg ESCHER Walking at 0.02m/s Simulation

Combined Joint Maximum Values	Peak Power [W]	Peak Torque [Nm]	Peak Velocity [rad/s]
Hip Yaw	6.20	27.76	0.44
Hip Roll	73.30	165.91	0.66
Hip Pitch	92.79	100.01	2.35
Knee	136.59	243.60	4.01
Ankle Pitch	138.74	171.03	2.85
Ankle Roll	28.97	71.02	1.63

Table 4: Summary of Peak Values of 140kg ESCHER Waking Up Stairs Simulation

Combined Joint Maximum Values	Peak Power [W]	Peak Torque [Nm]	Peak Velocity [rad/s]
Hip Yaw	63.62	101.87	1.85
Hip Roll	78.97	208.50	0.79
Hip Pitch	481.93	200.00	4.04
Knee	420.10	300.00	6.85
Ankle Pitch	220.29	163.78	4.60
Ankle Roll	116.25	89.55	5.90

2.2. Joint Data Synthesis and Actuator Requirements

Table 5: Synthesis of Human and Humanoid Peak Data Points

Combined Human Robot Data	Peak Power [W]	Peak Torque [Nm]	Peak Velocity [rad/s]
Hip Yaw	63.6	101.9	1.8
Hip Roll	79.0	208.5	0.8
Hip Pitch	707.5	200.0	5.1
Knee Pitch	780.0	300.0	7.2
Ankle Pitch	515.9	197.2	5.1
Ankle Roll	116.3	89.5	5.9

The human gait data and three robot-walking simulations were finally synthesized into one set of joint requirements. This was done by selecting the maximum values for each joint from the four sets of data. In doing so, the final set of requirements encompasses all operating points from these walking scenarios. These requirements give OLL-E the capability to implement the current walking controls scheme used by the humanoid at Virginia Tech, as well as allowing for future testing of different and/or more human like walking schemes.

The final set of joint requirements are shown in Table 5. It is interesting to note which data sets contributed values to the final set of requirements. Hence, the values in the table have been color-coded by which data set they were obtained. All black values were pulled from the ESCHER stair climbing data set, while the green numbers are from the ESCHER 0.48m/s walking-speed data set. The numbers highlighted in blue are peak values contributed by the human gait analysis. Here, the difference between human and bipedal walking can be seen. While humans have most of their power in the ankle, the humanoid relies heavily on its knees and hips. The largest roll and yaw values occurred while traversing stairs. This is in part, due to how the robot shifts its center of mass from one leg to the other when stepping up. The peak knee torque highlighted in red was reduced from 395Nm found in the 0.48m/s simulation to 300Nm from the stair climbing simulation to account for the increase in knee velocity and maintain reasonable power requirements.

3. Series Elastic Actuator Component Selection

With quantified performance requirements, the major components of the actuator could be analyzed and selected. These major components include the motor, drivetrain, bearings, and elastic element of the actuator. This selection process will dictate greatly the final design and performance of the actuator. Once major components are selected the final process of detailed design and integration can occur. Although this section is presented in a linear fashion, it should be noted that the following analyses were performed iteratively. Multiple components and combination of components were compared before final selections were made. Multiple analytical tools were developed in Microsoft Excel™ and MATLAB™ to facilitate this process. The following sections summarize the analytical methods and final component selections for the actuators.

3.1. Motor Selection

The most critical component of the actuator is its mechanical power source. The power source can be independent for the actuation, such as a pump in a hydraulic system with multiple cylinders, or integrated into each individual actuator. Because the OLL-E is a manned system, extra consideration must be given to pilot safety and regulations. For this reason, hydraulics systems were excluded from this analysis due to their health, safety, and fire risks. Stipulations were also placed on the maximum operating voltages of all electrical systems on the OLL-E. Systems that exceed 50V fall under statutory regulations. Therefore, electrical components that utilize the industry standard of 48V or lower were examined.

Over 50 brushed, and brushless DC motors encompassing a wide range of manufactures, applications, and formats were examined. Motor manufactures included Anaheim Automation, Kollmorgen, Maxon, Moog, Parker, and Soneceboz. Wide ranges of motor formats are provided by these companies, such as NEMA (National Electrical Manufactures Association) industry standard packaging, non-standard packaging, flat or pancake motors, and frameless motors. A selection of the motors examined during this analysis can be found in Appendix C.

It was determined motors capable of continuous operation at the required power levels were prohibitively large and heavy. Although frameless motors suffered from less of these issues, the added complexity of designing and manufacturing precisions mounting components made them less desirable than a framed motor. For this reason, multiple smaller motors working in unison or

smaller motors over-driven above their rated power were studied. However, over-driven motors suffer from overheating unless some form of active cooling is implemented.

3.1.1. Force Cooling DC Electric Motors

With proper thermal management, brushless DC motors can be driven at very high currents while maintaining safe winding temperatures [76]. This allows much higher power-to-weight ratios to be realized that would otherwise not be possible. However, it is important to remember that the cooling system will add size, weight, and complexity to the system. This is dependent on the selected coolant, supporting systems, and is highly application specific.

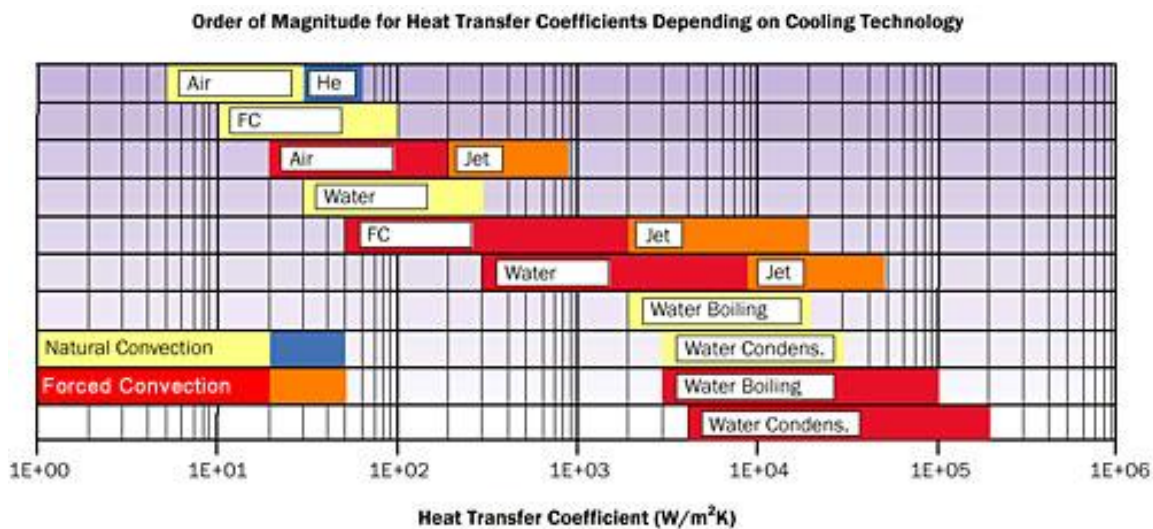


Figure 7: Heat Transfer Coefficients for various cooling methods and coolants [82]

Manufacturers typically provide the maximum continuous power a motor can safely maintain while it is operating in quiescent room temperature air. Here, the only cooling of the motor can occur via natural convection with the surrounding air. As can be seen in Figure 7, natural convection with air has the lowest heat transfer coefficients of any of the presented methods. Other methods of cooling could potentially increase the heat transfer coefficient by orders of magnitude. Implementing a system with forced air could yield heat transfer coefficients 3x to 60x greater than natural convection[82], [83]. This type of cooling is utilized extensively by high-power electronics and computers today. Typical applications utilize a fan in conjunction with a heat sink mount to the heat-generating component. This would require cooling systems to be individualized to each actuator. Increases in actuator package size and mass must be considered concurrently with the performance increases.

Another viable alternative is to use a coolant other than air. Water-based solutions possess very high specific heat and thermal conductivity, making them conducive for high-performance cooling applications [84]. The heat transfer coefficient of forced convective cooling with water can be 10x to 2000x greater than that of air in natural convection. However, the mass of the water and pumping equipment can be significant when compared to air cooling applications. Conversely, a centralized approach can be used, were multiple heat-generating components are all on the same cooling loop. This is also conducive to humanoid and exoskeleton design, as most of the mass of the cooling can be located in a less intrusive area than the legs. Thus maintaining lower mass of the limbs at the cost of increased overall system mass.

Although water-cooled motors and the necessary support hardware may weigh more than a system designed with larger motors capable of the same power output, the ability to centralize the mass of the cooling system was seen as a highly desirable attribute. For these reasons along with other desirable characteristics, Maxon was chosen as the motor supplier for the OLL-E. The cylindrical design of Maxon's motors lends themselves to be easily retrofitted with cooling jackets. Maxon also provides in-depth details on the thermal characteristic of their motors, allowing a more analytical design approach to be taken.

3.1.2. Determining Maximum Continuous Current

Using the provided equations in Maxon technical documents and [85], the steady state thermo-electric behavior of their motors can be modeled. The primary source of heat generation in the motor is due to the resistive heating in the motor's winding. This process is also called Joule heating or ohmic heating and is described by Joule's first law (3.1), where power lost due to resistive heating P_j is a function of the motor current I and the winding resistance R_T .

$$P_j = I^2 R_T \quad (3.1)$$

Because the winding is encased inside the motor, it must conduct this heat through its casing to the outside environment. Therefore, the change in the winding temperature ΔT_w is a function of the thermal resistance R_{th} and the resistive heating P_j as describe by equation (3.2), with T_w being the winding temperature and T_a the ambient temperature. The thermal resistance R_{th} is the sum of the thermal resistances from the winding to the surface of the motor R_{th1} and the thermal resistances from the motor surface to its surroundings R_{th2} (3.3). Maxon provides both of these thermal

resistance values for their motors, with R_{th2} being experimentally determined under natural convection with 25°C air.

$$\Delta T_w = T_w - T_a = R_{th} P_j \quad (3.2)$$

$$R_{th} = R_{th1} + R_{th2} \quad (3.3)$$

Substituting equations (3.1) and (3.3) into equation (3.2) and solving for the current I yields the equation (3.4). The current I is now the function of the winding temperature, the thermal resistance from the winding to the motors surface, the thermal resistance from the motors surface to the environment, and the windings electrical resistance.

$$I = \sqrt{\frac{T_w - T_a}{(R_{th1} + R_{th2}) - R_T}} \quad (3.4)$$

However, the electrical resistance of the motors winding R_T is also function of temperature. This resistance is dictated by a materials temperature coefficient of resistance. Copper has a positive temperature coefficient of resistance, meaning that as temperature increases, the electrical resistance increases as well. This results in a feed-forward loop that must be taken into consideration. The equation for Resistor Temperature Dependence is provided in equation (3.5). Where R_{25} is the provided winding resistance at 25°C and the thermal resistance coefficient of copper is $\alpha_{Cu} = 0.0039 \text{ } \Omega/\text{K}$.

$$R_T = R_{25}(1 + \alpha_{Cu}(T_w - 25^\circ\text{C})) \quad (3.5)$$

Substituting equation (3.5) into equation (3.4) yields the steady-state model of the motors thermo-electric behavior (3.6). The maximum continuous current can then be calculated by setting the winding temperature T_w to the provided maximum permissible winding temperature T_{max} and selecting a conservative ambient temperature T_a . This results in R_{th2} as the only variable that can influence I_{max} , while all other variables are fixed by the characteristics of the motor.

$$I_{max} = \sqrt{\frac{T_{max} - T_a}{(R_{th1} + R_{th2}) - (R_{25}(1 + \alpha_{Cu}(T_{max} - 25^\circ\text{C}))}} \quad (3.6)$$

The overall heat transfer coefficient of a heat exchanger is very difficult to analytically determine and will carry large amounts of uncertainty [86]. A multitude of factors, such as cooling jacket geometry, coolant type, flow rate, flow characteristics, and surface finish, will greatly influence the thermal resistance R_{th2} . Using the technique from [76], the resistance can be set to zero to

determine the theoretical maximum continuous current of the motor. While this approach is useful for comparing motors during the selection process, it is not a realistic representation of true motor performance. Experimentation on a similar liquid-cooled Maxon yielded an R_{th2} of 0.0325K/W. This results in a 160x improvement over the natural convective cooling thermal resistance value of 5.2K/W provided by Maxon[76].

A more conservative approach was taken during motor selection process and subsequent drivetrain analysis. All analyses were performed with an ambient temperature of 25°C and the maximum winding temperature was divided by a safety factor of 1.1. Finally, the thermal resistance for natural convection provided by Maxon was divided by an improvement factor of 50x. This was considered an easily obtainable thermal resistance for a liquid cooling system. Equally, if the improvement factor of the final design was experimentally determined to be greater than 50x, this would be viewed as improving the safety factor on the maximum winding temperature and/or an increase in the maximum operating environment temperature.

Table 6: Theoretical Maximum Continuous Current and Power of Maxon Motors

Maxon Product #	Thermal Resistance Winding-Housing R_{th1} (K/W)	Thermal Resistance Housing-Ambient R_{th2} (K/W)	Max Continuous Current Cooling (A)	Torque T_{max} (Nm)	Winding ohmic losses (W)	Power (W)	Power to Motor Weight (kW/Kg)	Power to Motor Volume (kW/cm ³)
353297	1.85	1.3	9.7	1.26	47.2	417.2	0.2	0.7
167132	0.5	1.3	18.7	1.59	168.5	731.3	0.3	1.4
167131	0.5	1.3	10.8	1.59	168.5	352.2	0.1	0.7
136212	1.1	1.7	12.9	0.55	78.2	542.8	0.4	2.1
136209	1.1	1.7	7.5	0.55	78.2	280.0	0.2	1.1
305015	0.21	7.4	23.6	0.65	323.8	808.7	2.3	9.1
351144	0.336	6.54	33.5	0.18	189.9	1014.8	3.5	11.3
426450	0.754	0.793	6.2	0.21	250.9	45.0	0.2	0.5
393879	0.734	3.69	11.3	0.80	239.1	305.6	0.4	1.4
397800	0.305	0.284	18.3	1.29	621.8	256.6	0.3	1.2

Table 6 summarizes the results from equation (3.6) utilizing the conservative assumptions and Maxon’s provided data. Two Maxon motors stood out from the rest, the 305015 and 351144. Both had an order of magnitude better power-to-weight ratio than any other motor examined. This was

due to their relatively low winding resistance R_T and winding-to-case resistance R_{thI} . The 351144 would appear to be the best choices as it out performs the 305015; however, this is a high-speed model with a nominal speed of 62,200 revolutions per minute (rpm). This motor would require very large gear ratios that would likely increase the size and complexity of the drivetrain. These high speeds would also require all of the rotating masses to have precision balancing to prevent dangerous vibrations. Therefore, the Maxon EC 4-Pole 305015 was chosen as the motor to power the OLL-E.

3.2. Gearing and Drivetrain Selection

To achieve the desired joint speeds and torque, the motor power must be passed through some form of gear reduction. Numerous methods of speed reduction exist in a large variety of form factors. The components examined were: planetary gearboxes, cycloidal gearboxes, Harmonic Drives®, ball screws, and timing belts. These components offered a large variety of off-the-shelf (OTS) solutions that can be adapted into an actuator. Examining the joint requirements and selected motor it was determined that gear ratios between 1:150 and 1:1600 would be required. However, the maximum input speed, maximum output torque, efficiency, rigidity, impact resistance, size, and weight must also be considered along with gear ratio. Given all of these design requirements, it was determined that no single gear reduction system was capable of meeting the necessary joint speed/torque requirements. For this reason, a combination of systems was adopted.

The ball screw presented itself as the primary candidate for the main component of the actuators gear train. Ball screws possess very low backlash, high efficiency, and high load bearing capabilities for their relatively small size and low weight. Like all power screws, a ball screw converts rotational motion into linear motion. However, unlike normal power screws, ball screws are capable of efficiencies in excess of 90% [87]. This is due to the rolling elements in the nut that greatly reduce the friction. This also allows the screw to be reversible or easily back drivable. When coupled to a lever arm to convert the linear motion back into rotational motion, very large gear reductions can be achieved.

However, the input speed of the motor exceeds the safe rotational speed limit of ball screws. For this reason, pre-gearing on the motor must occur. This was achieved by adding a timing pulley between the motor and ball screw. This also allows the gear ratio of each actuator to be easily tailored to the various requirements of each joint. In several instances pre-gearing ratios greater

than what was achievable with timing pulleys were required. These higher gear ratios were achieved by installing a planetary gearbox on the motor. In this configuration, power is transmitted through the gearbox, timing pulley, ball screw, and lever arm to accomplish a final gear reduction in excess of 1:1500.

Due to the complexity of the gear train and plethora of possible configurations, an analytical tool was developed in Microsoft Excel™ to expedite the selection process. This tool allowed multiple actuator configurations to be simultaneously analyzed and compared and included analyses of gear ratios, ball screw speed and force, two-bar linkages, and ball screw design criteria. The tool also incorporated the results from motor performance analysis discussed in section 3.1.2. The following sections detail the analytical methods used to develop this tool and the subsequent results.

3.2.1. Ball Screw Analysis

Ball screws convert rotational velocity and torque into linear velocity and force. This relationship is based on the lead of the ball screw. Lead is defined as the linear distance the ball nut travels per revolution of the screw. The required motor torque T_m for a given load F can be determined using equation (3.7), which is derived from the power screw efficiency equation [88]. Here, P_h is the ball screw lead, η is the ball screw efficiency, and G is the per-gearing ratio provided by any components between the motor and ball screw. As shown in equation (3.8), G is defined as the ratio between the drive gear and the driven gear.

$$T_m = \frac{F P_h}{2 \pi \eta} \cdot G \quad (3.7)$$

$$G = \frac{N_{drive}}{N_{driven}} \quad (3.8)$$

Since the max continuous motor torque T_{max} has already been defined, equation (3.7) can be solved for output force as a function of the of the gear ratio G and pitch P , as seen in equation (3.9). From this equation, the combination of timing pulleys and ball screws were examined.

$$F = \frac{(T_{max}/G) 2 \pi \eta}{P_h} \quad (3.9)$$

Finally, the linear velocity of the ball nut can be calculated using the relationship between the ball screw lead and motor's rotational velocity in equation (3.10). Where the motor's velocity ω_{rpm} is

converted from rpm to revolutions per second and multiplied by G to account for any per-gearing between the ball screw and motor.

$$v = \frac{\omega_{rpm}}{60} \cdot G P_h \quad (3.10)$$

3.2.2. Two-Bar Linkage Analysis

To manipulate the joints of the OLL-E, the linear force and velocity of the ball screw must be converted back into torque and rotational velocity. This can be achieved through many different types of mechanisms and linkages. However, one of the simplest methods for converting linear motion to rotational motion is through a lever arm. Together with the actuator, this system can be modeled by the simple two-bar linkage found in Figure 8.

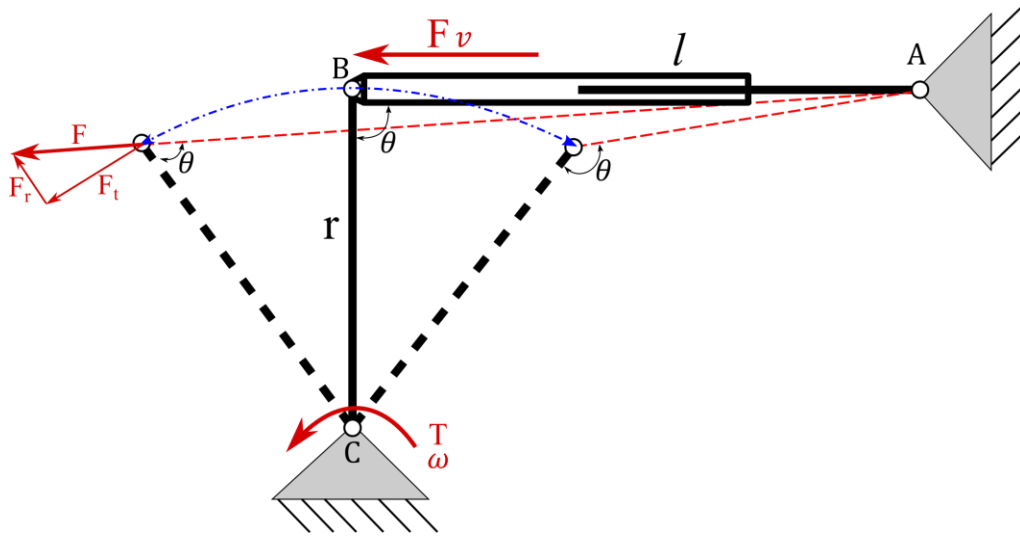


Figure 8: Two-Bar Linkage Free-Body Diagram

As the length of the actuator AB changes, the lever arm BC is rotated about point C . Because the lever arm BC is a fixed length r , the input angle θ between the lever arm and actuator varies. This results in the generation of component forces. Consequently, peak torque and rotation velocity both occur when the actuator is perpendicular to the lever arm. The relationship of the torque and rotational velocity about point C can be described by the relationships shown in equations (3.11) and (3.12).

$$T_{joint} = r F \sin \theta \quad (3.11)$$

$$\omega_{joint} = \frac{v \sin \theta}{r} \quad (3.12)$$

With the final output torque and velocity at the joint determined, the overall effective gear ratio of the drivetrain can also be calculated. The motor torque and joint-torque were utilized to derive the gear-ratio equation seen in (3.13); however, the rotational velocity of the motor and joint can also be utilized. The input angle θ was assumed to be 90° and dropped from the equation in order to determine the maximum relative gear ratio G_{eff} . The overall efficiency of the gear train components can also be added into the equation using ψ .

$$G_{eff} = \frac{T_{motor}}{T_{joint}} = \frac{\omega_{joint}}{\omega_{motor}} = \frac{GP_h}{r 2 \pi \psi} \quad (3.13)$$

The results of these calculations were then compared to the speed/torque requirements for each joint, allowing a set of viable gear-train component combinations to be generated.

3.2.3. Ball Screw Analysis

Although a gear train may meet the speed/torque requirements of a particular joint, other design factors must be considered before a final selection can be made. These factors include the maximum static load, maximum axial load, and maximum rotational speed. These requirements were incorporated into the analysis, as they are directly related to the input/output speeds and torques of the gear train. The component efficiencies were also incorporated into this analysis. The mechanical efficiencies were assumed to be 0.80 for the Maxon gearbox, 0.95 for the THK precision ball screw, and 0.99 for the S3M timing belt.

The first critical design requirement is the maximum allowable force that can be applied to the rolling elements of the ball screw. THK provides a static load rating for all of their products. This static load rating is the maximum allowable load that can be applied to the ball nut without causing permanent damage. For this reason, the normal operating point of the actuator should not be close to this number. Unknown loads, impacts, or outside forces could easily cause loads that could exceed this rating. In order to mitigate this risk, a safety factor of 1.2 was applied to the static load rating. Table 7 summarizes the maximum permissible static load determined using the safety factor for the two ball screws selected for the OLL-E.

Table 7: Ball Screw Static Load Safety Factor

THK Part Number	DK 1404-3	DK 1404-4
Static Load Rating (CoA)(kN)	7.6	10.2
Static Load Safety Factor	1.2	1.2
Permissible Static Load (kN)	6.3	8.5

Besides the static load factor of the ball nut, the permissible axial load must be examined as well. This is done by examining the load bearing capability of the ball screw by assuming it to be a rod of equal diameter under the same loading conditions. This is especially important as the length of the ball screw increases and bulking failure becomes predominate. As recommended by THK, a safety factor of 1.5 was applied to these values as well. Table 8 summarizes the loads at which tensile/compressive failure and buckling failure will occur. Between these two values and the maximum permissible static load, the lowest value was selected as the maximum permissible load on the ball screw. The maximum permissible static load was the lowest value for both ball screws.

Table 8: Ball Screw Permissible Axial Load

THK Part Number	DK 1404-3	DK 1404-4
Distance between points (mm)	150	150
Young's Modulus (N/mm ²)	2.06E+05	2.06E+05
Moment of Inertia (mm ⁴)	1087.4	951.7
Mounting Factor (η)	0.25	0.25
Safety Factor	1.5	1.5
Tensile/Comp Stress (MPa)	147	147
Buckling Load (kN)	16.4	14.3
Tensile/Comp Load (kN)	11.5	10.7

Finally, the maximum permissible rotational speed and dangerous rotational speed of the ball screw were calculated. At speeds that exceed this point, the ball screw can begin to resonate at its natural frequency and become unstable. Like buckling, this speed is largely dictated by the length of the ball screw. Again, the lowest of these two values was selected as the maximum rotational speed for the ball screws.

Table 9: Ball Screw Dangerous Rotational Speed

THK Part Number	DK 1404-3	DK 1404-4
Distance between points (mm)	150	150
Young's Modulus (N/mm ²)	2.06E+05	2.06E+05
Moment of Inertia (mm ⁴)	1087.4	951.7
Cross-sectional area (mm ²)	116.9	109.4
Density (kg/mm ³)	7.85E-06	7.85E-06
Mounting Factor (λ_1)	1.875	1.875
Dangerous Speed (rpm)	18650	18039
Permissible Speed (rpm)	4778	4828

3.2.4. Drivetrain selection

Due to the multi variable nature of the drivetrain, no one finite solution exists. Instead, a set of solutions enveloping various combinations of components can be obtained. This allows for multiple design options as the development of the OLL-E legs progresses, presenting the design engineer with more latitude to optimize the packaging of the actuators and joint designs. In order to bound the solution set, a vector of OTS timing pulleys ratios and a vector lever-arm lengths were generated. Using this 2-D parameter space, the joint speeds and torques for each combination were computed. This solution matrix must then be filtered to determine which combinations meet or exceed the joint requirements.

Ball Screw Pre-gearing	1.45	1.55	1.64	1.82	2.00	2.18	2.27	2.73
Rotational Speed (rpm)	1432.3	1348.0	1273.1	1145.8	1041.7	954.9	916.7	763.9
Linear displacement (m/s)	0.095	0.090	0.085	0.076	0.069	0.064	0.061	0.051
Linear Force (N)	2760.5	2933.1	3105.6	3450.7	3795.7	4140.8	4313.3	5176.0

Lever arm length (m)	Peak Velocity (rad/s)								Lever arm length (m)	Peak Torque (Nm)							
	1.45	1.55	1.64	1.82	2.00	2.18	2.27	2.73		1.45	1.55	1.64	1.82	2.00	2.18	2.27	2.73
0.02	4.77	4.49	4.24	3.82	3.47	3.18	3.00	2.55	0.02	55.21	58.66	62.11	69.01	75.91	82.82	86.27	103.52
0.021	4.55	4.28	4.04	3.64	3.31	3.03	2.91	2.43	0.021	57.97	61.59	65.22	72.46	79.71	86.96	90.58	108.70
0.022	4.34	4.08	3.86	3.47	3.16	2.89	2.78	2.31	0.022	60.73	64.53	68.32	75.91	83.51	91.10	94.89	113.87
0.023	4.15	3.91	3.69	3.32	3.02	2.77	2.66	2.21	0.023	63.49	67.46	71.43	79.37	87.30	95.24	99.21	119.05
0.024	3.98	3.74	3.54	3.18	2.89	2.65	2.55	2.12	0.024	66.25	70.39	74.53	82.82	91.10	99.38	103.52	124.22
0.025	3.82	3.59	3.40	3.06	2.78	2.55	2.44	2.04	0.025	69.01	73.33	77.64	86.27	94.89	103.52	107.83	129.40
0.026	3.67	3.46	3.26	2.94	2.67	2.45	2.35	1.96	0.026	71.77	76.26	80.75	89.72	98.69	107.66	112.15	134.58
0.027	3.54	3.33	3.14	2.83	2.57	2.36	2.26	1.89	0.027	74.53	79.19	83.85	93.17	102.48	111.30	116.46	139.75
0.028	3.41	3.21	3.03	2.73	2.48	2.27	2.18	1.83	0.028	77.29	82.13	86.96	96.62	106.28	115.94	120.77	144.93
0.029	3.29	3.10	2.93	2.63	2.39	2.20	2.11	1.76	0.029	80.06	85.06	90.06	100.07	110.08	120.08	125.09	150.10
0.03	3.18	3.00	2.83	2.55	2.31	2.12	2.04	1.70	0.03	82.82	87.99	93.17	103.52	113.87	124.22	129.40	155.28
0.031	3.08	2.90	2.74	2.46	2.24	2.05	1.97	1.64	0.031	85.58	90.92	96.27	106.97	117.67	128.36	133.71	160.46
0.032	2.98	2.81	2.65	2.39	2.17	1.99	1.91	1.59	0.032	88.34	93.86	99.38	110.42	121.46	132.51	138.03	165.63
0.033	2.89	2.72	2.57	2.31	2.10	1.93	1.85	1.54	0.033	91.10	96.79	102.48	113.87	125.26	136.65	142.34	170.81
0.034	2.81	2.64	2.50	2.25	2.04	1.87	1.80	1.50	0.034	93.86	99.72	105.59	117.32	129.05	140.79	146.65	175.98
0.035	2.73	2.57	2.43	2.18	1.98	1.82	1.75	1.46	0.035	96.62	102.66	108.70	120.77	132.85	144.93	150.97	181.16
0.036	2.65	2.50	2.36	2.12	1.93	1.77	1.70	1.43	0.036	99.38	105.59	111.80	124.22	136.65	149.07	155.28	186.34
0.037	2.58	2.43	2.29	2.06	1.88	1.72	1.65	1.38	0.037	102.14	108.52	114.91	127.67	140.44	153.21	159.59	191.51
0.038	2.51	2.36	2.23	2.01	1.83	1.68	1.61	1.34	0.038	104.90	111.46	118.01	131.13	144.24	157.35	163.91	196.69
0.039	2.45	2.30	2.18	1.96	1.78	1.63	1.57	1.31	0.039	107.66	114.39	121.12	134.58	148.03	161.49	168.22	201.86
0.04	2.39	2.25	2.12	1.91	1.74	1.59	1.53	1.27	0.04	110.42	117.32	124.22	138.03	151.83	165.63	172.53	207.04
0.041	2.33	2.19	2.07	1.86	1.69	1.55	1.49	1.24	0.041	113.18	120.26	127.33	141.48	155.62	169.77	176.85	212.22
0.042	2.27	2.14	2.02	1.82	1.65	1.52	1.46	1.21	0.042	115.94	123.19	130.44	144.93	159.42	173.91	181.16	217.39
0.043	2.22	2.09	1.97	1.78	1.61	1.48	1.42	1.18	0.043	118.70	126.12	133.54	148.38	163.22	178.05	185.47	222.57
0.044	2.17	2.04	1.93	1.74	1.58	1.45	1.39	1.14	0.044	121.46	129.05	136.65	151.83	167.01	182.19	189.79	227.74
0.045	2.12	2.00	1.89	1.70	1.54	1.41	1.36	1.13	0.045	124.22	131.99	139.75	155.28	170.81	186.34	194.10	232.92
0.046	2.08	1.95	1.85	1.66	1.51	1.38	1.33	1.11	0.046	126.98	134.92	142.86	158.73	174.60	190.48	198.41	238.10
0.047	2.03	1.91	1.81	1.63	1.48	1.35	1.30	1.08	0.047	129.74	137.85	145.96	162.18	178.40	194.62	202.73	243.27
0.048	1.99	1.87	1.77	1.59	1.45	1.33	1.27	1.06	0.048	132.51	140.79	149.07	165.63	182.19	198.76	207.04	248.45
0.049	1.95	1.83	1.73	1.56	1.42	1.30	1.25	1.04	0.049	135.27	143.72	152.17	169.08	185.99	202.90	211.35	253.62
0.05	1.91	1.80	1.70	1.53	1.39	1.27	1.22	1.02	0.05	138.03	146.65	155.28	172.53	189.79	207.04	215.67	258.80

Figure 9: Gear Train Solutions Matrix Color-Code to Display Viable Solutions

In order to filter the results and locate viable solution in the matrix, a visual color-coding scheme was utilized. This allowed for a fast visual inspection of the results and insight into how manipulation of input variables altered the solution set. An example of a solution matrix and the applied color-coding can be seen in Figure 9. Values highlighted green represent gear train combinations that meet or exceed the specific requirement for that variable. For example, all gear train combinations that meet or exceeded the joints peak velocity are highlighted green. Conversely, if a result did not meet the requirement, it was not highlighted. If the result violated a specified design requirement, such as permissible static load, it was highlighted orange. Finally, the intersection of viable solutions between the torque and speed matrices were highlighted blue. These results represent a gear train that fulfills all of the specified joint requirements.

Ball Screw Pre-gearing	2.27	2.40	2.67	2.93	3.20	3.33	4.00	4.80
Rotational Speed (rpm)	7058.8	6666.7	6000.0	5454.5	5000.0	4800.0	4000.0	3333.3
Linear displacement (m/s)	0.471	0.444	0.400	0.364	0.333	0.320	0.267	0.222
Linear Force (N)	4667.8	4942.4	5491.5	6040.7	6589.8	6864.4	8237.3	9884.7
Peak Velocity (rad/s)								
Lever arm length (m)	2.27	2.40	2.67	2.93	3.20	3.33	4.00	4.80
0.02	23.53	22.22	20.00	18.18	16.67	16.00	13.33	11.11
0.021	22.41	21.16	19.05	17.32	15.87	15.24	12.70	10.58
0.022	21.39	20.20	18.18	16.53	15.15	14.55	12.12	10.10
0.023	20.46	19.32	17.39	15.81	14.49	13.91	11.59	9.66
0.024	19.61	18.52	16.67	15.15	13.89	13.33	11.11	9.26
0.025	18.82	17.78	16.00	14.55	13.33	12.80	10.67	8.89
0.026	18.10	17.09	15.38	13.99	12.82	12.31	10.26	8.55
0.027	17.43	16.46	14.81	13.47	12.35	11.85	9.88	8.23
0.028	16.81	15.87	14.29	12.99	11.90	11.43	9.52	7.94
0.029	16.23	15.33	13.79	12.54	11.49	11.03	9.20	7.66
0.03	15.69	14.81	13.33	12.12	11.11	10.67	8.89	7.41
0.031	15.18	14.34	12.90	11.73	10.75	10.32	8.60	7.17
0.032	14.71	13.89	12.50	11.36	10.42	10.00	8.33	6.94
0.033	14.26	13.47	12.12	11.02	10.10	9.70	8.08	6.73
0.034	13.84	13.07	11.76	10.70	9.80	9.41	7.84	6.54
0.035	13.45	12.70	11.43	10.39	9.52	9.14	7.62	6.35
0.036	13.07	12.35	11.11	10.10	9.26	8.89	7.41	6.17
0.037	12.72	12.01	10.81	9.83	9.01	8.65	7.21	6.01
0.038	12.38	11.70	10.53	9.57	8.77	8.42	7.02	5.85
0.039	12.07	11.40	10.26	9.32	8.55	8.21	6.84	5.70
0.04	11.76	11.11	10.00	9.09	8.33	8.00	6.67	5.56
0.041	11.48	10.84	9.76	8.87	8.13	7.80	6.50	5.42
0.042	11.20	10.58	9.52	8.66	7.94	7.62	6.35	5.29
0.043	10.94	10.34	9.30	8.46	7.75	7.44	6.20	5.17
0.044	10.70	10.10	9.09	8.26	7.58	7.27	6.06	5.05
0.045	10.46	9.88	8.89	8.08	7.41	7.11	5.93	4.94
0.046	10.23	9.66	8.70	7.91	7.25	6.96	5.80	4.83
0.047	10.01	9.46	8.51	7.74	7.09	6.81	5.67	4.73
0.048	9.80	9.26	8.33	7.58	6.94	6.67	5.56	4.63
0.049	9.60	9.07	8.16	7.42	6.80	6.53	5.44	4.54
0.05	9.41	8.89	8.00	7.27	6.67	6.40	5.33	4.44
0.051	9.23	8.71	7.84	7.13	6.54	6.27	5.23	4.36
0.052	9.05	8.55	7.69	6.99	6.41	6.15	5.13	4.27
0.053	8.88	8.39	7.55	6.86	6.29	6.04	5.03	4.19
0.054	8.71	8.23	7.41	6.73	6.17	5.93	4.94	4.12
0.055	8.56	8.08	7.27	6.61	6.06	5.82	4.85	4.04
0.056	8.40	7.94	7.14	6.49	5.95	5.71	4.76	3.97
0.057	8.26	7.80	7.02	6.38	5.85	5.61	4.68	3.90
0.058	8.11	7.66	6.90	6.27	5.75	5.52	4.60	3.83
0.059	7.98	7.53	6.78	6.16	5.65	5.42	4.52	3.77

Figure 10: Knee Actuator Gear Train Combinations Solution Matrix

In the example provided in Figure 10, the gear train solution matrix for the knee-pitch actuator is presented. As can be seen at the top of the table, only two pre-gearing ratio meet both the rotational speed and force requirements of the ball screw. Following the gear ratio columns down, four peak joint velocities are highlighted blue. Following these rows to the left reveals the necessary lever arm length to achieve this velocity. For example, an actuator with a 1:4 pre-gear ratio and a lever arm between 37mm to 38mm would meet all of the specified design and joint requirements. From this analysis, it was determined that no single actuator configuration was capable of meeting the requirements of every joint on the OLL-E. Instead, multiple actuator designs would be required.

3.3. Final Configuration Selection and Performance Analysis

Using the analyses discussed in sections 3.1 and 3.2, it was determined the OLL-E required multiple actuator configurations to meet the unique requirements of each joint. For this reason, three different designs were chosen to power the six different degrees of freedom. The hip-pitch and knee-pitch joints required the highest power, speed, and torque of any other of the joints. A single liquid cooled Maxon motor was unable to deliver the necessary power. However, it was determined that two motors working in parallel would be capable of achieving the requirements for these joints. These motors are coupled together on the same timing belt to drive the ball screw. This dual-motor-liquid-cooled actuator was given the designation MKIII Heavy.

Table 10: Summary of Actuator Designs and Joint Locations

Designation	MK III Heavy	MK III Lite	MK IV Gear
Motor Count	2	1	1
Liquid Cooling	Yes	Yes	No
Pre-Gearing	No	No	4.8 : 1
Drive Gear	15	15	15 - 23
Driven Gear	60	32-34-36	32-34-36
THK Ball Screw	DK1404-4	DK1404-3	DK1404-3
Lead (mm)	4	4	4
Hip Joints	Pitch	-	Yaw - Roll
Knee Joint	Pitch	-	-
Ankle Joints	-	Pitch - Roll	-

Next, an actuator design was chosen for the Ankle degrees of freedom. This joint would utilize a dual actuation configuration similar to those found on THOR and ESCHER [36], [40], [89]. Here, two actuators will simultaneously manipulate the ankle-pitch and ankle-roll joints. As a result of these actuators working in tandem, the required output force from each actuator is reduced. Despite this, the actuators still required liquid cooling to meet the torque requirements, due to the pre-gearing necessary to meet the speed requirements. This single-motor liquid-cooled actuator was given the designation MKIII Lite. Finally, an actuator for the hip-roll and hip-yaw joints was selected. Both of these joints are relatively low velocity and torque when compared to the others. Therefore, a motor without liquid cooling could be utilized on these joints. However, in order to achieve the required torque, pre-gearing the motor was necessary. This was accomplished by

installing a Maxon GP32 single-stage planetary gearbox with a reduction ratio of 4.8 to 1. This single-motor with pre-gearing actuator was given the designation MKIV Gear. A summary of the finalized actuators specifications and their applicable joint locations can be found in Table 10.

In order to summarize all of the information and design choices from these analyses, theoretical performance diagrams were generated for each actuator concept. These diagrams utilize the theorized performance of the motors and gear train to predict the speed/force operational area of the actuators. The area under the curves given in these diagrams represent the region in which the actuator can operate continuously without overheating or mechanical failure. Included in these diagrams are lines representing the motors speed-torque gradient. This is the mechanical property of the motor in which speed degrades as function of torque. This speed-torque gradient is also a function of temperature; therefore, a line representing the speed-torque gradient and the max allowable winding temperature is also included. The actuator is incapable of achieving any operating points above these speed-torque gradient lines. Also included are lines representing the maximum mechanical limits of the motor. These represent the maximum motor rotational velocity, maximum permissible ball screw rotational velocity, ball screw Permissible Static Load, and the ball screws static load rating. Operating past these lines could result in mechanical failure of components in the actuator. Similarly, lines representing the maximum allowable current, which is dictated by the winding temperature of the motor, were added. These lines are dependent on the cooling conditions around the motors. Operating past these lines could result in motor failure due to overheating. Finally, lines of constant power were added as a quick reference for actuator power at any given operating point on the diagram. The performance diagrams for the MKIII Heavy, MKIII Lite, and MKIV Gear can be found in Figure 11, Figure 12, and Figure 13 respectively.

These plots can also be used to validate the selected actuator designs against the joint requirements. Given a lever arm length, equations (3.11) and (3.12) can be used to convert the gait data into actuator speeds and forces. This gait data can then be plotted directly onto the performance diagram. The particular example given in Figure 14 shows the knee-pitch data for a human and ESCHER plotted on the MKIII Heavy performance plot. It can be noted that there are several data points that violate the maximum output force of the actuator. These points fall to the right of the water cooling line because the knee torque was reduce from 390Nm to 300Nm as stated in section 2.2. Conversely, both speed and peak power requirements are within the operational area.

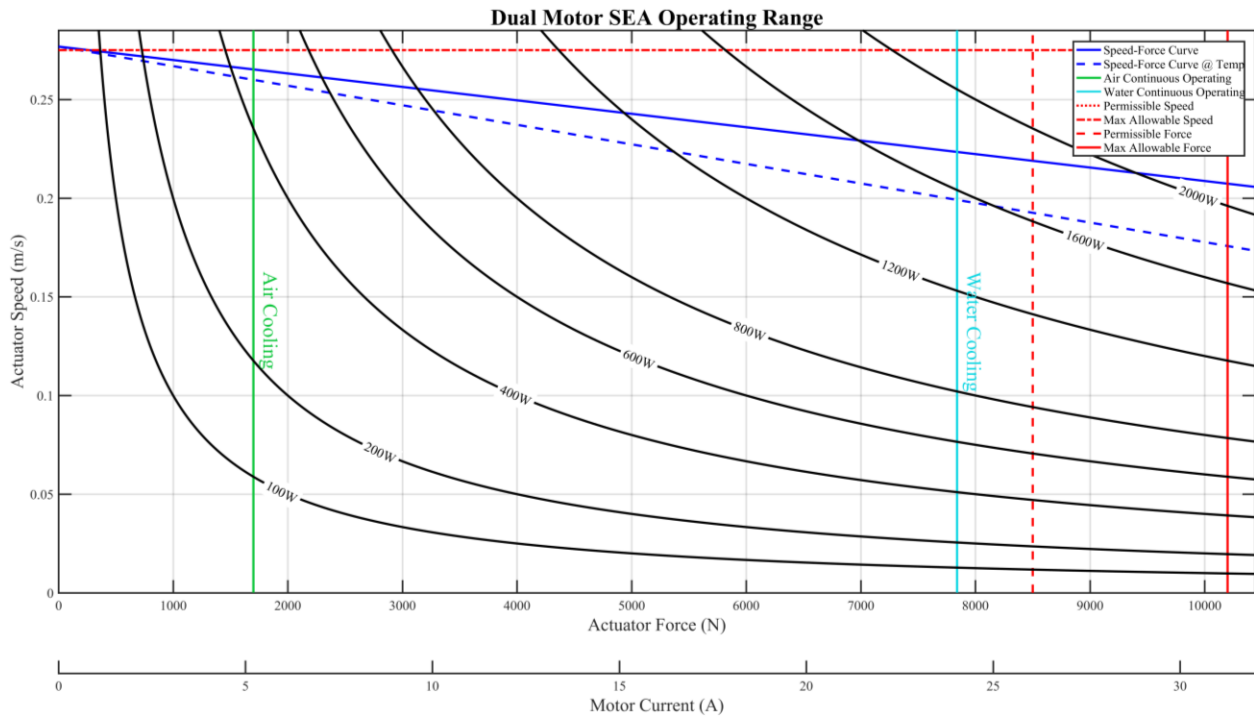


Figure 11: Performance Diagram for a Liquid Cooled Dual Motor LSEA (MKIII Heavy)

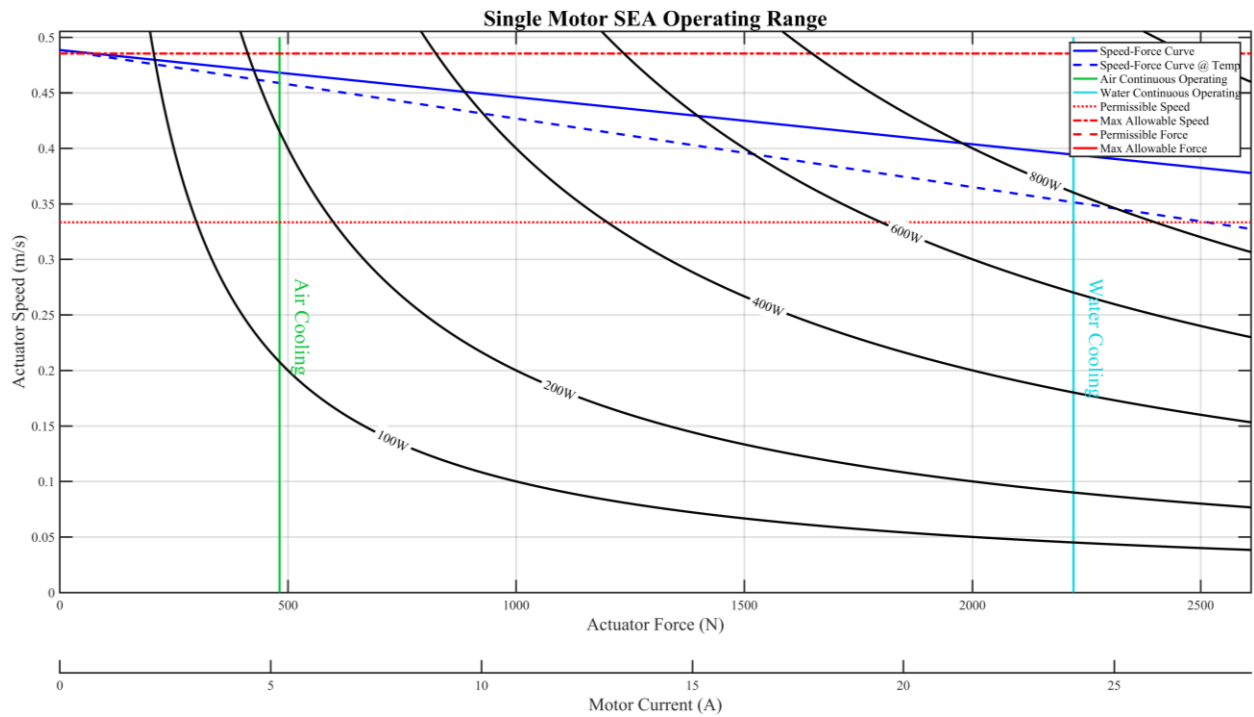


Figure 12: Performance Diagram for a Liquid Cooled Single Motor LSEA (MKIII Lite)

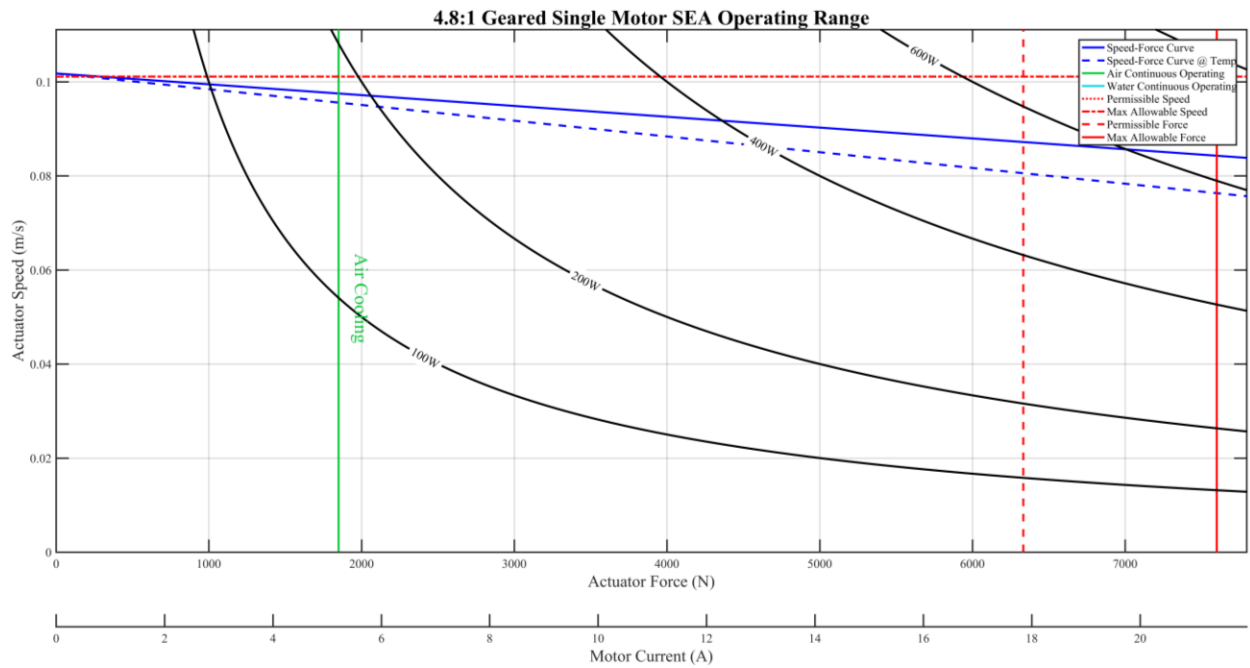


Figure 13: Performance Diagram for a LSEA with a Planetary Gear Box (MKIV Gear)

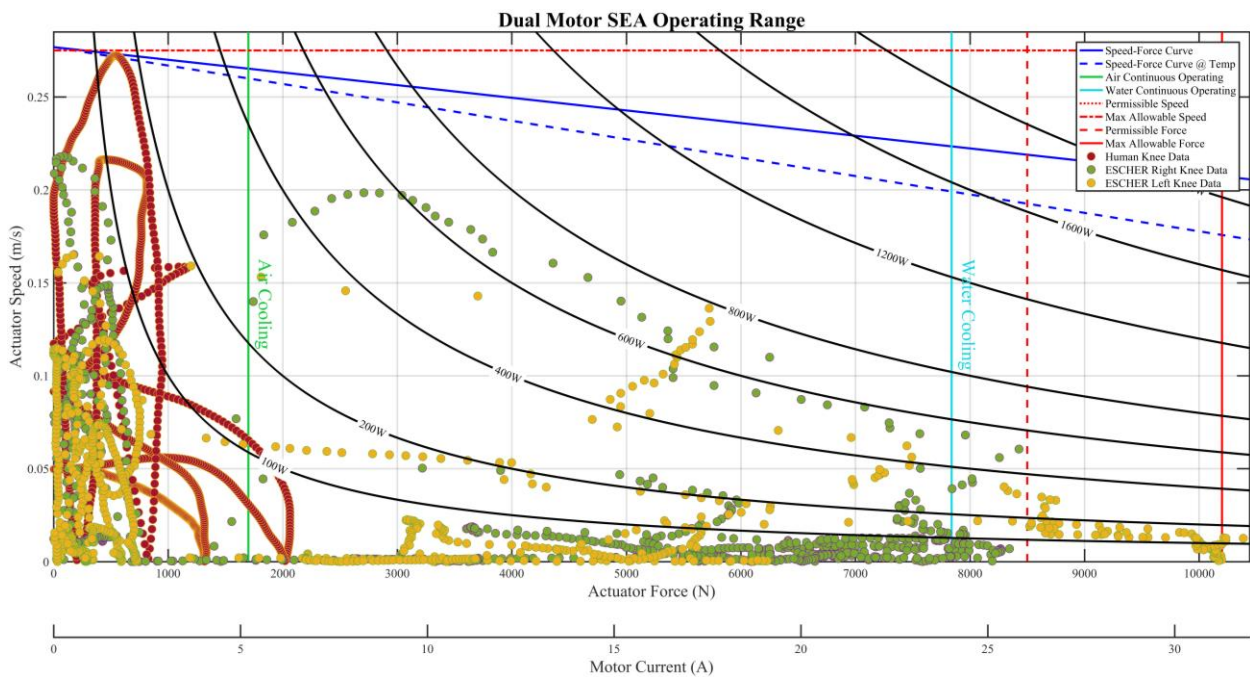


Figure 14: Validation of Knee Joint Requirements and MKIII Heavy Actuator Performance

4. Elastic Element Analysis and Design

The addition of mechanical compliance to an actuator is the defining feature of an SEA. Not only will the properties of the elastic element dictate the performance of the actuator, but also its size and mass. The size of the elastic element can greatly affect the packaging and location of the actuators on the exoskeleton's frame. The material type and configuration can also dictate greatly the mass of the actuator. These factors must be considered when selecting the type of elastic element for the actuator. For this reason, several different spring configurations were analyzed.

The selected LSEA configuration from Chapter 3 limited the types of spring that can be utilized to those that can be loaded in extension or compression. A common low-cost solution used on many LSEA's is die springs [51], [54], [65], [69]. Die springs are designed to be loaded in compression, making them a unidirectional elastic element. In order to deal with bidirectional loading, multiple die-springs are used in pairs. This can lead to bulky and heavy designs in high force applications. Another common spring type used in LSEA's is leaf springs [90]–[93], [38]. Leaf springs can be designed for bidirectional loading, allowing the use of just one spring. An adaptation to this method is the leaf spring with lever arm developed at Virginia Tech [40]. This allows the spring to be placed along the axis of the actuator, thus reducing package size of the actuator. The lever arm also places the spring into pure bend, allowing increased energy storage though the length of the spring when compared to the same spring under shear loading.

The extension or compression of an elastic object, such as a spring, can be directly related to the force required to deform the object. This linear relationship is described by Hooke's Law (4.1), where x is the displacement of the spring during extension/compression, k is the constant of proportionality known as the spring constant, and F is the force required to achieve the displacement x . The spring constant is typically given in units of N/m. However, Hooke's law is only a first-order approximation of the actual response of a spring. This non-linearity of k can affect the performance of the actuator and should be considered when selecting a spring.

$$F = kx \tag{4.1}$$

The following sections detail the analysis conducted to compare different spring configurations for the LSEA. This preliminary analysis was conducted using a target loading of 4400N and deflection of 10mm for a spring stiffness of 440N/mm. Further analysis was conducted to refine the design of the spring and model the spring constant.

4.1. Coil Spring Analysis

Die springs were initially considered for use with the LSEA due to their low cost and OTS availability. However, as product search was conducted, it became apparent that very large die springs would be required. This would lead to a very large package size for the actuator since multiple die springs are required for bidirectional loading. This would also lead to a spring mass well in excess of a kilogram before any mounting features were added. This was seen as an unacceptable amount of mass to add to the actuators.

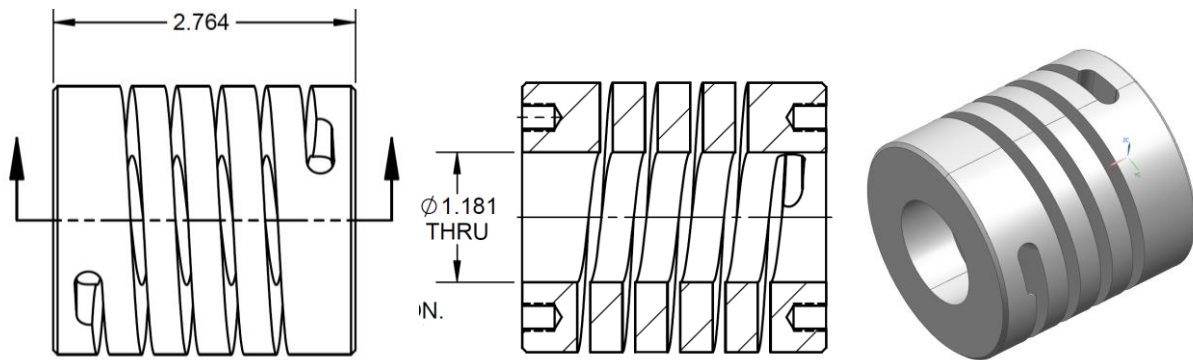


Figure 15: Custom Bi-Directional Coil Spring by Helical

Although die spring were quickly eliminated, other coil spring designs were explored. Machined springs were seen as a possible alternative to die springs. Unlike common coil springs wound from wire or square rod, machined springs are milled from solid bar stock. This allows for many unique features and properties that are not available with common coil springs. This includes specialty alloys and the ability to integrate multiple features into a spring. The integration of structures such as flanges, bearing seats, gears, threads, and other machinable features into a single element reduces the number of parts and simplifies design. For these reasons Helical Products Company, Inc. [94] was contacted and asked to design a bidirectional coil spring with threaded holes on the ends. This would allow the spring to be easily mounted and function in both tension and compress. With the provided load and deflection requirements, Helical developed the bidirectional spring seen in Figure 15. This spring had similar dimensions to the die springs first examined, but was capable of bidirectional loading. The spring was made from C300 nickel maraging steel, which has a considerably high tensile strength of 2135MPa [95]. These details and other spring characteristics are summarized in Table 11. Consequently, the spring still had a hefty mass of 1kg. Again, this was seen as an unacceptable amount of mass, so other options were explored.

Table 11: Helical Bidirectional Coil Spring Properties

Bi-Directional Coil Spring	
Material	C300 Maraged steel
Length (mm)	70.21
O.D. (mm)	62.23
I.D. (mm)	30.00
Volume (cm ³)	213.5
Weight (kg)	1.043
Displacement (mm)	10.00
Max Load (N)	4250±425
Life Cycles	10 ⁶

4.2. Leaf Spring Analysis

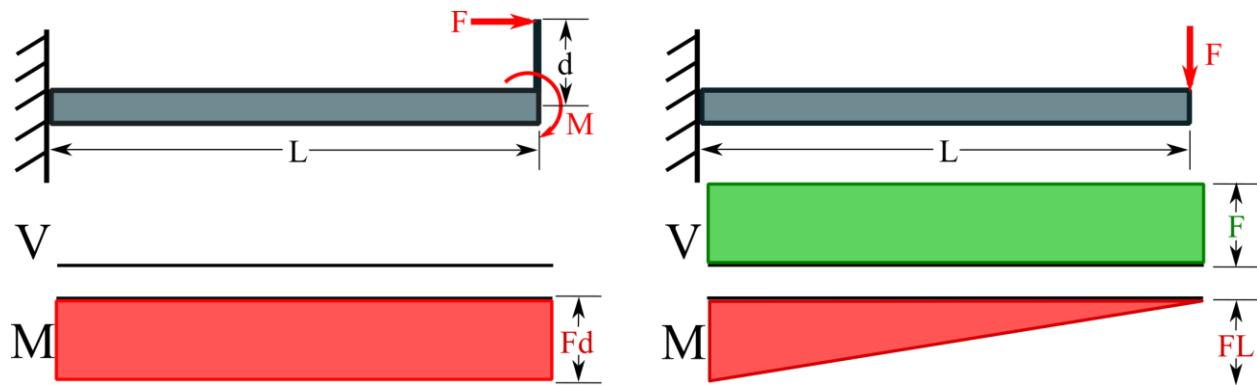


Figure 16: Shear Moment Diagrams for Leaf Spring in Pure Bending and Shear Loading

Leaf springs have the inherent advantage of being capable of bidirectional loading. However, there are no OTS options available for leaf springs, requiring them to be custom fabricated. Advantageously, this allows the material of the spring to be selected, permitting more design options. Analysis was performed on cantilever leaf springs similar to those found on SAFFiR and the parallel leaf springs found on THOR and ESCHER. Several other spring types were also examined for this actuator in [96], but were not capable of the same performance as the cantilever beams. A simple free body diagram and shear moment diagram of these two spring configuration can be seen in Figure 16.

These diagrams demonstrate difference in bending moments M and shear forces V created by the same loading F applied to the two spring configurations. The parallel spring is placed in pure

bending by the moment generated by the lever arm. The resulting bending moment is evenly spread across the length of the beam and is a function of the length of the lever arm F is applied to.

On the other hand, a load directly applied to the end of cantilever beam generates both a bending moment and shear force. The shear force is evenly distributed across the length on the beam while the bending moment is a function of the length L of the beam. This results in the bending moment increasing to a maximum at the farthest point from the input load. Both the bending moment and shear force induce stresses in the beam.

Euler–Bernoulli Beam Theory, also known Classical Beam Theory, describes the relationship between the deflection of a beam and the applied load. Classical Beam Theory can also be used to describe stresses in the beam as well. The equation for bending stress σ_b can be seen in (4.2). Where M is the bending moment, c is the distance from the neutral axis to the surface of the beam, and I is the beams moment of inertia. While the normal stress and shear stress should be examined, they are typically negligible in comparison to bending moment stresses.

$$\sigma_b = \frac{Mc}{I} \quad (4.2)$$

The equation describing the deflection of a cantilever beam like those found on SAFFiR is given in (4.3). Here, F is the applied load, L is the length of the beam, E is the spring material's modulus of elasticity, and I is the beams moment of inertia. Utilizing equations (4.1) and (4.3), the effective spring stiffness of the cantilever beam can be determined by (4.4).

$$\delta_{max} = \frac{FL^3}{3EI} \quad (4.3)$$

$$k_{eff} = \frac{F}{\delta_{max}} \quad (4.4)$$

Classical Beam Theory can also be used to model the parallel leaf springs found on THOR and ESCHER. To determine the effective spring stiffness of the parallel leaf spring, the displacement of both the spring and lever arm must be accounted for. As can be seen in Figure 17, the rotation at B causes the lever arm BC to rotate as well. This results in point C being displaced in both the x and y directions. This displacement is due to the rotation of BC is summed with the springs deflection at B to find the total displacement of point C . The load input angle θ_i was assumed to be 90° during this initial analysis; however, this input angle will become significant when the non-linearity of this configuration is explored.

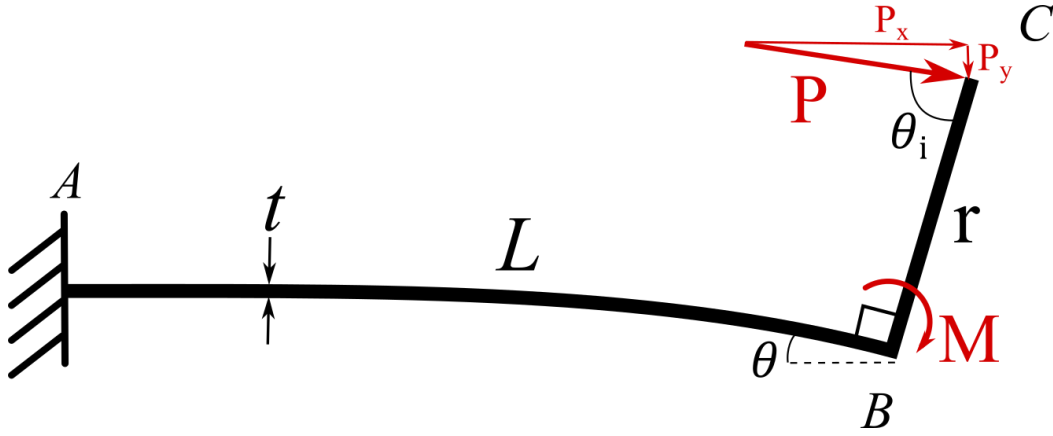


Figure 17: Free-Body Diagram of Cantilever Beam with Lever Arm

The component forces resulting from the load input angle θ_i relative the lever arm are:

$$P_x = P \sin \theta_i \quad (4.5)$$

$$P_y = P \cos \theta_i \quad (4.6)$$

The deflection of point B due to the load components P_x , P_y , and resulting moment M is:

$$\delta_{B_{P_y}} = \frac{P_y L^3}{3EI} \quad (4.7)$$

$$\delta_{B_{P_x}} = \frac{P_x L}{EA} \quad (4.8)$$

$$\delta_{B_M} = \frac{ML^2}{2EI} \quad (4.9)$$

Rotation of the tip due to the load component P_y and resulting moment M is:

$$\theta_{P_y} = \frac{P_y L^2}{2EI} \quad (4.10)$$

$$\theta_M = \frac{ML}{EI} \quad (4.11)$$

$$\theta = \theta_{P_y} + \theta_M \quad (4.12)$$

Displacement of point C in the x and y directions due to the rotation of the lever arm BC is:

$$\delta_{C_x} = r \sin \theta \quad (4.13)$$

$$\delta_{C_y} = r(1 - \cos \theta) \quad (4.14)$$

Total displacement of point C due to deflection of B and rotation of the lever arm BC is found by:

$$\delta C = \sqrt{(\delta B_{P_y} + \delta B_M + \delta C_y)^2 + (\delta B_{P_x} + \delta C_x)^2} \quad (4.15)$$

Finally, the effective spring stiffness resulting from the displacement of C can be determined:

$$k_{eff} = \frac{P}{\delta C} \quad (4.16)$$

These equations were used to examine different spring geometries and materials. One particular material that stood out was titanium. Titanium has a higher yield strength, lower modulus of elasticity, and lower density than steel. These properties make titanium an excellent lightweight spring material that can handle high loads. Titanium was also used as the spring material on all three Virginia Tech humanoids, resulting in the experience and tooling required to produce these springs in house. For these reasons, Titanium Ti-6Al-4V was selected as the spring material. This particular grade of titanium is readily available and has a yield strength approximately 60% greater than steel. Using the material properties found in Table 12, two preliminary leaf spring designs were developed. The characteristics of these springs are summarized in Table 13.

Table 12: Material Properties of Titanium Ti-6Al-4V (Grade 5), Annealed [97]

Property	Value
Density (g/cc)	4.43
Ultimate Strength (MPa)	950
Yield Strength (Mpa)	880
Shear Strength (MPa)	550
Modulus of Elasticity (GPa)	113.8
Shear Modulus (GPa)	44.0
Poisson Ratio	0.342

Table 13: Leaf Spring Properties under 4400N Load

Leaf Spring (Bending)(50mm lever arm)		Leaf Spring (Shear Loading)	
Material	Ti-6Al-4V (Grade 5)	Material	Ti-6Al-4V (Grade 5)
Span (mm)	110	Span (mm)	145
Width (mm)	38.0	Width (mm)	40.5
Thickness (mm)	8.0	Thickness (mm)	10.5
Volume (cm ³)	36.8	Volume (cm ³)	61.6
Weight (kg)	0.148	Weight (kg)	0.273
Displacement (mm)	10.0	Displacement (mm)	10.0
F.S.yield	1.62	F.S.yield	1.00

4.3. Spring Selection

With a preliminary design for each of the spring types generated, a spring was selected by comparing the results in Table 11 and Table 13. The machined spring had the highest package volume and mass between the three springs. The machined spring also had a unit price of approximately \$400 per spring. In comparison, each leaf spring would require \$150 to \$200 of bar stock plus the cost of specialized tooling. However, working with local machine shops the springs could be manufactured for \$250 per unit. Both of these options were significantly cheaper than the machined springs. For these reasons, the machined spring was eliminated, reducing the options to the two leaf spring configurations.

When comparing the two leaf spring designs it can quickly be determined that the spring in pure bending outperforms the spring in shear loading. The lever arm allows a shorter and lighter spring with the same desired spring stiffness. The spring in pure bending also has a much higher yield stress safety factor than the other spring. For these reasons, the parallel leaf spring with lever arm was selected as the compliance configuration for the OLL-E's actuators. However, further analysis was required in order to characterize and design the springs.

4.4. Finite Element Analysis and Finalized Design of Leaf Springs

While Classical Beam Theory can be used to estimate spring performance, it does not capture all the features that will be present on the spring. Features such as bolt holes and fillets will be required in the final design of the spring. These features create stress concentrations that can cause a failure long before the maximum bending stress is reached. In order to develop the final design of the leaf spring, finite element analysis (FEA) was utilized. FEA is a computer-aided engineering (CAE) method that can be used to predict the performance of a structure. This modeling also permits the examination of stress concentrations, the interactions between components, and can be used to verify the analytical model developed in Section 4.2. These FEA analyses were conducted using Siemens ABAQUS CAE 2016.

A critical step in the FEA process is selecting the type of element applied to the meshed 3-D model. One possible element for 3-D modeling is fully integrated linear hexahedral elements (C3D8). However, elements with large aspect ratios can suffer from shear locking, leading to inferior results. Hexahedral elements that can reduce shear locking are Reduced Integration (C3D8R) and Incompatible Mode (C3D8I) [98]–[100]. The C3D8R has the advantage of greatly

reducing solution times, but can suffer from hourglassing that leads to a reduction in element stiffness. C3D8I has an additional degree of freedom to better model the displacement gradient through the element, but suffers from sensitivity to element distortion resulting in the elements acting too stiff. In order to expedite the iterative design process, the reduced integration element C3D8R was utilized. In total, over 60 FEA models and cases were analyzed before the two spring designs were finalized.

Due to the large variation in actuator requirements, two different springs were developed; one for low-force actuators and one for high-force actuators. The MKIII Heavy actuator utilizes the high-load spring while the MKIII Lite and MKIV utilize the low-load spring. Based on actuator requirements, the MKIII spring must be capable of handling $\pm 7000\text{N}$ under normal operating conditions. Likewise, the MKIV spring must be capable of handling a $\pm 4800\text{N}$ load. Based on previous work with THOR and ESCHER, the preliminary spring stiffness was changed to 500N/mm . This is approximately the average of the two stiffness settings found on THOR and ESCHER's LSEA [42], [43].

4.4.1. MKIV and MKIII Lite Spring

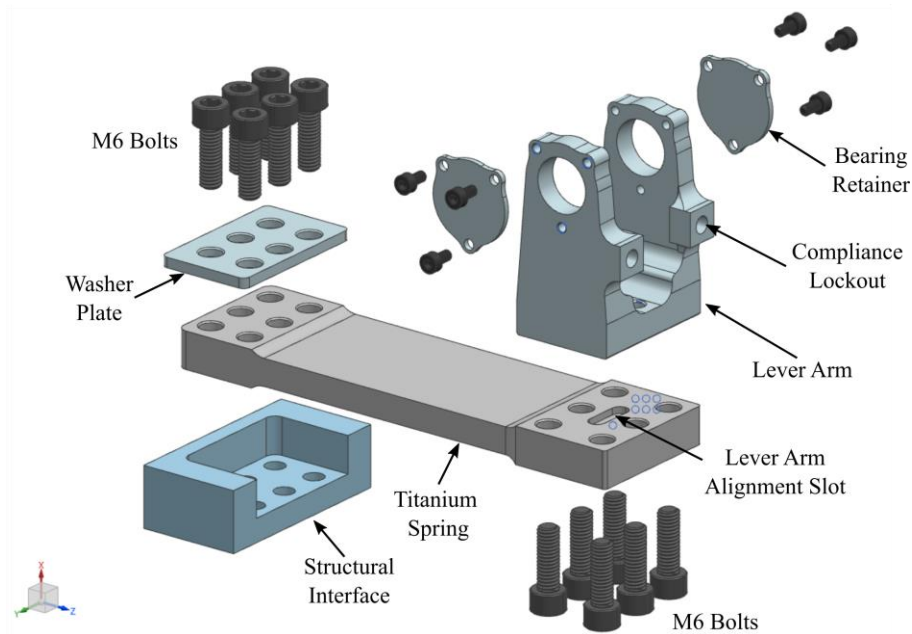


Figure 18: Exploded view of MKIV Spring Assembly

In order to fully capture the performance of the spring and the interactions between the various components, the entire spring assembly was modeled in ABAQUS. These components included

the spring, lever arm, bolts, washers, and mounting interface with the exoskeleton. This allowed of the components to be simultaneously examined. The full MKIV spring assembly can be seen in Figure 18. When comparing this to the ABAQUS assembly in Figure 19, simplification to the geometry can be noted. The removal and simplification of features was done in order to ease the partitioning and meshing process. These removed features were considered non-critical to the design of the spring.

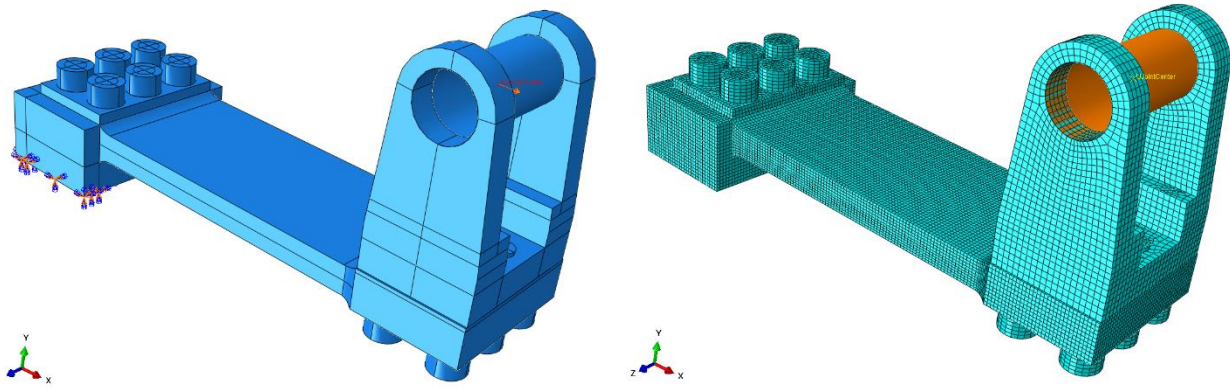


Figure 19: ABAQUS FEA Model of MKIV Spring Assembly

A central characteristic of this FEA model was the inclusion of the bolted joints between the lever arm, mount fixture, and the spring. This was done to better understand how the load would be transferred into the spring from the bolts. This area of the spring was also most likely to have stress concentrations due to the bolt holes through the spring. This also has the added effect of incorporating joint stiffness into the predicted deflection of the trunnion.

As predicted, stress concentrations around the bolt holes were the predominate failure mode. In order to remove these stress concentrations, the thickness of the spring was increased at the mounting areas on the ends of the spring. A fillet was used to transition between the two profiles and prevent corner stress concentrations, which resulted in the spring having a dog-bone shaped cross-sectional area. Although the increase in thickness reduced the stress concentrations, it also stiffened the spring. In order to maintain the desired deflection, the leaf of the spring length had to be increased. Without FEA, these stress concentrations and the resulting design changes to remedy them would not have been identified, highlighting the importance of a multi-faceted approach.

The Final FEA results for deflection, von Mises stress, and the absolute max principle stress can see seen in Figure 20 , Figure 21, and Figure 22 respectively and are summarized in Table 14.

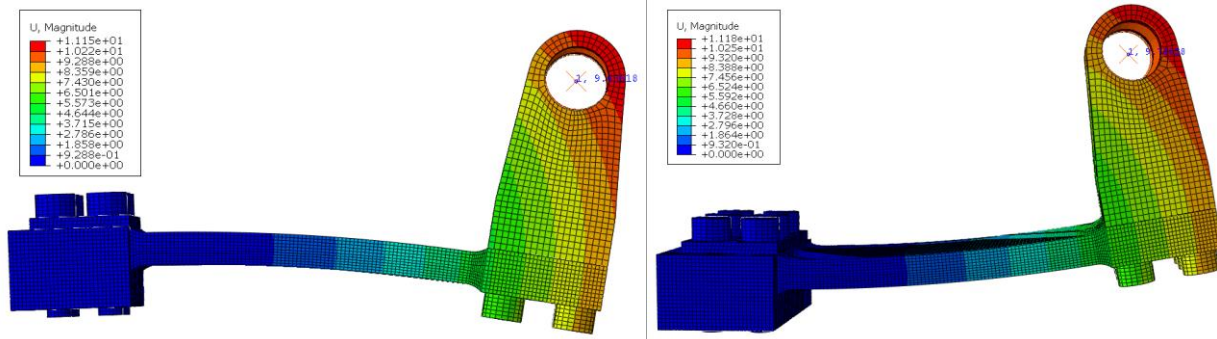


Figure 20: Deflection at U-Joint Center under $\pm 4800\text{N}$ Loading

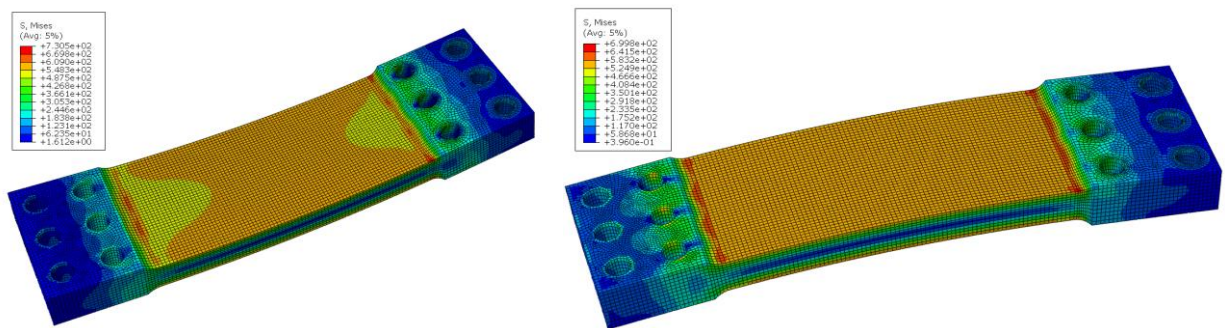


Figure 21: von Mises Stress under $\pm 4800\text{N}$ Loading

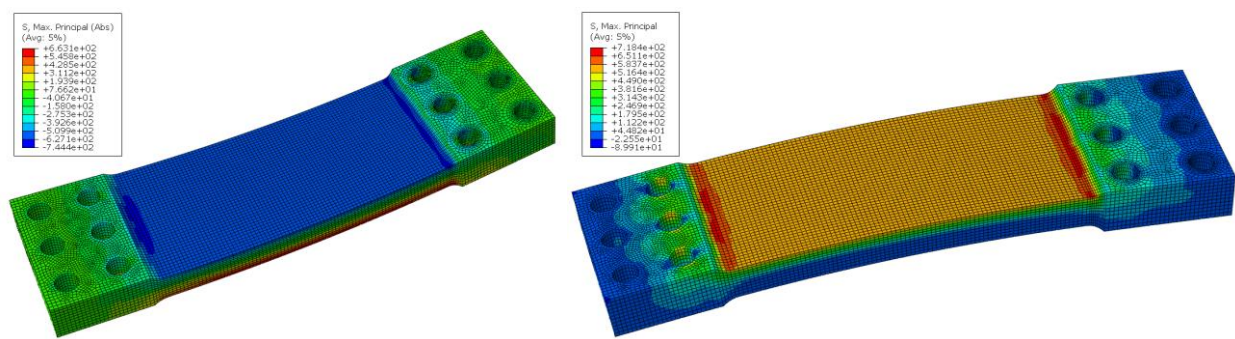


Figure 22: Max Principal Stress under $\pm 4800\text{N}$ Loading

Table 14: MKIV Spring FEA Results

Case	+4800N	-4800N
Mises Stress (MPa)	730.5	699.8
Principal Stress (MPa)	744.4	718.4
Model Convergence	3.0%	3.1%
Deflection (mm)	9.64	9.74
Spring Stiffness (N/mm)	498.1	492.8

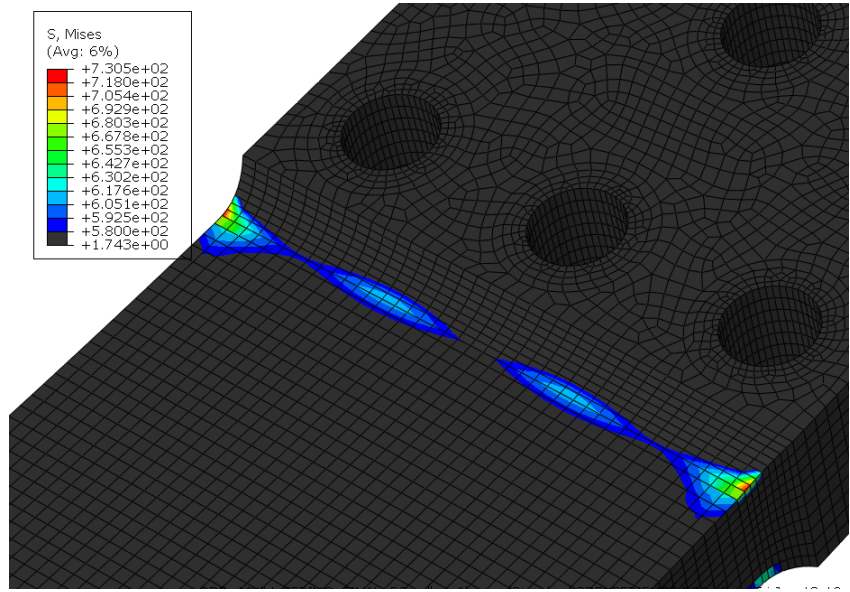


Figure 23: Stress Concentrations on MKIV Spring

Although the increased thickness at the end of the springs removed the stress concentrations around the bolt holes, new concentrations developed on the fillet between the spring area and lever arm-mounting pad. Using Grade 5 Titanium’s yield strength of 880 MPa, the yield safety factor was calculated. The elements shown in Figure 23 are under compression and have a yield safety factor of approximately 1.2. Examining the bending stress in the middle of the spring yielded a safety factor of 1.5. The spring also has a spring stiffness of approximately 495.5N/mm at maximum loading.

In order to assure the mesh applied to the model was not affecting the solution, the model was re-meshed with smaller elements until the maximum stresses converged to within 10%. This convergence was determined by examining the percent difference between the maximum stresses of each run. Further mesh refinements were made around the bolt holes and fillets to ensure stress concentrations were fully captured. The final convergence of the model was determined to be 3%.

4.4.2. MKIII Heavy Spring

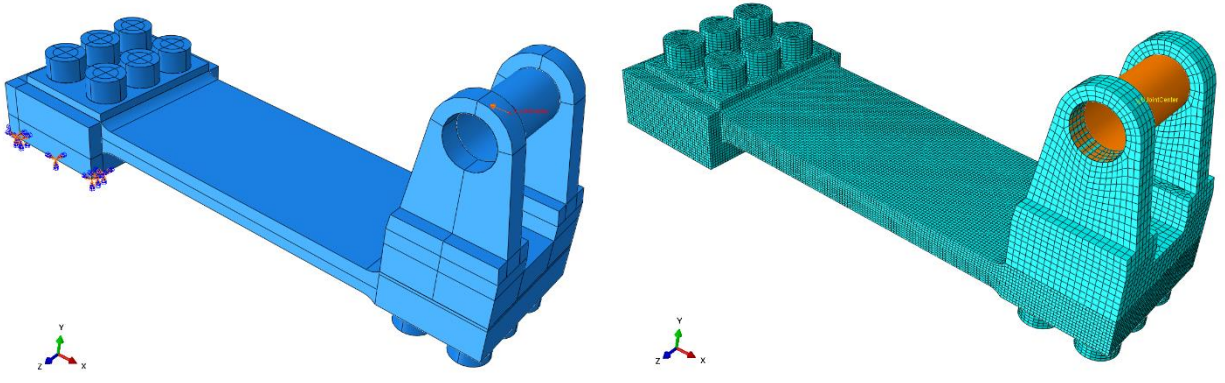


Figure 24: ABAQUS FEA Model of MKIII Spring Assembly

Like the MKIV, the MKIII spring shares all of the same characteristics and features. However, the MKIII spring is wider, thicker, and longer than the MIV spring. This is due to the much higher loading of 7000N this spring must endure. The bolts were also increased in size from M6 to M8 to handle the higher loading. Finally, the base of the lever arm was widened, allowing more material to accommodate the larger bolts and increased its strength. The final FEA results for deflection, Von Mises stress, and the absolute max principal stress are summarized in Table 15 and can be seen in Figure 25, Figure 26, and Figure 27 respectively.

Unlike the MKIV spring, the MKIII spring still had stress concentrations around the bolt holes after thickening the ends of the spring. The elements shown in Figure 28 are in tension and have yield safety factor of approximately 1.25. Examining the bending stress in the middle of the spring yielded a safety factor of 1.4. The spring also has a spring stiffness of approximately 496N/mm at maximum loading. The final convergence of the model was determined to be approximately 1%.

Table 15: MKIII Spring FEA Results

Case	+7000N	-7000N
Mises Stress (MPA)	706.3	633.1
Principal Stress (MPA)	723.9	693.8
Model Convergence	0.3%	1.1%
Deflection (mm)	14.03	14.19
Spring Stiffness (N/mm)	499.0	493.2

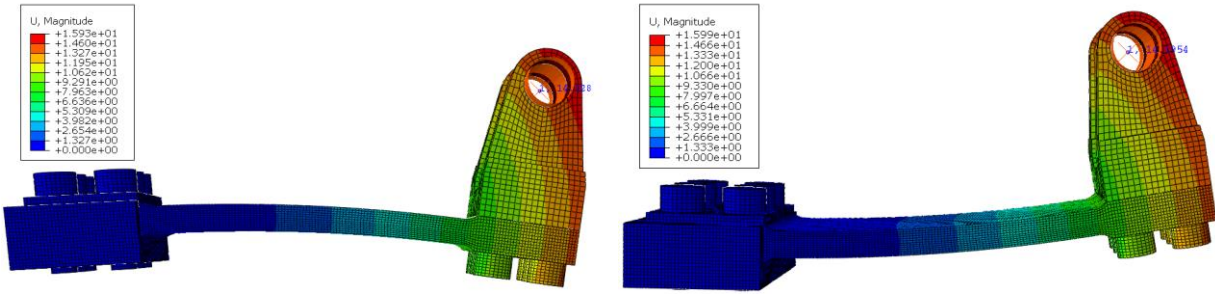


Figure 25: Deflection at U-Joint Center under $\pm 7000\text{N}$ Loading

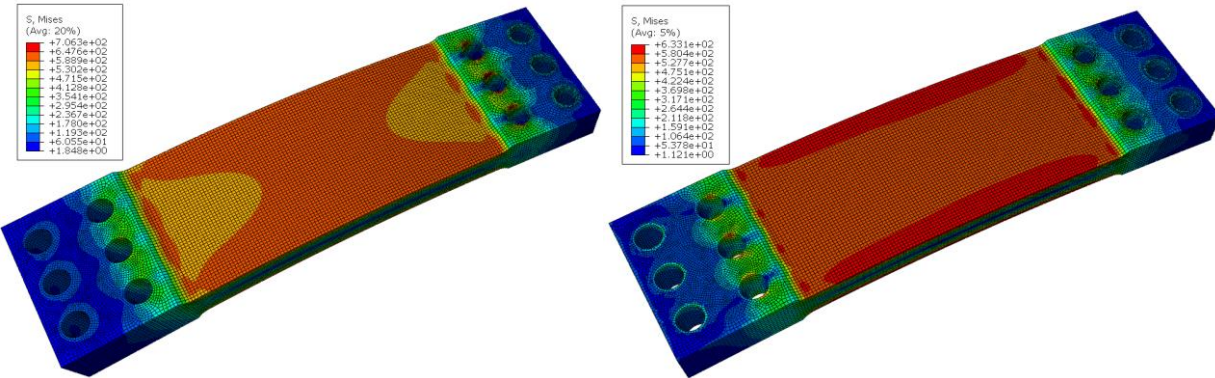


Figure 26: von Mises Stress under $\pm 7000\text{N}$ Loading

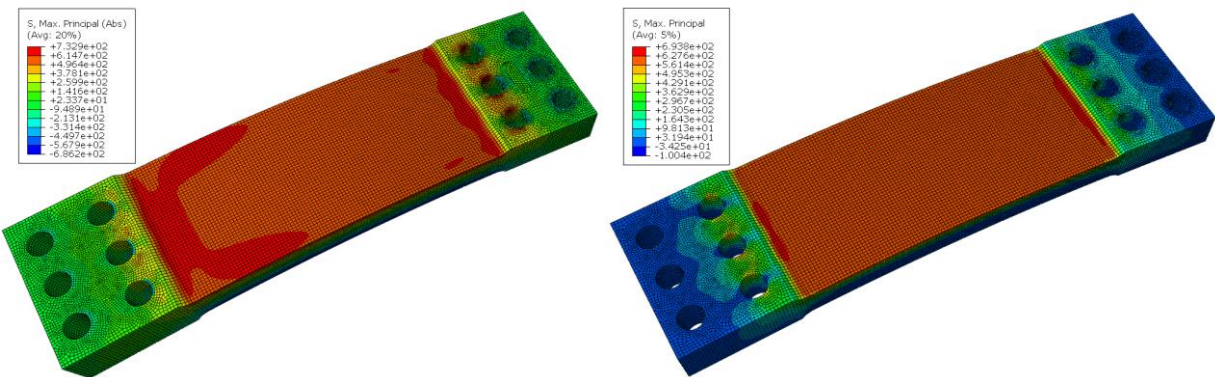


Figure 27: Max Principal Stress under $\pm 7000\text{N}$ Loading

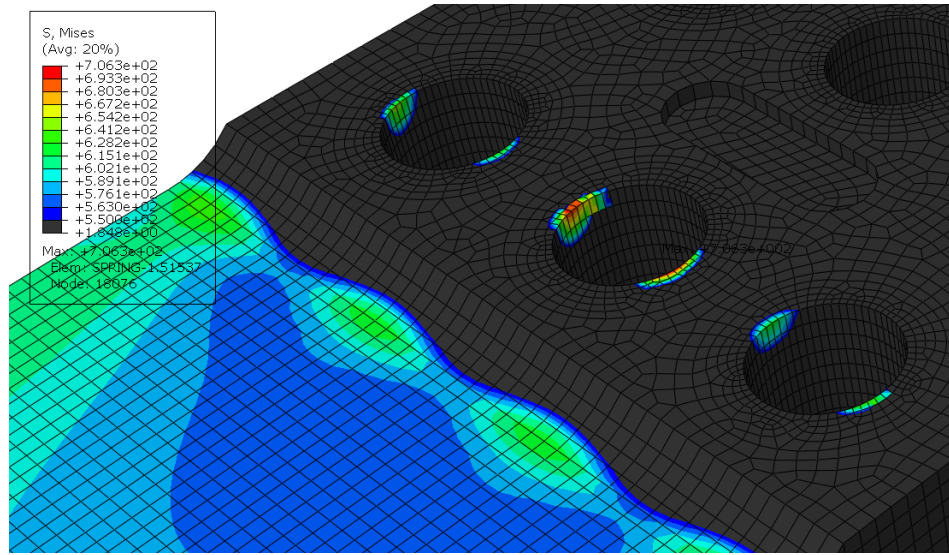


Figure 28: Stress Concentrations on MKIII Spring

4.5. Spring Stiffness Analysis

Utilizing FEA, the design of the leaf spring was finalized. However, due the amount of time required for each FEA run, only the maximum load cases were analyzed. In order to understand the performance of the spring between no-load and maximum loading, the analytical model discussed in section 4.2 was utilized. These equations, however, required several simplifications be applied to the finalized dimensions of the leaf spring and lever arm. Due to the mounting features on the ends of the spring, the length of the active span of the spring was approximated as the distance from the fillet at the base to the centerline of the lever arm. The length on the lever arm was assumed to be the distance from the central axis of the spring to the centerline of the trunnion bearing. Using theses approximated dimensions, the deflection path of the trunnion at the top of the lever arm was analyzed. The displacement components seen in equation (4.15) were plotted in an x versus y displacement plot. The spring stiffness was calculated using the magnitude of these displacements and equation (4.16) and then plotted against the input load.

Observing the spring stiffness in Figure 29 and Figure 30, it can easily be seen that the spring stiffness are nether constant or linear. This is an important revelation, as the spring stiffness strongly influences the plant dynamics that must be compensated for by the controller [42]. A variation of 8.4% in spring stiffness occurs between the maximum load cases for the MKIII spring. A similar variation of 6.5% can be seen in the MKIV spring. Previous modeling of this spring configuration for THOR and ESCHER had assumed a constant spring stiffness.

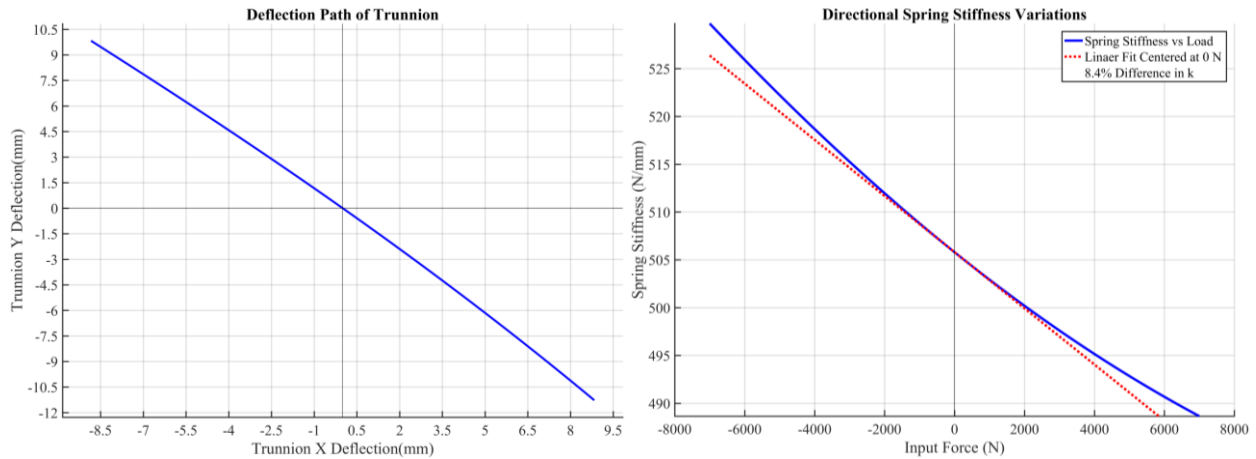


Figure 29: Deflection Path and Spring Stiffness of MKIII Spring due to $\pm 7000\text{N}$ Loading

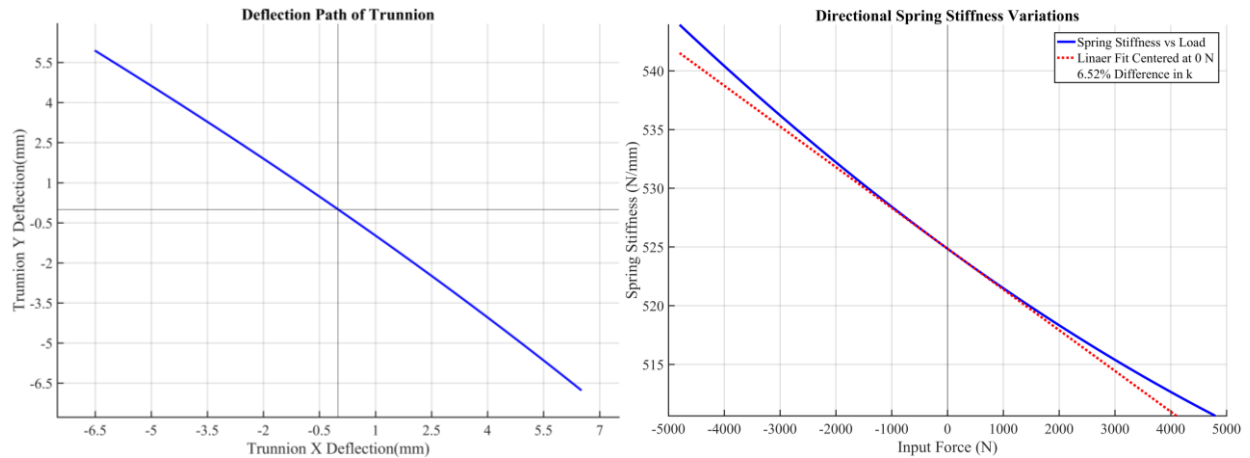


Figure 30: Deflection Path and Spring Stiffness of MKIV Spring due to $\pm 4800\text{N}$ Loading

This variation in spring stiffness is inherent to the geometry of the lever arm. Three major components contribute to the magnitude of deflection. These components are the deflection of the spring tip in the y direction, displacement of the lever arm in the y direction, and displacement of the lever arm in the x direction. During positive loading, all three components contribute to the overall magnitude of the deflection. However, when the load is applied in the negative direction, the y components counteract each other, resulting in a smaller overall magnitude of deflection. This is reflected in the stiffness, where positive loading has a decreasing stiffness (more deflection) and negative loading has an increasing stiffness (less deflection).

However, the results presented thus far have one critical assumption; the applied load is perpendicular to the lever arm. This will not be the case during normal operation of the actuator. Combining the free body diagrams of the spring, actuator, and exoskeleton joint in Figure 31, we

can observe how θ_i varies. In this particular example, the lever arm DE rotates around point E and θ_j increases, resulting in θ_i decreasing. However, depending on the geometry of the joint and location of actuator, this angle could also increase beyond 90° . As a result, the load component P_y is generated as described in equation (4.6). This load component produces a deflection and rotation at the spring tip that can contribute to or counteract the overall y deflection and rotation θ ; recall equations (4.7) and (4.10). This only exacerbates the non-linearity of this spring configuration, results in a spring stiffness that is relatively sensitive to the geometry of the joint and its effects on the input load angle θ_i .

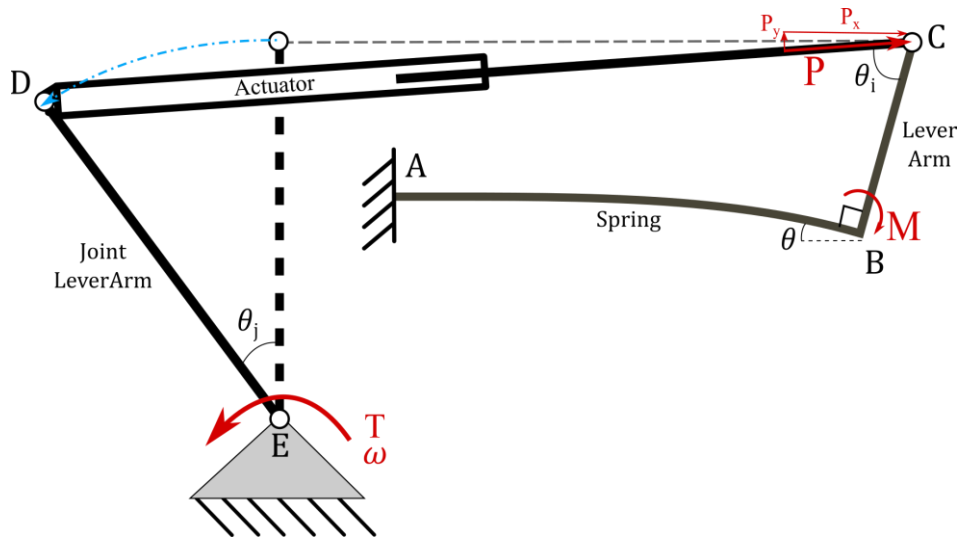


Figure 31: Free Body Diagram of Actuator and Parallel Leaf Spring

The current design of the hip yaw joints on the exoskeleton have an input angle between 90° and 86° , or a delta of 0 to 4° [96]. The design of the lower legs is in progress and no joint geometry currently exists. To fully map the performance of the leaf spring, both the load and input angle must be varied in the model. Therefore, the maximum input angle for the model was assumed to be $\pm 8^\circ$. Operating points beyond this range were considered extreme and should be avoided.

Using this two-dimensional parameter space, the trunnion deflection, spring stiffness, and bending stress were computed. These results were then mapped on contour plots, where the vertical axis is the input angle, the horizontal axis is the load, and the iso-response values represent the dependent variable, such as deflection. The predicted trunnions deflection for the MKIII and MKIV springs can be seen in Figure 32 and Figure 33, as well as spring stiffness Figure 34 and Figure 35. Finally, the estimated bending stress for each spring is shown in Figure 36 and Figure 37.

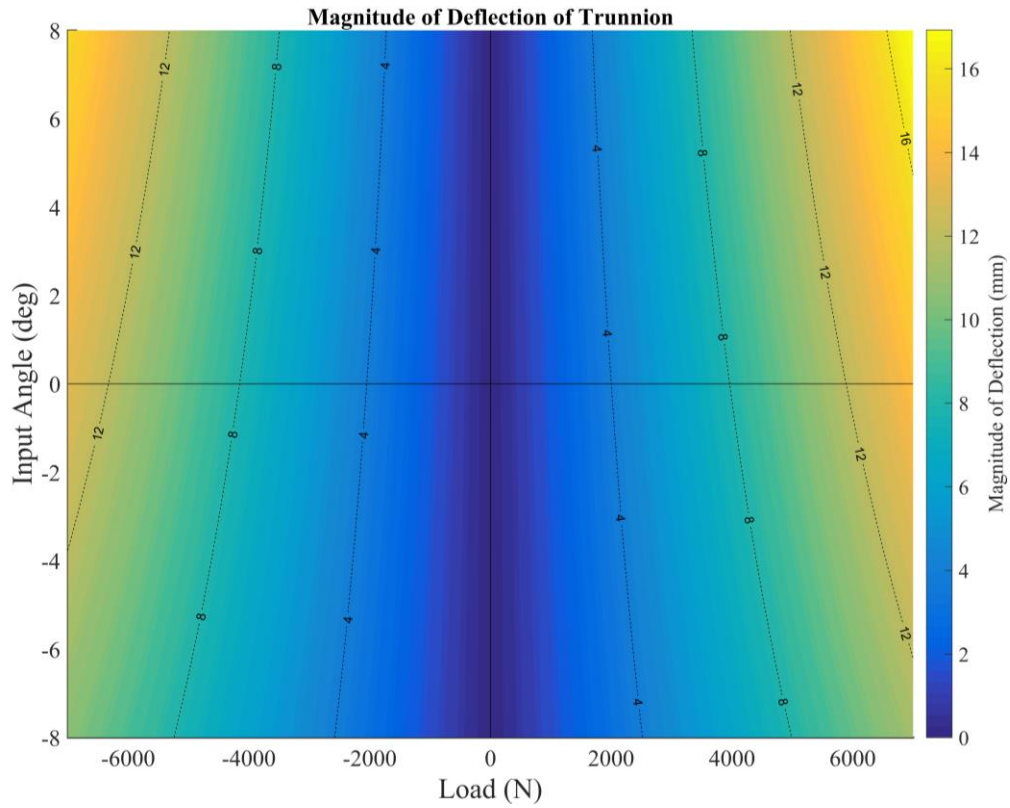


Figure 32: MKIII Spring Deflection Given Input Load and Angle

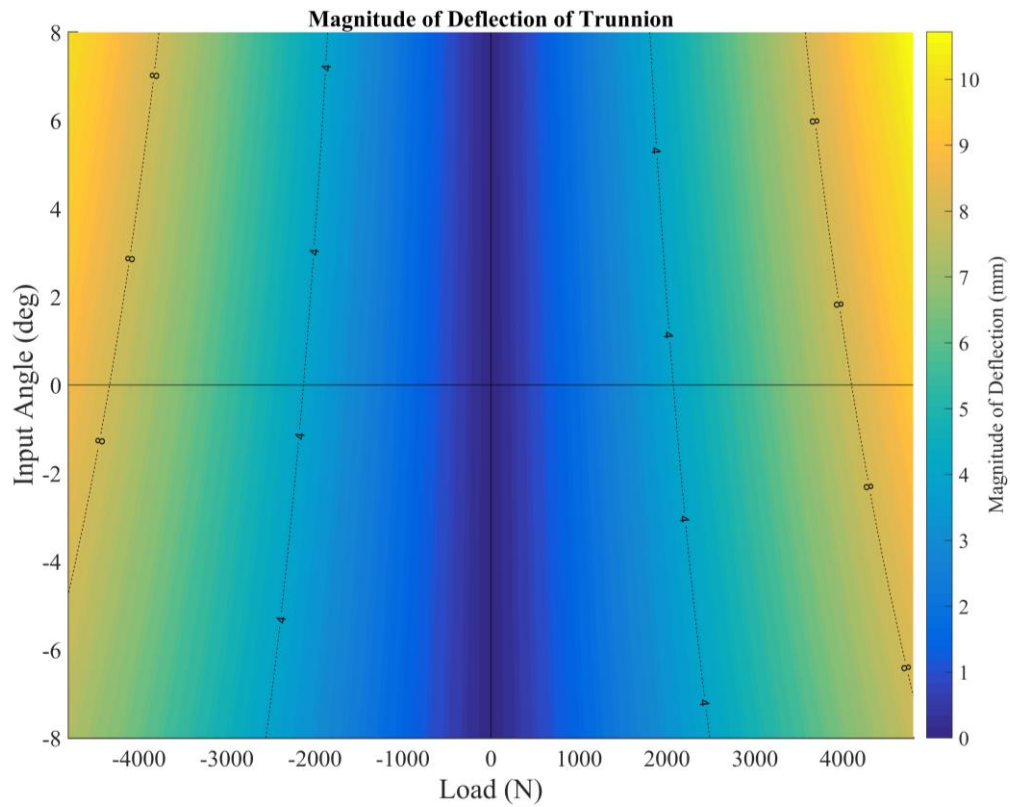


Figure 33: MKIV Spring Deflection Given Input Load and Angle

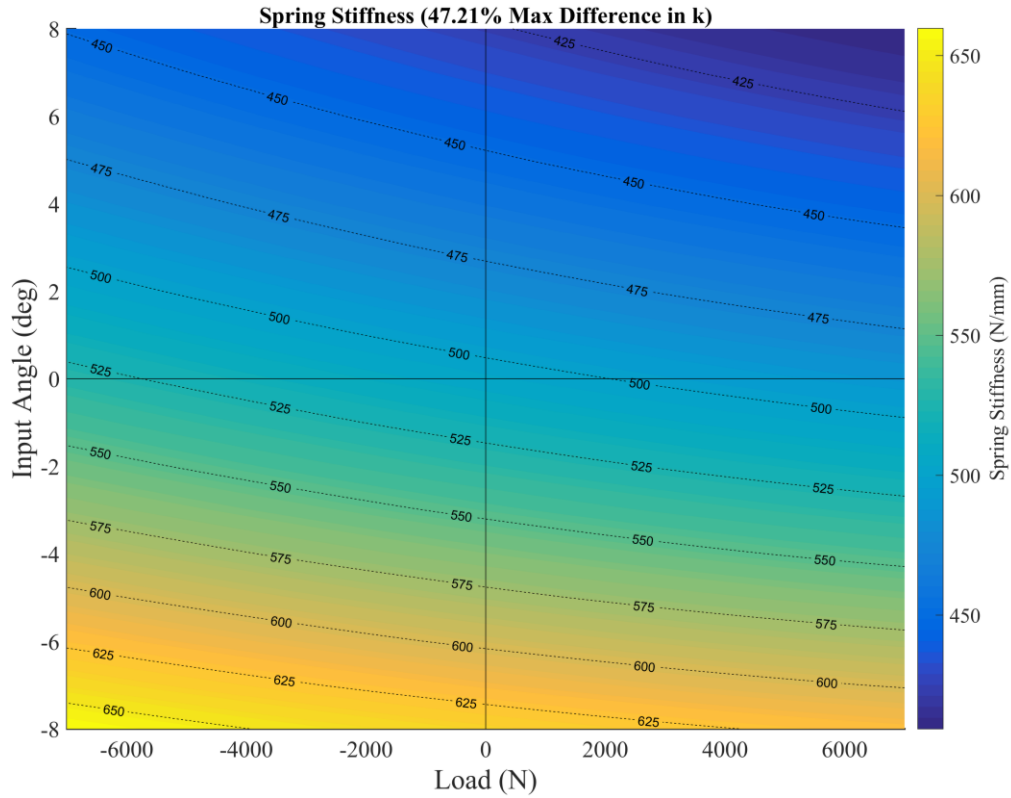


Figure 34: MKIII Spring Stiffness Given Input Load and Angle

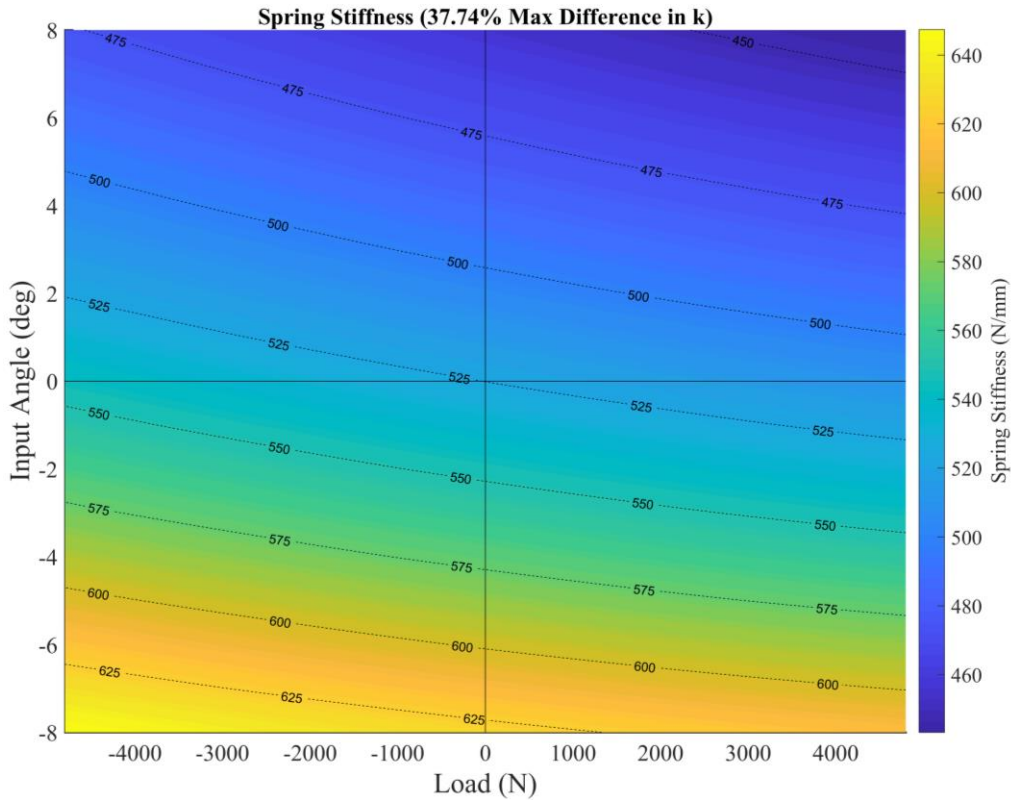


Figure 35: MKIV Spring Stiffness Given Input Load and Angle

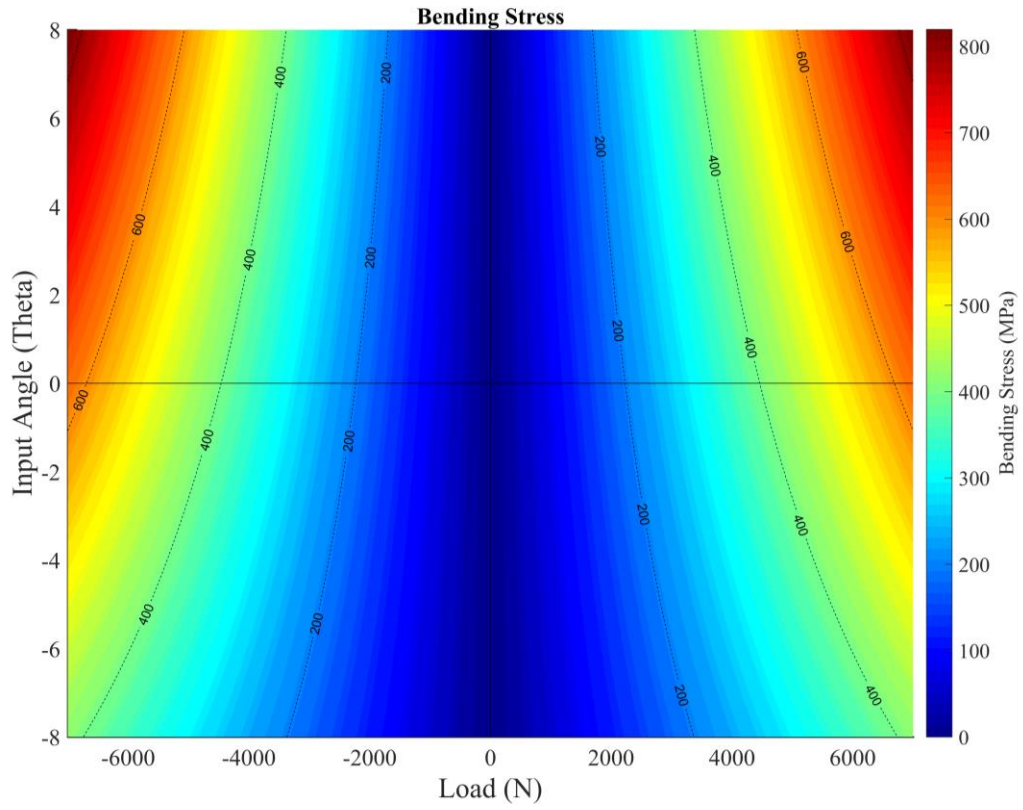


Figure 36: MKIII Bending Stress Given Input Load and Angle

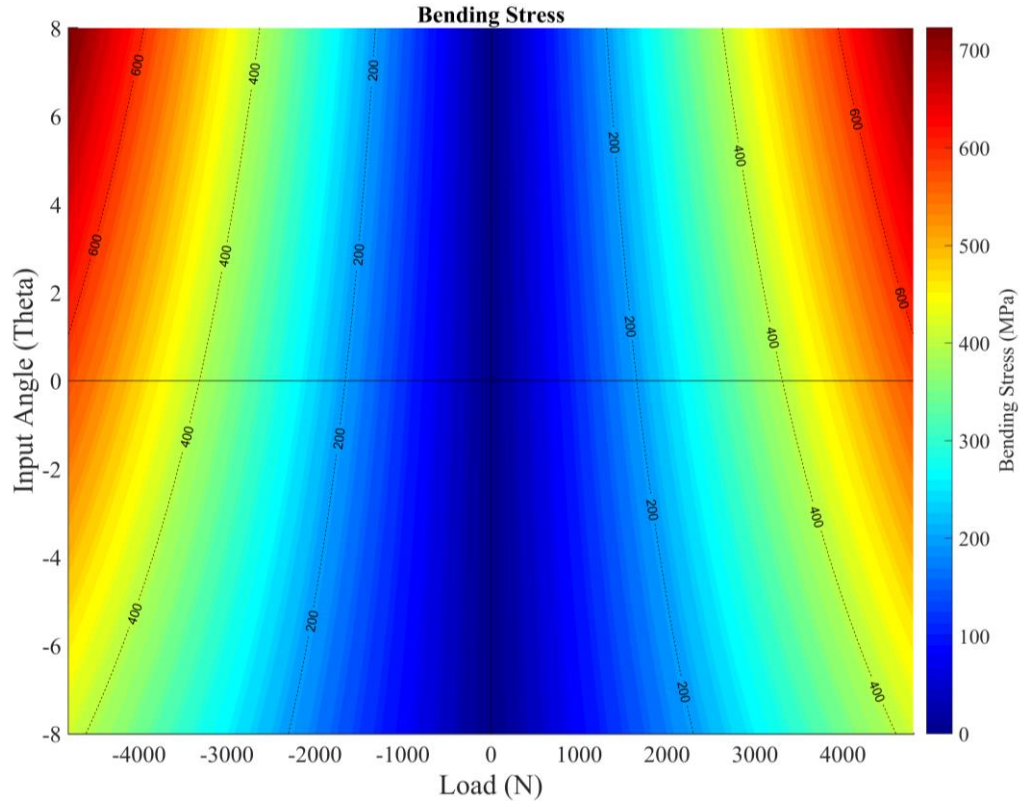


Figure 37: MKIV Bending Stress Given Input Load and Angle

As can be seen in Figure 34 and Figure 35, the difference in spring stiffness across the operational area is significant. The spring stiffness of the MKIII spring fluctuates over 250N/mm, resulting in a 47% change in spring stiffness across the operating area. Similarly, the MKIV spring stiffness changes up to 200N/mm for a max difference of 38%. While these fluctuations are significant across the analyzed operational area, it is unlikely an actuator will experience these extremes changes. For example, the hip yaw actuators operate within 0 to 4°, or just one quarter of the shown operation area in Figure 35. However, this smaller operating area still has a spring stiffness fluctuation of 18%. Joints with large ranges of motion and/or long lever arms will have a larger operational area. Preliminary work on the exoskeleton leg suggests the input angle may vary up to 8 or 10°, which would constitute half the operational area displayed in the plots.

The bending stress in the spring was also estimated. While the analytical model cannot predict stress concentrations, it can be used to approximate failure from bending. Examining Figure 36 and Figure 37, it can be seen that the stress also fluctuates with input angle. Near the extreme ends of the operating area, the stress rapidly increases. As these zones are approached, the spring yield safety factor falls below 1.1. It is interesting to note that given the proper combination of variables the stress in the spring can be reduced even under maximum loading, but comes at the cost of increasing (stiffening) the spring stiffness. However, this revelation opens up the possibilities of allowing the peak stress and spring stiffness to be selected based on the geometry of the joint.

The opportunity of having control over when peak operating points are reached is noteworthy. For example, the geometry of the actuator and joint could be configured in such a way that peak loading occurred while the input load was at an angle that reduced the stress in the spring, resulting a higher yield safety factor being maintained. If the joint angle at which at which maximum torque occurs is determined, then the desired joint geometry could then be derived. This joint angle could be determined by examining the walking data discussed in section 2.1. The joint angle at which peak torque occurs could then be incorporated into the actuator requirements

With this information and the methods discussed in previous sections, a full analytical model of the exoskeleton joint-actuator-spring system can be created. This model could be used to predict the performance, operational area, and critical points of the joint and spring. It could also be used to understand how design decisions effect the other aspects of the system and where refinements in the design of the exoskeleton can be made.

4.6. Comparison of Analytical Model and FEA

In order to understand how well the simplified geometry used in the analytical model represented the final spring design, the results of the analytical model and FEA were compared. This was done by comparing the maximum deflection, spring rate, and peak stress. Another critical difference between the models is the incorporation of the bolted joint stiffness in the FEA model. To see how bolted joint stiffness affected the deflection, two additional FEA cases were generated. In these cases, the bolted joint at the base of the spring was removed and replaced with an encastred constraint. This eliminated one of the two bolted joints in the model. The lever arm remained bolted to the top of the spring due to being part of the load input path. This case was also compared against the analytical model. The results from these three cases are summarized in Table 16 for the MKIV and Table 17 for the MKIII.

Table 16: MKIV Spring Model Results Comparisons

MKIV Spring	Euler Bernoulli	FEA Fixed Base	% Error	FEA Bolted Base	% Error
Deflection (mm) -4800N	8.8	8.9	1.1%	9.7	10.2%
Deflection (mm) +4800N	9.4	9.1	3.2%	9.6	2.1%
Avg. Spring Rate (N/mm)	527.5	533.3	1.1%	497.4	5.7%
Stress (MPa) -4800N	579.4	678	17.0%	678	17.0%
Stress (MPa) +4800N	579.4	708	22.2%	709	22.4%

Table 17: MKIII Spring Model Results Comparisons

MKIII Spring	Euler Bernoulli	FEA Fixed Base	% Error	FEA Bolted Base	% Error
Deflection (mm) -7000N	13.2	13.3	0.8%	14.2	7.6%
Deflection (mm) +7000N	14.3	13.4	6.3%	14.0	2.1%
Avg. Spring Rate (N/mm)	509.1	524.3	3.0%	496.5	2.5%
Stress (MPa) -7000N	627.8	649	3.4%	626	0.3%
Stress (MPa) +7000N	627.8	705	12.3%	704	12.1%

Examining the two tables, several trends can be noted. The FEA model with an encastré fixed base has the highest spring rate of the three cases. This is to be expected, as the thicker spring ends are likely stiffening the spring and any deflection of the mount or stretching in the bolts has been removed. Conversely, the cases including both bolted joints had the lowest spring stiffness. The highest deflection errors were seen in these cases. Again, this is likely due to the stiffness of the bolted joint. In particular, the maximum errors were both seen in the negative load cases. This is likely due to the fact the spring is twisting up against the bolts under this loading. By manipulating the counter scales in the FEA results, we can examine the displacement around the base of the spring. Examining Figure 38, the deflection of the spring and bolts for both configurations is approximately 0.05mm. Small displacements at the base of the spring are amplified by the geometry of the spring to where they are measured at the trunnion.

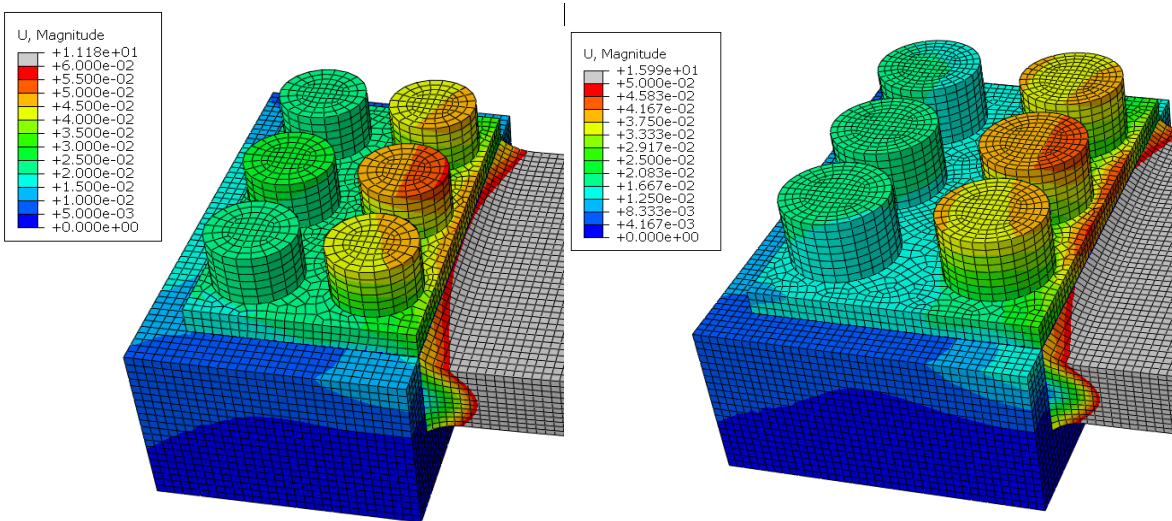


Figure 38: Deflection of Bolted Joint at the Base of the MKIV and MKIII Springs

Observing the predicted maximum stresses between the models, large errors can be seen. However, these maxima include stress concentrations and do not represent the bending stress in the active span of spring. Again, the contour scales in the FEA model were manipulated so the bending stress could be examined. This was done by setting the maximum stress value equal to the bending stress predicted by the model. If the bending stress of the active span in the FEA model is equal to the predicted stress it will be colored red. Any stress value exceeding this limit will be colored light gray. Examining Figure 39 and Figure 40, the bending stress in the active span is shown to be equal to or less than the predicted stress. This is also confirmed by the -7000N load

case results seen in Table 17. This particular case did not have any notable stress concentrations in the FEA model. With bending dominating the stress results, the error between the three models was quite low. Therefore, the model can be used to predict the maximum expected bending stress in the spring. This is very usefully during the preliminary design process as good initial spring design can reduce the number of FEA runs required to finalize a design. The model can also be used to generate design requirements and explore material options.

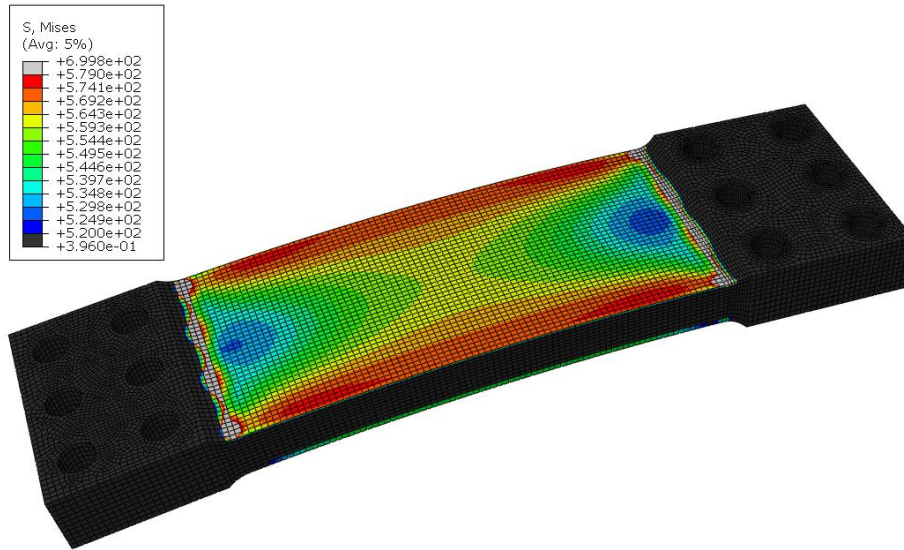


Figure 39: Bending Stress in Active Span of MKIV Spring

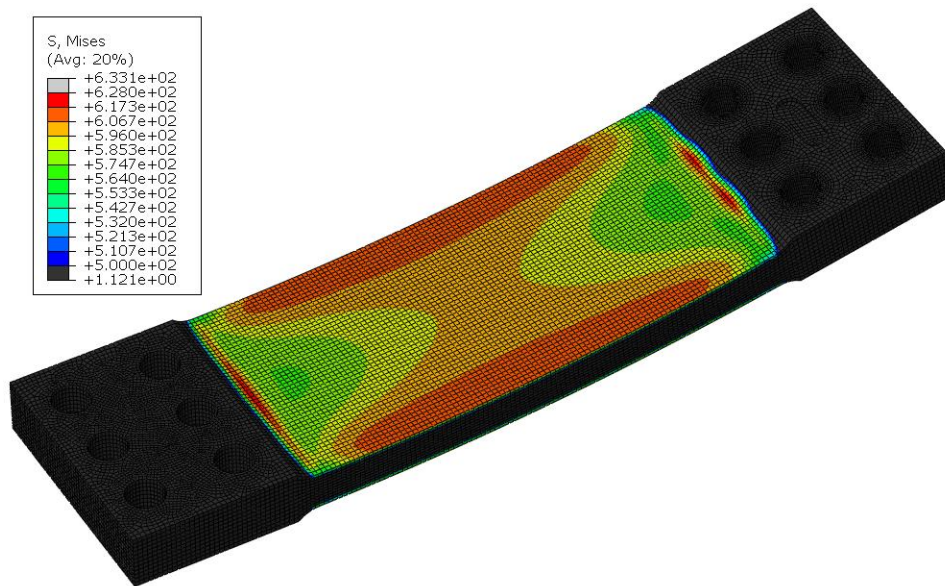


Figure 40: Bending Stress in Active Span of MKIII Spring

Finally, the input load angle was varied and results of the analytical model and FEA were compared. This was done by comparing the estimated deflection and stress between the two models. This comparison was only conducted on MKIII spring due the number of required FEA runs. The model with both bolted joints was utilized, as this is representative of the actual configuration that will be used on the exoskeleton. In total, 10 FEA runs were conducted in which the load input angle was varied $\pm 8^\circ$ by two-degree increments.

The comparison of deflection results can be seen in Figure 41. Examining the plot, it is apparent the models have relatively good agreement during positive loading. The two lines have almost the same slope but are offset from one another. The error between these two lines varies between 1.6% and 2.6%. However, this is not the case during negative loading. Here the two lines can be seen diverging from one another, resulting in an error that increases from 3.3% to 10.3%. The FEA predicted deflection actually exceeds both predicted values during positive loading. Once more, the bolted joint stiffness becomes is likely a critical factor.

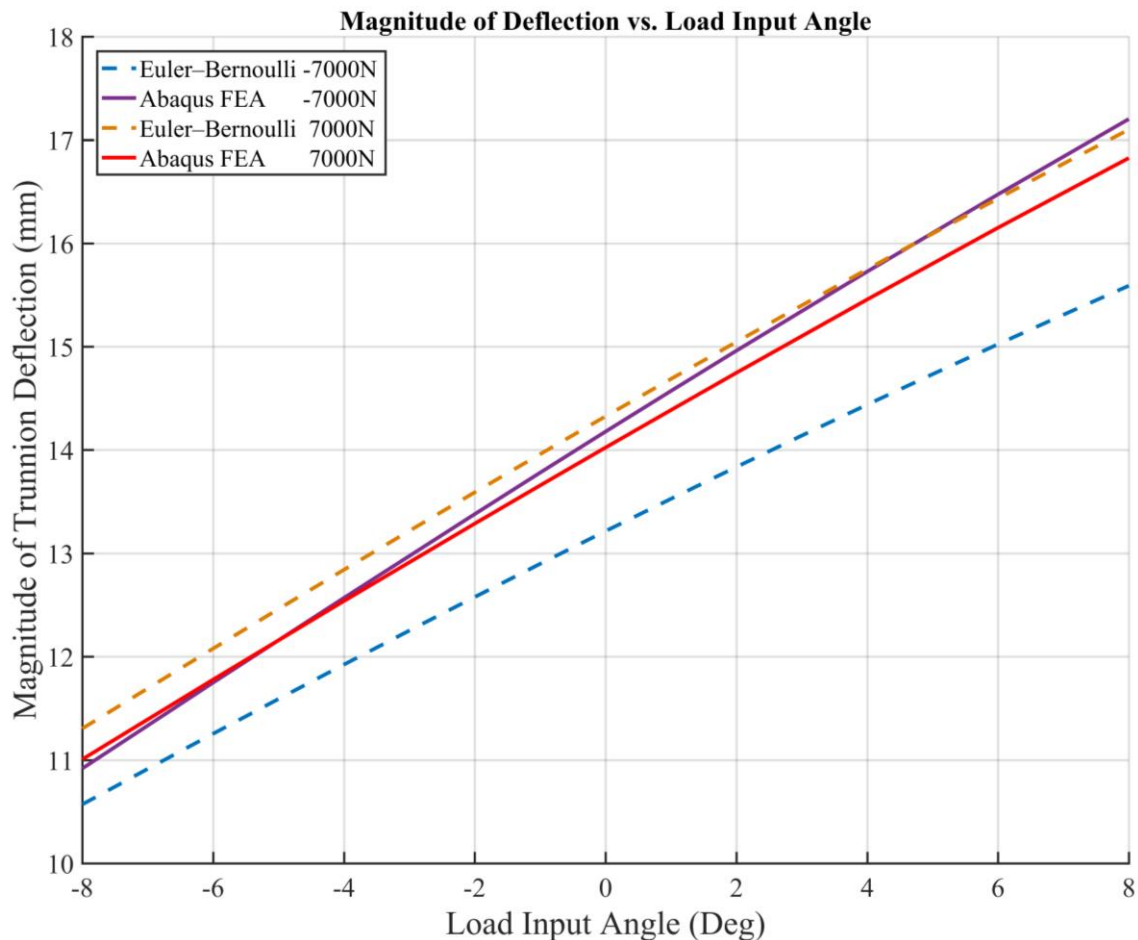


Figure 41: Model Comparison of Magnitude of Deflection versus Input Angle

Inspecting Figure 42, the effects of stress concentrations can be easily seen. Large deviations can be seen between the two models. However, once bending stress becomes the dominate value, the models have excellent agreement. The maximum error between the two models drops to less than 2% once this occurs.

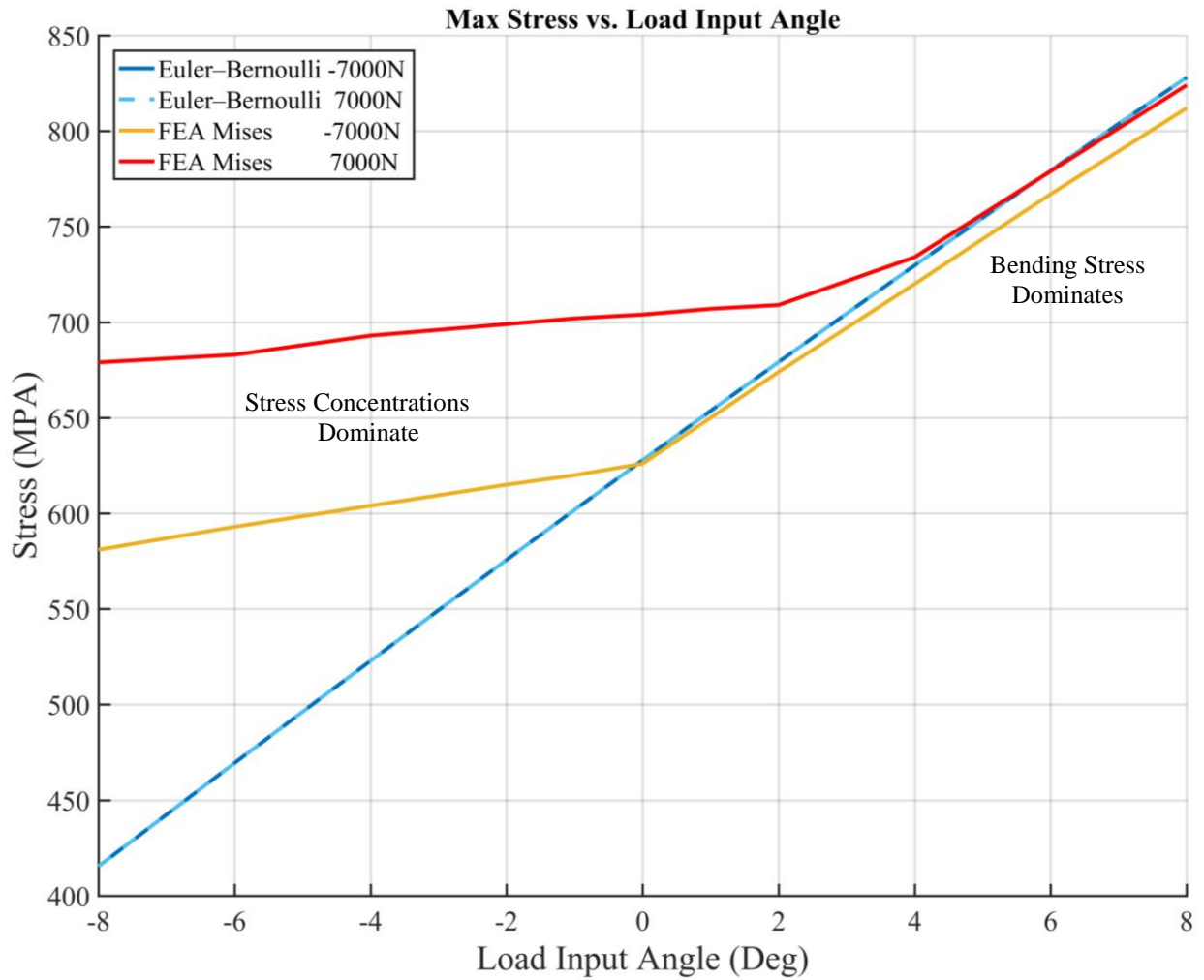


Figure 42: Model Comparison of Maximum Stress versus Input Angle

5. Linear Series Elastic Actuator Mechanical Design

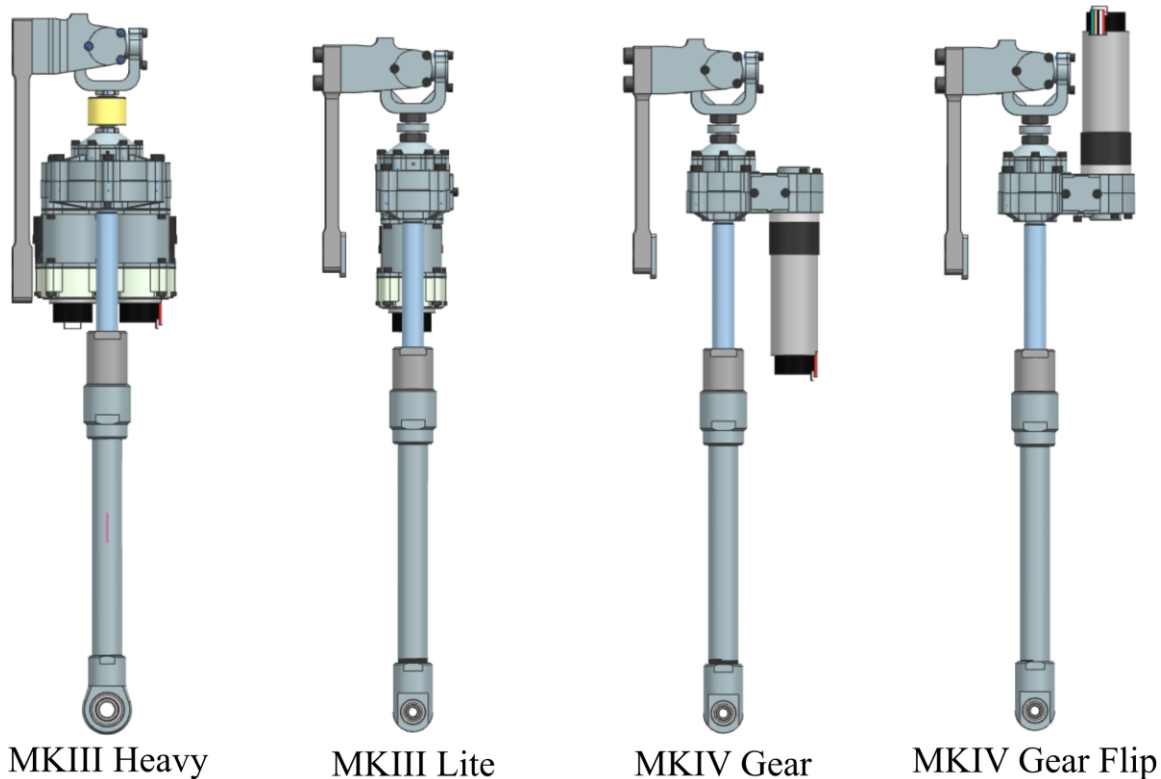


Figure 43: Overview of the Four LSEA's for the OLL-E Exoskeleton

Utilizing the selected major components and requirements developed in the previous chapters, the final step of detailed component design was initiated. As discussed in section 3.3, three different gear train configurations were necessary to meet all of the joint requirements. These three configurations, the MKIII Heavy, MKIII Lite, and MKIV Gear, are shown in Figure 43. However as can be seen, four different actuator configurations were developed. This was a result of the packaging requirements placed on the hip joints of the exoskeleton [96]. In order to meet these new requirements, a variation of the MKIV Gear was produced to permit better packaging. This actuator has the motor flipped 180° so that the motor is located over the U-Joint instead of the ball screw. This provides more clearance along the ball screw, and consolidates the bulk of the actuator in one location. This variation was given the designation MKIV Gear Flip.

While the performance of each LSEA varies greatly, the overall configuration of the four actuators is identical. Figure 44 and Figure 45 give a general overview of the major components found in MKIII Heavy and MKIV Gear. However, this component layout can be generalized across all four

actuators. A custom-machined ball screw from THK is located at the center of the actuator. The balls screw is attached to a timing pulley that is sandwiched between thrust bearings in the bearing housing. The Maxon EC-4 pole brushless motor is also mounted to this housing and is connected to the ball screw via a timing pulley. The bearing housing not only holds these components, but also transmits the thrust load from the ball screw through a Futek load cell to the U-joint yoke. The load cell is use to precisely measure the output force of the actuator during operation. The u-joint connects the actuator to the lever arm and titanium leaf spring. The u-joint also ensures the actuator is only loaded as a two-force member and reduces the chance of binding due to small misalignments.

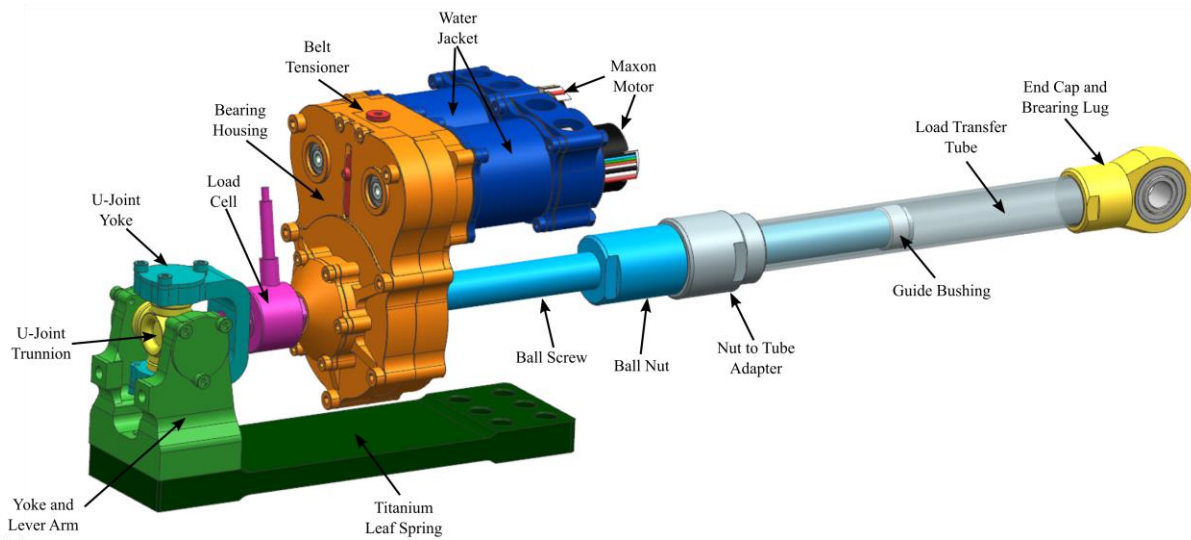


Figure 44: Component Overview of the MKIII Heavy LSEA

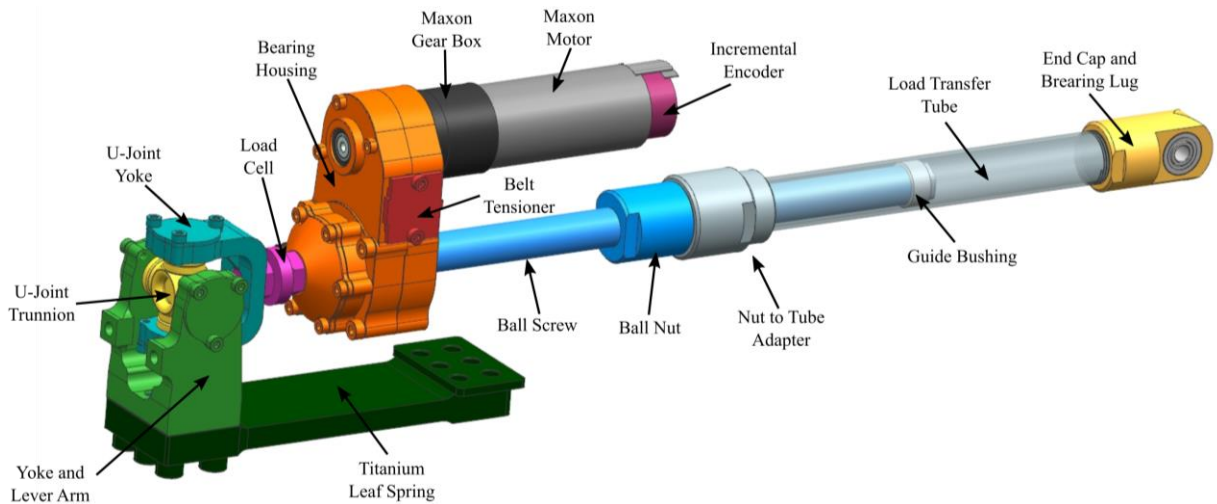


Figure 45: Component Overview of the MKIV Geared LSEA

In order to manipulate the joints of the exoskeleton, the force generated by the ball screw must be transferred from the ball nut to the joint lever arm. For joints with a low range of motion or tight packaging requirements, the ball nut can be directly connected to the joints lever arm. This configuration was used on THOR's knees [40] as well as the hip roll and yaw joints of OLL-E [96]. For all other joints, a load bearing tube was used to transmit the force to the lever arm. A bushing on the end of the ball screw rides along the inner wall of the tube. This bushing helps maintain axial alignment between the ball screw and load bearing tube.

These components can be grouped into four major subassemblies. The Actuator Bearing and Transmission Assembly contains the upper and lower housings, thrust bearings, axial bearings, timing pulleys, belt tensioner, and Maxon motor. The Cooling Jacket Assembly is comprised of the cooling jacket, water block, O-rings, gaskets, and fittings. The Load Bearing Tube Assembly contains the adapter nut, load bearing tube, and end cap. Finally, the Yoke and U-Joint Assembly consists of the titanium leaf spring, lever arm, trunnion, bearings, and yoke. These assemblies will be discussed in further detail later in this chapter.

Given the similarity of selected components, the overall configuration of the OLL-E's LSEAs resemble those found on THOR and ESHER. However, these new actuators can be viewed as the next generation of LSEA utilizing this configuration. A comparison of the actuators found on SAFFiR, THOR, and OLL-E is shown in Table 18. Utilizing liquid cooling, these new actuators have a power-to-weight and force-to-weight ratio superior to the previous generation. Not only do the new actuators have improved performance but they also possess greater configurability. The MKIII Lite and MKIV have customizable gear ratios that allow the output force and speed to be adjusted for a specific application.

Although the new actuators are heavier, their mass is easily justifiable given their significantly higher performance. This mass was the result of the larger ball screw, spring, and other components necessary to handle the increased force output. It should also be noted that the mass of the required cooling equipment is not included in the Full SEA Mass provided in Table 18. The presented mass can be viewed as the amount of mass the actuator will contribute to the inertia of the moving segments on the exoskeleton. An estimate of system power-to-weight and force-to-weight ratios were determined using a cooling system mass of 9kg supporting four MKIII Heavy and four MKIII Lite actuators. These values are highlighted by an asterisk (*) in Table 18.

Table 18: Comparison of Linear SEA's from SAFFiR, THOR, ESCHER, and OLL-E

SEA Characteristic	SAFFiR (MKI)	THOR (MKII)	MKIII Heavy	MKIII Lite	MKIV Gear
Liquid Cooling	No	No	Yes	Yes	No
# of Motors	1	1	2	1	1
Weight (Actuator) (kg)	0.653	0.726	1.73	1.27	1.27
Weight (Full SEA) (kg)	0.816	0.938	2.6	1.83	1.79
Continuous Power (W)	100	100	1600	800	200
Power/Weight (W/kg)	123	107	618 (372)*	438 (372)*	112
Maximum Speed (m/s)	0.35	0.198	0.267	0.767 - 0.444	0.16 - 0.093
Continuous Force (N)	300	685	7840	2090 - 2350	1420 - 2450
Peak Force (N)	1,000	2,225	8500	6300	6300
Force/Weight (N/kg)	1,225	2,372	3282 (2298)*	3452 (2298)*	3520
Spring Constant (kN/m)	145 - 512	372 or 655	500	500	500
Ball Screw Lead (mm)	3.175	2	4	4	4
Pulley reduction	2.5 : 1	3 : 1	4 : 1	1.39-2.4:1	6.68-11.52:1

With the major component of the actuator selected during the analysis process, the design effort could be focused on integration, custom component design, and selection for supporting hardware. This also allowed effort to be dedicated to addressing issues discovered in the previous generation of actuators. Several bearing in the universal joints experienced failures. These bearings were selected based on their dynamic load ratings. However, bearing subjected to continuous high load or intermittent peak loads while not rotating, like those in the u-joint, should be selected based on their static load rating. The static load rating is typically less than half the dynamic load rating. This is likely what led to the bearing failures in the previous generation. The old actuators also had a complex assembly process that required several iterations of test fitting and shimming. During this process, the actuator housing would be re-assembled several times with different shim combinations until the proper “feel” was obtained.

Stricter design requirements were placed on this new generation of actuators in an effort to correct these issues and further optimize the design. These requirements included increased mechanical safety factors, reducing the number of custom-machined parts, reduced complexity of assembly process, and increased number of interchangeable parts between actuators, while maintaining low weight and small package size. This chapter discusses the detail design of the four major actuator assemblies and the analyses used to refine and verify the design.

5.1. Bearing and Transmission Housing Assembly

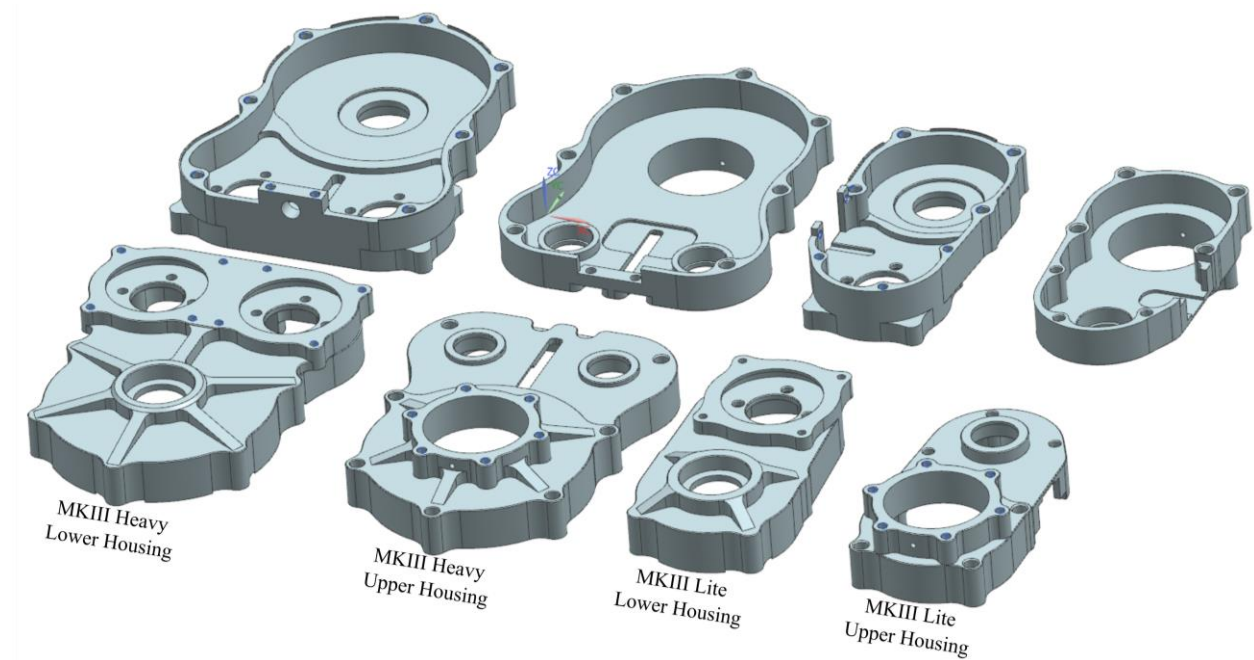


Figure 46: Upper and Lower Housings of the MKIII Heavy and MKIII Lite

The most critical and complex assembly of the LSEAs is the Actuator Bearing and Transmission Assembly. This assembly contains all of the components for mechanical power production and transmission in the actuator. However, the primary component of this assembly is the upper and lower actuator housings. Every component in the assembly is attached to or aligned by these two parts. This includes the bearings, ball screw, pulleys, belt tensioners, and motors. A top and bottom view of the MKIII upper and lower housings are shown in Figure 46. As can be seen in the figure, the housing is quite complex due to the number of components that must interface with them. In addition to positioning all of the components in the assembly, the housing also transfers the forces from the ball screw to the leaf spring.

In conjunction with the bearings, the housing must be capable of supporting and transmitting the forces generated by the ball screw. The cross-sectional view of Actuator Bearing and Transmission Housing Assembly in Figure 47 shows how compression and tension loads are transferred through the assembly. The compression load path is represented by a red line, while the tension load path is denoted by a yellow line. During compressive loading, forces are transferred from the ball screw to the timing pulley, then to the upper thrust bearing, through the thrust nut, into the upper housing, and finally into the Futek load cell through the load cell adapter plate. The tension load path is

slightly more complex due to the number of bolted joints the load is transferred through. Again, forces are transferred from the ball screw to the timing pulley, then to the lower thrust bearing, then into the lower housing, through bolts to the upper housing, through bolts again to the load cell adapter plate, and finally to the Futek load cell. This load path results in tensile loading being the critical load case for the upper and lower housing. Several analyses were conducted in order to ensure the actuator housings were capable of supporting the maximum tensile loads.

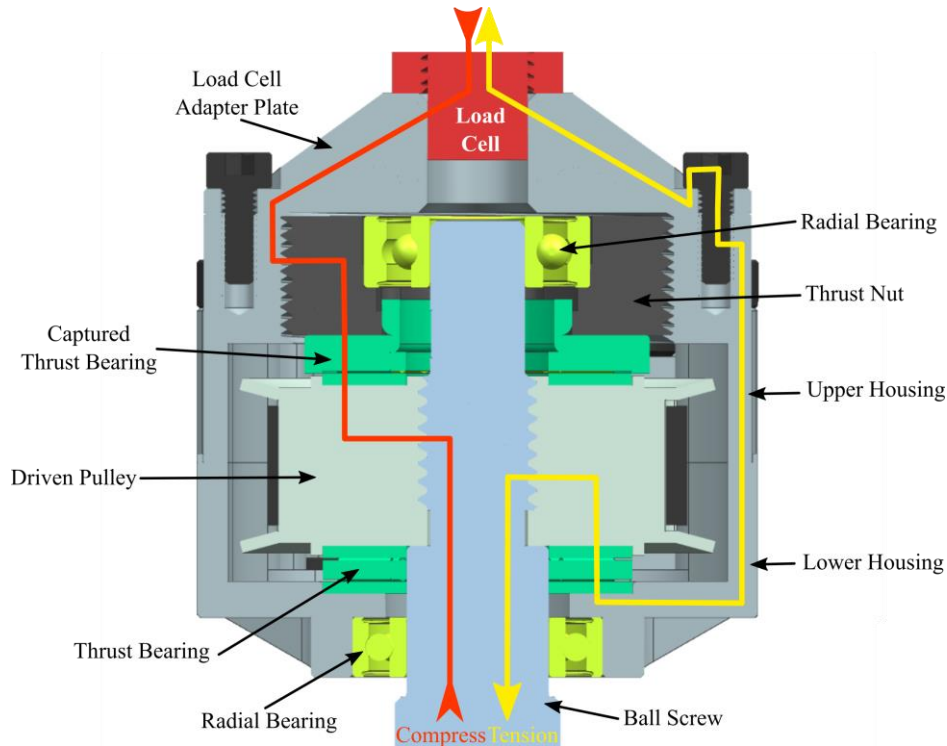


Figure 47: Cross-section View of Actuator Bearing and Transmission Assembly Showing Compression and Tension Load Paths

Through these analyses, the housing material was selected and several strengthening features were incorporated into the design. Aluminum alloy 7075-T6 was selected as the housing material due to its many desirable traits. With a yield strength almost as high as steel's, yet half its density, a strong, lightweight housing design was possible. Areas directly in the load path have thicker cross-sectional areas, while areas outside the load path were thinned in order to reduce weight. To further increase the strength and reduce deflection in the housing, ribs were added in several critical locations. These ribs are located around the lower thrust bearing, the center of the lower housing, and around round the thrust nut flange. Together these features help stiffen the housing while only adding a minimal amount of material.

5.1.1. Bearing Stack

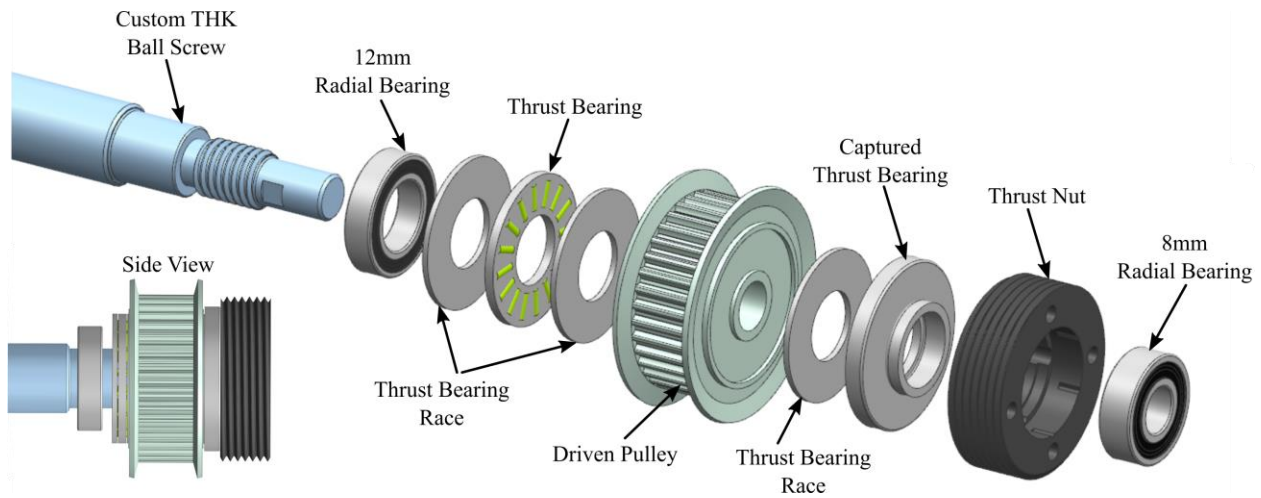


Figure 48: Ball Screw Bearing Stack Configuration

The bearing stack is a central subassembly of the Actuator Bearing and Transmission Assembly. The ball screw must be constrained both radially and axially in the housing. A typical ball bearing can only be loaded in the radial direction. However, there are several bearing types that are capable of simultaneously loading in both of these directions. These bearing types include angular contact bearings, spherical roller bearings, taper roller bearings, and combined needle roller bearings. It proved quite difficult to find angular contact bearings in a small package size that were also capable of handling the maximum load case. The other three bearing types were easily capable of handling very large loads, but again there were very few options available in the required size range. For these reasons, a combination individual thrust and radial bearings were used. This also allowed the size and load rating of each bearing to be selected independently. An overview of the bearing stack configuration with these two bearing types can be seen in Figure 48. A summary of the selected bearings and their load ratings can be found in Table 19.

Table 19: Bearings Used in all MKIII and MKIV Actuators

Bearing Type	Part #	Dimensions (mm)	Static Load Rating (N)	Dynamic Load Rating (N)
Deep Groove Radial	SKF 607/8-2Z	8x19x6	950	2340
Deep Groove Radial	SKF 61801-2Z	12x21x5	915	1740
Needle Roller Thrust	SFK AXW 12 AXK 1226	12x26x2	30000	9150

A key improvement in the bearing stack preloading and assembly process was made as well. The previous generations of actuators required shims to be placed under the bearing races to preload the thrust bearings. However, due to the variability during manufacturing of components, each actuator required a different set of shims. There was no method for determining which combination of shims was necessary. This resulted in having to reassemble the actuator several times until the right preload was obtained. The proper preload was done by “feel” and no measurement tools were used. Instead of shims, the thrust bearings in the new actuators are preloaded using a threaded plug christened the thrust nut. The thrust nut threads into the upper housing and “clamps down” on the thrust bearing. This can be done while the actuator housing is assembled. Using a custom made spanner wrench and torque wrench; the thrust nut is tightened and then torqued to the desired preload. This process can be seen in Figure 49.



Figure 49: Installation of Bearing Components (Left) and Thrust Nut (Right)

Not only does the thrust nut greatly improve the ease of installing and preloading the upper bearing, but several other critical design features have been implemented as well. As a result of the thread machining requirements for the timing pulley, the diameter of the ball screw shaft must be reduced to 8mm after the pulley. This does not allow the same size thrust bearing to be used on the upper bearing stack. The lower thrust bearing utilizes the 12mm diameter of the ball screw shaft to align itself in the bearing sack. In order for the same bearing to be used in the upper stack, it must be aligned over the 8mm shaft by some other method. This was achieved by using a special bearing race that captures and aligns the thrust bearing. Instead of using the ball screw shaft, this captured race is mounted into the bore of the thrust nut. The upper radial bearing is also installed into the thrust nut. Finally, this assembly is installed over the upper thrust bearing and screwed into place.

5.1.2. Overhung load analysis

A key consideration in determining the mounting configuration of the motors in the housing was the Overhung Load. Overhung Load (OHL) is the industry term for the radial loading experienced on the unsupported end of a motor output shaft. If the operational OHL exceeds the manufacture's rating, then additional bearing support must be added to the motor shaft and drive pulley. The OHL can be calculated using equation (5.1).

$$OHL = \frac{9550 * P * F}{N * PR} \quad (5.1)$$

Where P is the shaft power in kilowatts, F is the Load Connection Factor, N is the rpm of the shaft, and PR is the Pitch Radius. However, if the output torque of the motor is known, the equation simplifies to (5.2) with T representing the output torque of the motor.

$$OHL = \frac{T * F}{PR} \quad (5.2)$$

It should be noted that PR is the radius of the pulley plus the Pitch Line Difference (PLD). Unlike gear and chain drive systems, the PLD of a timing belt drive is outside the pulley. Therefore, the PLD should be added to the radius of the pulley to obtain the PR . The Load Connection Factor F corrects the load for the type of drive system being utilized. This correction factor can vary widely between belt, chain, and gear driven systems. The manufacture recommended correction factor for the specific belt should be utilized.

Once the OHL is calculated, it must be compared to the manufacture's shaft rating. However, the location of the load on the shaft must be considered. Manufactures typically provide their OHL ratings one shaft diameter away from the face of the motor, which is represented as d in Figure 50. This rating must be corrected to the actual input location D so the loads can be compared.

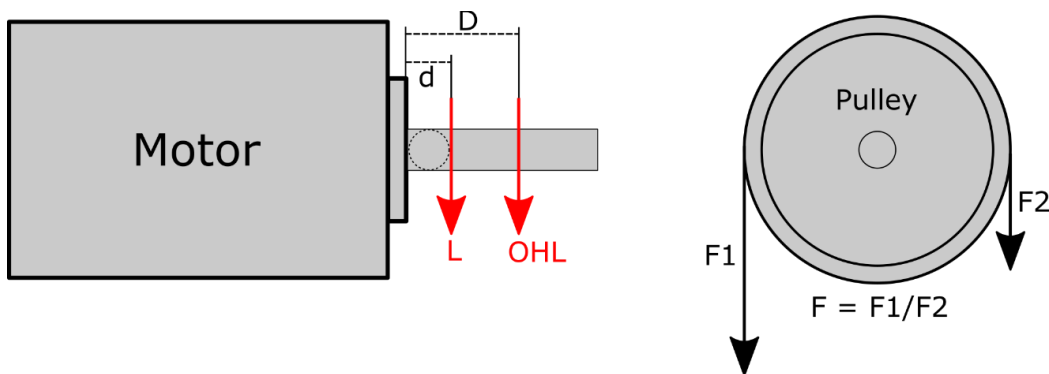


Figure 50: Free Body Diagrams of Overhung Load and Load Connection Factor

If no specific correction factor is provided, then this correction can be achieved using the Equivalent Moments method. The moment generated by the rated load L at the given distance (d) can be divided by the actual location D of the OHL. This is shown in equation (5.3).

$$L_{adjusted} = \frac{L * d}{D} \tag{5.3}$$

With the rated load adjusted, it can now be directly compared to the OHL. The maximum estimated output torques for the motor and gearbox were used to determine the worst case OHL. The results of the OHL calculations in Table 20 show that both the motor and gearbox are unable to support the loads. The factors of safety are both well below 1 and steps must be taken to remove or reduce the OHL.

Table 20: Overhung Load Results for Actuator Dive Components

Component	d (mm)	L (N)	D (mm)	L _{adj} (N)	OHL (N)	Factor of Safety
Maxon EC-4Pole	5	25	11.55	10.82	231.3	0.05
Maxon GP32	10	90	9.95	86.12	212.8	0.40

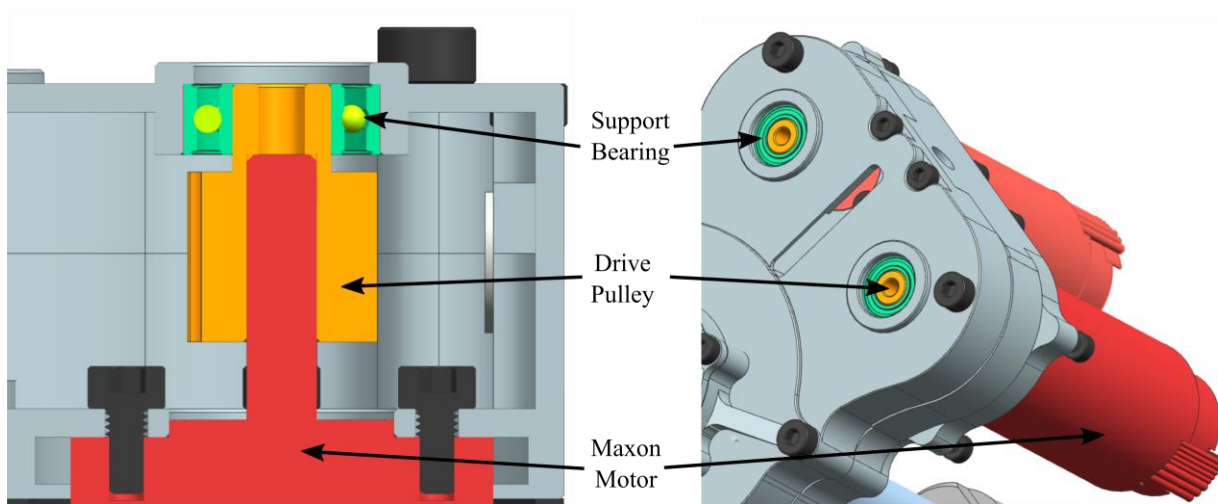


Figure 51: Integral Dual Support Design for Drive Pulley

In order to remedy this issue, a support bearing was integrated in to the upper housings of the actuators. This changed the load case from overhung to double supported, eliminating the large bending moment induced on the motor bearings. To save space and maintain low weight, bearing pockets were machined directly in to the upper housing. The bearings were then pressed into the

housing. However, the motor shaft was not long enough to reach this bearing. To bridge this gap, custom timing pulleys were designed with shaft extensions. This configuration can be seen in Figure 51. This custom drive pulley is pressed and shaft locked onto the motor shaft. A hole in the top of the pulley permits a 1/16” punch to be inserted into the pulley for disassembly. This allows force to be directly applied to the motor shaft without applying force to the motor bearings, eliminating the risk of potential damage to the motor’s bearings from prying the pulley from the shaft.

5.1.3. Belt Tensioning

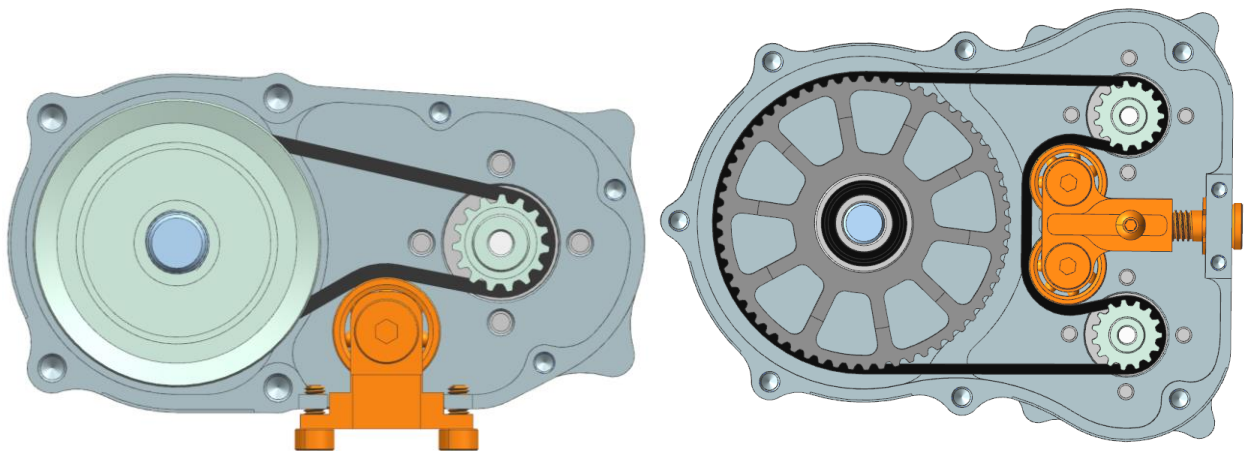


Figure 52: Belt Tensioner Designs for Single and Dual Motor Actuators

While the belt tensioning method used in the previous actuators [40] was innovative, it could not be used in this generation of actuators. This was due to the need of double support on the drive pulley and the incorporation of cooling jackets. For these reasons, a carriage style tensioner design was adopted instead. In this arrangement, an idler pulley is mounted to a small support carriage. This carriage is then slid towards the belt until the idler engages the belt and is locked into place. Due to the very limited sizes of OTS idler pulleys, ball bearings were used as pulleys instead. This allowed the exact desired pulley size too be utilized, thanks to the plethora of bearing sizes available on the market. With this method, the belt runs directly against the outer race of the bearing as seen in Figure 52.

To reduce the number of parts, the belt tensioners all use the same parts with the exception of the custom-machined tensioner carriage and adjustment screws. Viewing Figure 53, these shared components can be seen. These components include the bearing bolts, bearing spacers, and

bearings. The three single motor actuators all share the same single idler carriage, while the dual-motor actuators use a twin-idler carriage. The carriages slot into grooves machined into the upper and lower housings. These grooves guide the carriage into the belt and prevent any unwanted movement. The belts are tensioned via adjustment bolts that force the idlers against the belt. Due to space constraints, the single motor tensioner simply uses two M2.5 bolts to pull the carriage towards the housing. The dual motor tensioner uses a slightly more complex system for tensioning. A shoulder bolt is inserted through a hole in the lower housing and threaded into the carriage. An e-ring is then installed in the bolt between the housing and carriage. This e-ring captures the bolt and allows the bolt to be rotated, forcing the tensioner into the belt. Once the belt is tensioned, a locking bolt is tightened to prevent the carriage from moving.

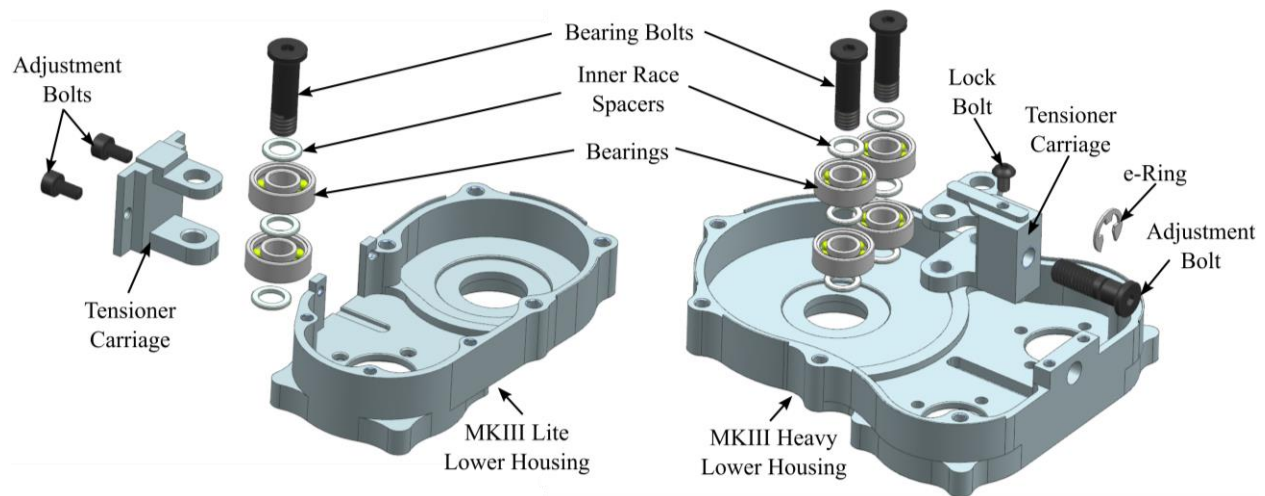


Figure 53: Belt Tensioner Components for Single Motor and Duel Motor Actuators

Like the previous belt tensioning system, the carriage system allows for easy adjustment while the actuator is fully assembled. The belt tension can also be easily adjusted while the actuator is mounted on the exoskeleton. This is an essential feature as timing belts tend to stretch over time and require readjustment. Another benefit of this design is it allows the actuator housing to fully enclose the moving components. This not only prevents dust and debris for getting into the bearing stack, but also improves operator safety. Exposed moving components are dangerous due to the actuators close proximity to the user. A fully enclosed actuator housing prevents a user's fingers or hair from getting caught in the timing belt and pulleys.

5.2. Cooling Jacket Assembly

The crucial subsystem allowing the enhanced performance of the motors is the Cooling Jacket Assembly. Without this liquid cooling system, the motors would quickly over heat and fail. While Maxon's cylindrical motor design lends itself to easily being retrofitted with a cooling jacket, several key design criteria were taken into consideration. First and foremost, the water jacket must remain watertight during operation of the exoskeleton, as leaks could damage high-power electronics and create a shock hazard to the operator. Second, the cooling jacket must be capable of being easily removed or installed while the actuator is mounted on the exoskeleton, so maintenance can be performed on the actuator without having to remove it from the exoskeleton. This also allows the actuators to be used in other applications where liquid cooling is not required. Lastly, the cooling jacket should be designed so that it can be machined or 3-D printed. This permits for a wide range of material options and expedites the prototyping process, allowing different jacket designs to be easily produced for performance testing. The cooling jackets also utilize standard aftermarket computer liquid cooling fittings and plumbing methods. This ensures components in the cooling system can easily be replaced or upgraded in the future. This was done in effort to allow the cooling system to be easily modified as the design of the actuators and exoskeleton evolve.

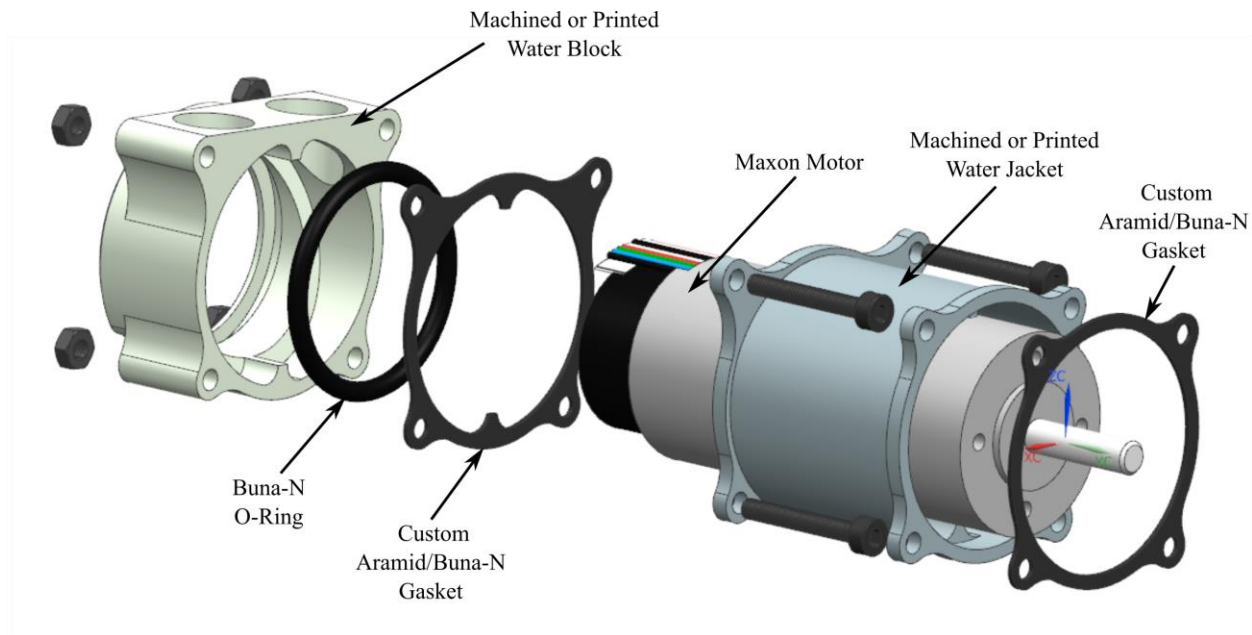


Figure 54: Cooling Jacket Component Overview

Using these requirements, the cooling jacket design seen in Figure 54 was developed. The cooling jacket consist of two major components, the water block and the jacket. The water block is mounted at the rear of the motor near the encoder. This locates the water block over the section of the motor that contains the internal circuitry and Hall effect sensor that are not heat generating components. This allows the jacket to be mounted over the full length of the windings in the motor. The water block also contains the inlet and outlet holes for the fluid. These holes are threaded in 1/4" G: Series British Standard Pipe - Parallel (BSPP), which is a standard threading used by most computer cooling systems. Compression fittings are screwed into these holes allowing coolant to be routed around the exoskeleton using flexible 1/4" PVC (polyvinyl chloride) tubing. An O-ring is also housed in the water block, which seals the cooling system around the motor. The jacket contains fins that direct the flow of water around the surface of the motor and is sealed to the water block with a gasket. Another gasket at the front of the jacket seals the assembly to the mount on the actuator lower housing.

To maintain the smallest package size as possible, several cooling jacket features were directly incorporated into the lower housing of the actuators. This reduced the number of parts and the overall size of the cooling jacket assembly. These integral features are shown in Figure 55. The front O-ring is installed directly into a machined groove in the housing. The motor is then installed through the O-ring and bolted into place. The actuator can then be left in this configuring if liquid cooling is not required. If cooling is required, the Cooling Jacket Assembly is simply slid over the back of the motor and secured in place with four bolts.

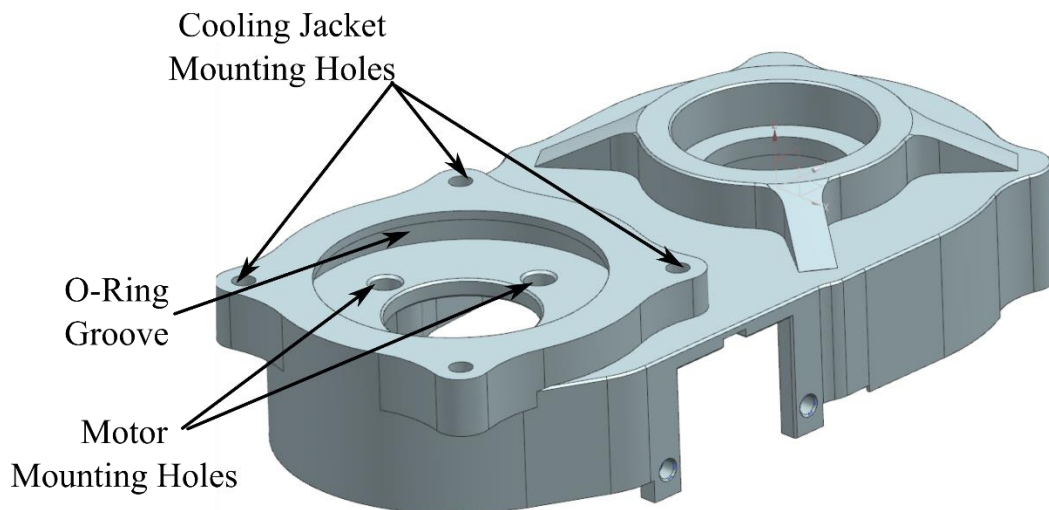


Figure 55: Cooling Jacket Mount and Seal Integration into Housing

5.2.1. Jacket Design

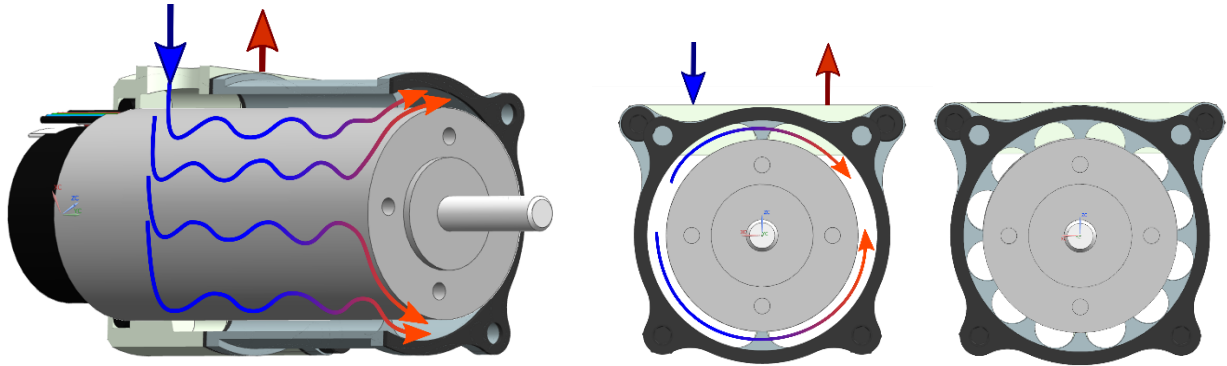


Figure 56: Cooling Jacket Flow Path (Left), Open Design (Center), and Fin Design (Right)

The jacket is used to direct the flow of water around the surface of the motor. Currently two different jacket design have been developed, however the design of the Cooling Jacket Assembly easily allows future jacket designs to be installed and tested. The first design is a basic concentric annulus with two fins dividing the flow area in half. However, the fins do not span the full length of the jacket. The resulting gap creates a water passage at the front of the motor that connects the two sides. This results in the inlet water flowing over 50% of the motors surface before passing through the water passages and returning across the other half of the motors surface. This flow path is illustrated in Figure 56. This jacket can be machined from aluminum, Delrin® or 3-D printed form a high temperature material, such as Polyamide Nylon.

The second jacket design has the same flow path as the first design but incorporated 12 cooling fins. These fins cover approximately 10% of the surface area of the motor and can be seen in Figure 57. These fins could potentially act like a heat sink and improve the cooling performance of the system. This jacket was machined form 6061-T6 aluminum, which has a thermal conductivity over 350x greater than water. This allows heat to be rapidly pulled out of the motor and into the jacket where it can then be dissipated. However, despite aluminum's high thermal conductivity the interface conductance between the housing and the fins can greatly affect the performance of the fins. The interface conductance is a function of the surface roughness and contact pressure between the fins and motor [102]. A transition fit was used during the machining process to improve the contact pressure of the fins; however, the jacket had to be heated in order for it to be easily install over the motor. Thermal testing must be conducted to determine if these fins and contact conductance improve or degrade the overall performance of the cooling systems

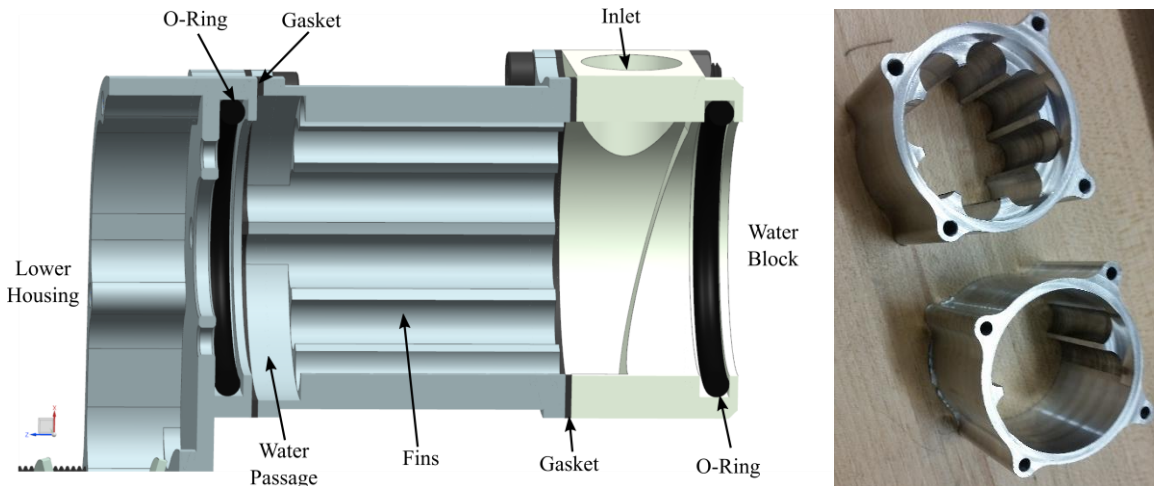


Figure 57: Cross-Section of Fined Cooling Jacket and Lower Housing

While these two jacket design were selected for the preliminary testing process, other jacket designs can be explored. Altering the flow path and the amount of time the fluids spends passing over the surface of the motor can greatly affect the performance of the cooling system. Several other jacket designs could be implemented using this configuration. One such design would have the flow zigzag around the surface of the motor. This zig-zag flow design could be implement using a fin design similar to those seen in [73], [76]. More complex flow paths, such as inducing swirl around the motor, are also possible with 3-D printed jackets.

5.2.2. O-ring and Gasket Design

To form a watertight seal around the Maxon motor, a Buna-N O-ring was utilized. These O-rings are installed into glands (grooves) machined into the water block and lower housing. In order to ensure a watertight seal was attained, several design factors were considered during the design of the gland. A general design guideline for static seals is to maintain a 10%-40% compression of the O-ring [101]. This percent compression is directly related to the crush distance of the O-ring, which is set by the gland diameter. Along with the gland diameter, the gland width is another critical design factor. The gland width determines the cross sectional area of the gland. The cross sectional area of the O-ring should not exceed 90% of the gland cross sectional area to allow room for the O-ring to deform. If the gland width is too small, the O-ring will fill the gland and not allow the motor to be installed or lead to a damaged O-ring. Using the design criteria and the dimensions of the Maxon motor, the percent compression and gland width were determined.

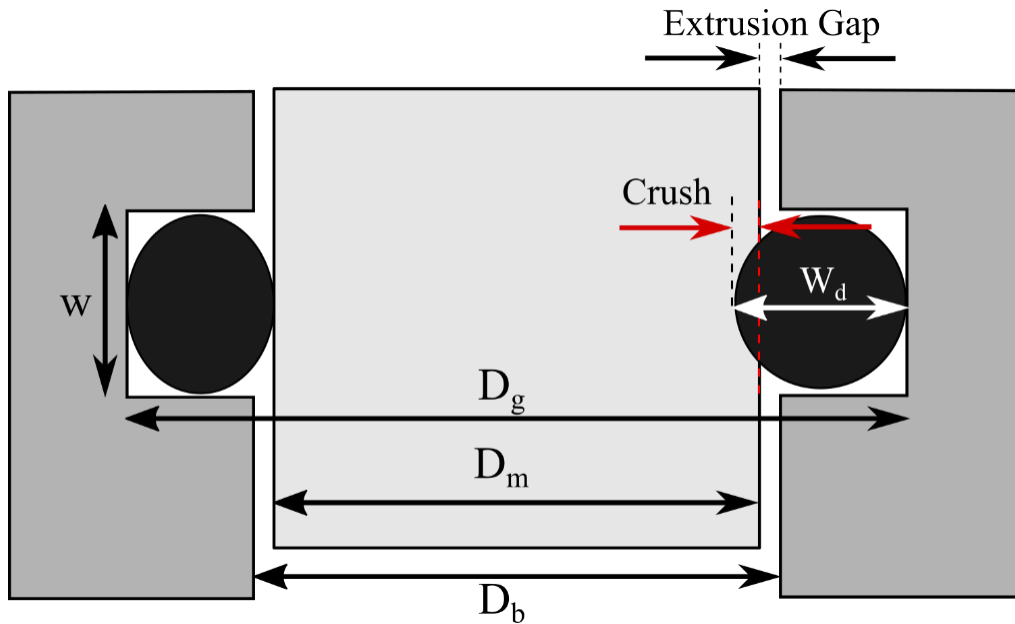


Figure 58: O-Ring Calculation Diagram

Several critical dimensions determine the compression of the O-ring. These dimensions include the diameter on the motor D_m , the bore diameter D_b , and width of the O-ring W_d . Figure 58 shows cooling jacket O-ring configuration and relevant dimensions. However, these dimensions can vary due to deviations in the manufacturing process; therefore, the manufacturing tolerances were included in the following calculations. This ensures the O-ring will properly seal even with deviation in crush due to tolerance stack up. These tolerances are based on information from Maxon and experience of the accuracy generally obtained on the labs computer numerical control (CNC) milling machines. These dimension and their manufacturing tolerances are summarized in Table 21. The O-ring width W_d was selected to be 3mm, this O-ring size is readily available and a gland of this size or larger could be easily machined with a T-slot cutter on the CNC mill.

Table 21: O-ring Calculation Dimensions and Tolerances

Dimension	Nominal	+ Tolerance	- Tolerance
Gland Diameter D_g (mm)	35	0.05	0.05
Bore Diameter D_b (mm)	30.1	0.05	0.05
Motor Diameter D_m (mm)	29.85	0.15	0.1
O-Ring Width W_d (mm)	3		

Using these dimensions, the minimum, nominal, and maximum crush were calculated using equation (5.4). This was done by combining tolerances that would produce the largest and smallest gap between the motor and gland. The crush is then determined using equation (5.5) to calculate the percent compression of the O-ring.

$$Crush = W_d - \frac{D_g - D_m}{2} \quad (5.4)$$

$$\%Comp. = \left| \frac{(W_d - Crush) - W_d}{W_d} \right| \times 100 \quad (5.5)$$

Finally, the minimum width of the gland was calculated using equation (5.6). The ratio between the cross sectional area was set so that the O-ring would fill no more than 85% of the gland.

$$\text{Min. Gland Width} = \frac{\pi W_d^2}{4} \times \frac{2}{D_{gmin} - D_{bmax}} \times \frac{1}{0.85} \quad (5.6)$$

The results of these calculations are summarized in Table 22. It can be seen that the percent compression ranges from 12% to 18%, which is acceptable for low-pressure applications like the cooling jacket. The minimum required gland width was determined to be 3.4mm, which was increased to 3.5mm to ease the machining process. To prevent the O-ring from free floating in the gland, a slightly oversize O-ring was chosen. A standard Buna-N 3x30 with a soft Durometer of 50A was selected. This O-ring has an outside diameter of 36mm, which is 1mm larger than the selected gland diameter of 35mm. This results in a 2% squeeze between the O-ring and gland, holding the O-ring in place during the installation of the jacket over the motor.

Table 22: O-Ring Calculation Results

Results	Minimum	Nominal	Maximum
Crush (mm)	0.35	0.42	0.53
% Compression	11.7	14.2	17.7
Extrusion Gap (mm)	0.03	0.13	0.20
Min. Gland Width (mm)	3.40		

5.3. Load Bearing Tube Assembly

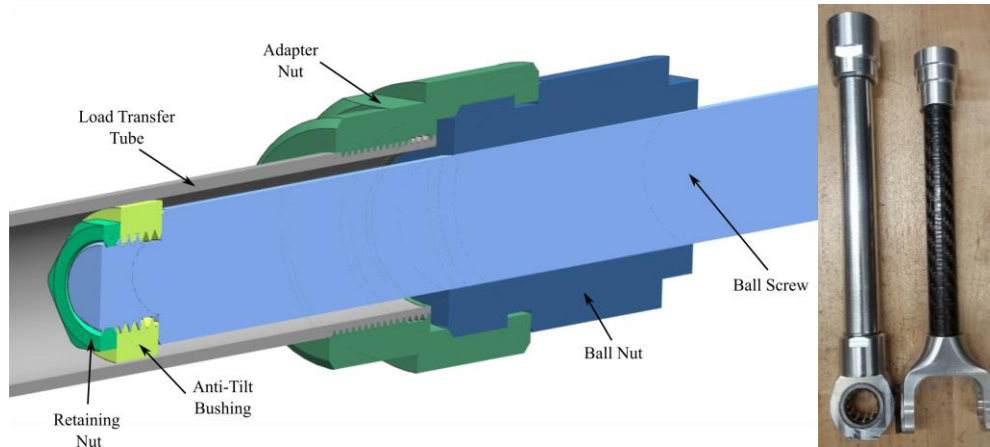


Figure 59: Cross Section Load Bearing Tube (Left) Comparison to Prior Design (Right)

For joints that cannot connect directly to the ball nut, a load bearing tube was used to transmit the force to the lever arm. This load bearing tube is attached to the ball screw via a custom adapter nut. A bushing is threaded on the end of the ball screw and retained by a jam nut. This bushing rides along the inner wall of the tube and helps maintain axial alignment of the ball screw and load bearing tube. This is the same configuration used on THOR and ESCHER [40], however, several changes were made.

The previous tubes were made from carbon fiber, which is expensive, difficult to work with, and posed an inhalation hazard while cutting. The carbon fiber tube also required the components to be permanently attached to the tube with epoxy resin. Carbon fiber composites only have a density of approximately 1 g/cm^3 lower than the density of aluminum. This minimal weight saving did not justify the added cost, complexity, and risk of carbon fiber. The new load bearing tube was instead made from 3/4" 6061-T6 aluminum tubing. The ends of the tube were threaded so that the adapter nut and end cap could be easily assembled or disassembled. Another change was the simplification of the anti-tilt bushing. The previous design mounted a Teflon™ bushing on bearings that allowed it to freely rotate as it slid up and down the tube. However, this configuration was prone to bearing failures and falling off. The bearings and free rotation were not seen as a necessary feature and the design was simplified with their removal. Instead, the bushing is mounted directly onto the end of the ball screw and is secured in place with LOCTITE® and a jam nut. With the bushing secured to the end of the ball screw, the aluminum tube was lubricated with grease to further reduce friction.

5.4. U-Joint and Yoke Assembly

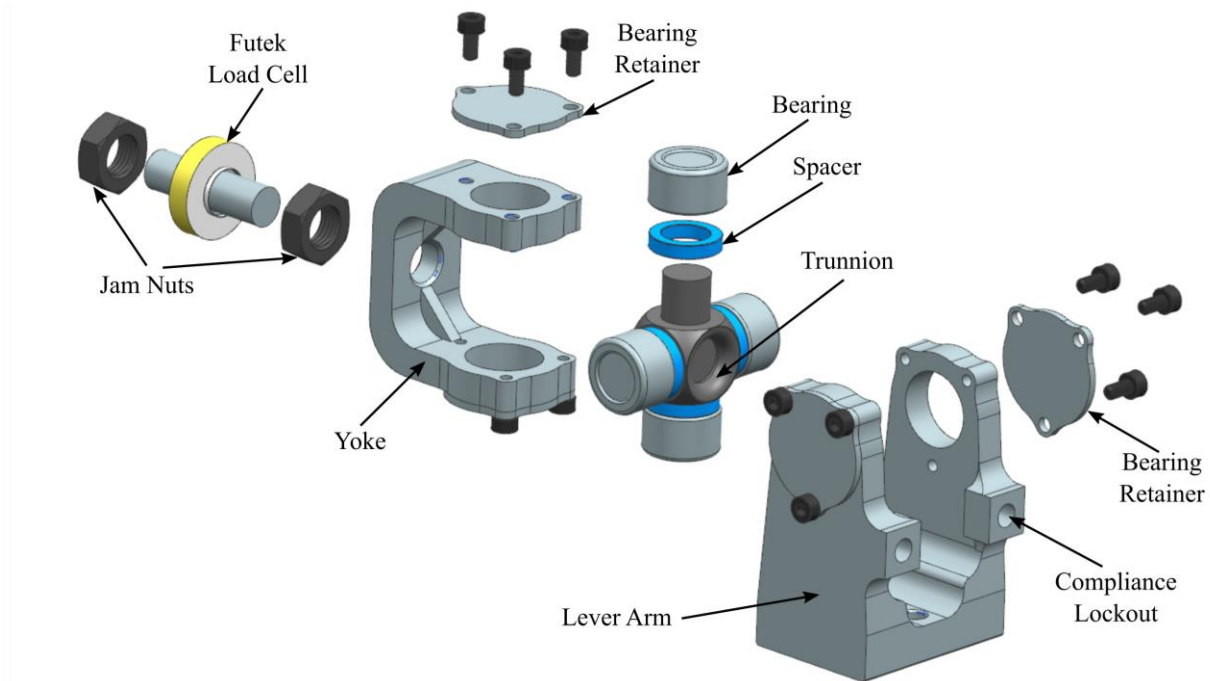


Figure 60: U-Joint and Yoke Assembly

To connect the actuator to the leaf spring lever and ensure two-force member loading, a universal joint was utilized. The u-joint permits two degrees of freedom in the horizontal and vertical directions, but restricts rotation along the axis of the of the ball screw. This prevents off-axis loading that could induce buckling as well as reducing the chance of binding due to small misalignments. The u-joint also allows the actuator to be utilized in dual actuation configurations, where two degrees of freedom are required. Examining Figure 60, the u-joint is shown installed between the yoke and lever arm. Spacers were placed between the u-joint trunnion and bearings to prevent any lateral movement of the trunnion once installed. The u-joint trunnion is placed in the middle of the yokes and the bearing are pressed into place. Retaining plates are then bolted over the bearing to ensure the bearings do not move.

Several other key feature were incorporated into the U-Joint and Yoke Assembly. A Futek LCM 200 or LCM 325 load cell is placed between the yoke and actuator housing. This load cell allows direct measurement of the actuator output force during operation, which is crucial for force control systems. Another feature was the incorporation of a compliance lock-out on the lever arm. When installed, this lock-out prevents the deflection of the spring, allowing the use of position control.

5.5. Fastener Analysis

Fasteners are essential components used throughout the actuators to constrain components together and transfer loads between them. A comprehensive understanding of the interactions between the bolts and the components they constraint is crucial. An inadequate number of bolts, improper preloading, and poor joint stiffness are just a few oversights that can lead to component failure. Some of the effects of bolted joint stiffness were seen in the results of the FEA analyses discussed in section 4.6. For these reasons, further analysis was conducted on the critical bolted joints of the actuator. This included the upper to lower housing bolts, load cell adapter plate bolts, lever arm to spring bolts, spring to base bolts, and the threaded load bearing tube.

As loads are transferred between components, the resulting stresses concentrate around the threads and head of the bolt. Although each component in the bolted joint stack is important, analyses can be focused on components most likely to suffer a failure. While all of the fasteners are made from steel, most of the actuator components are made from aluminum, making them the weakest link in the bolted joint. These steel bolts are threaded directly into the aluminum components, which have a lower yield strength than steel. Subsequently, the internal threads of the aluminum parts will suffer a failure long before the bolt does. This also means that the general conventions used to determine the number of required bolts and necessary preload cannot be used, as they assume the screw and nut have similar yield strengths.

To ensure thread failure would not occur in the aluminum, several design criteria were examined. As the bolt is threaded into the part, an initial clamping force is induced on the parts. This clamping force is called preload and directly related to the torque applied to the bolt. This preload ensures the parts remain in contact with one another as load is applied across the joint. Once the applied load becomes large enough to overcome the preload, the joint will separate. If separation occurs, the parts can now move independent of each other and the bolted joint is considered failed. Another criterion examined was the pull-out safety. Pull-out occurs when the shear yield strength of the threads is exceeded and the bolt rips the thread out of the hole. This was considered the most likely failure mode, as aluminum shear yield strength can be as little as half of that of steel's. Finally, bearing failure can occur on the aluminum's parts under the bolt head. This occurs when the force applied by the bolt head exceeds the compressive yield strength of the material beneath. In order to analyze these failure criteria [88], [102], [103] were utilized.

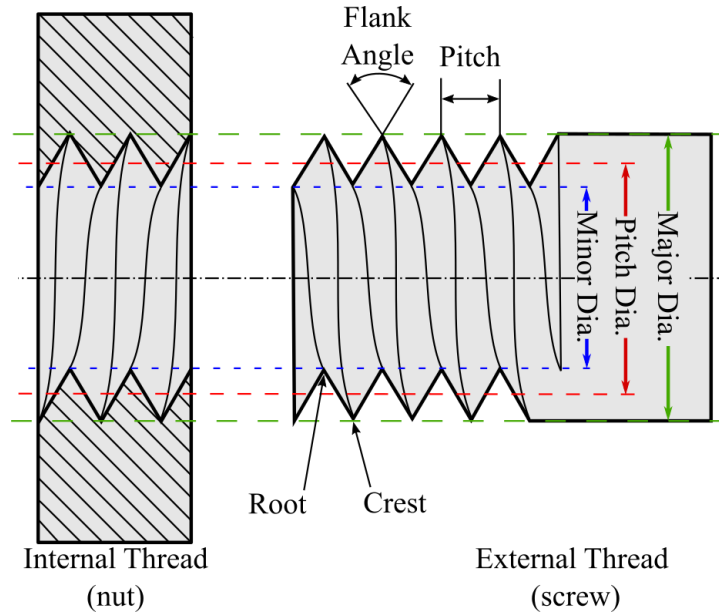


Figure 61: Characteristic Dimension of Metric Thread

Note that the following calculations only apply to International Organization for Standardization (ISO) metric screw threads. Two critical thread dimensions are necessary to perform the following calculations. These dimensions are the bolt major diameter d_{maj} , and the thread pitch P . Using these two dimensions the tensile stress area of a bolt can be calculated using:

$$A_t = \frac{\pi}{4} (d_{maj} - 0.9382P)^2 \quad (5.7)$$

Bolt preload is regularly specified as a percentage of the tensile yield strength of the bolt material. For most applications where the fastener will be reused, is approximately 64% [88]. However, the tensile yield strength of aluminum can be much lower than steels. As a result, this percentage will likely have to be reduced to prevent thread failure. Using the percentage of bolt yield Pr_{yld} , the bolt tensile yield strength S_{ty} , and tensile stress area A_t , the preload force F_{PL} can be calculated using:

$$F_{PL} = Pr_{yld} \cdot S_{ty} A_t \quad (5.8)$$

When a tensile load is applied to the joint, a percentage of the applied load is carried by the bolt while rest of the applied load acts to relieve the preload. This percentage is directly related to the relative stiffness of the bolt and the compressed members in the bolted joint. This relative stiffness, known as the joint constant C , can be calculated using equation (5.9). When no joint separation is occurring, the total tensile force on a bolt F_{bt} is equal to the sum of the preload F_{PL} and the applied tensile load $F_{t,app}$ multiplied by this joint constant C . This can be seen in equation (5.10).

$$C = \frac{k_{bolt}}{k_{bolt} + k_{member}} \quad (5.9)$$

$$F_{bt} = \begin{cases} F_{PL} + C \cdot F_{t.app} & \text{No Joint Separation} \\ F_{t.app} & \text{Joint Separation} \end{cases} \quad (5.10)$$

While the bolt stiffness k_{bolt} is relatively easy to determine, the stiffness of the members k_{member} is quite difficult to obtain. This is because the stiffness is a function of the compression region, which does not have a uniform area [88]. This area can be approximated using a frustum, however this assumes there is sufficient material around the bolt to allow a frustum to develop. If the approximation criterion cannot be met, then a conservative assumption can be applied to C . A very conservative assumption is to set $C=1$. This results in 100% of the applied load contributing to the bolt tensile load. While this will likely result in increasing the number and/or size of bolts necessary to achieve reasonable safety factors, it considerably reduces the design effort. Further discussion on joint member stiffness can be found in [88].

Using the Federal Standard, the thread shear area for an internal thread $A_{ts.int}$ can be calculated using equation (5.11). The length of threads that transfers the load from the bolt to the component is known as the length of engagement LE . This length is equal to the length of the internal threads the bolt engages or the bolt's major diameter $d_{maj.}$, whichever value is smaller [103]. The pitch diameter d_p can be calculated using equation (5.12).

$$A_{ts.int} = \frac{3}{4}\pi d_p LE \quad (5.11)$$

$$d_p = d_{maj.} - 0.64951905P \quad (5.12)$$

The shear stress in the internal threads $\tau_{ts.int}$ can then be calculated using:

$$\tau_{ts.int} = \frac{F_{bt}}{A_{ts.int}} \quad (5.13)$$

The factor of safety of using the internal thread shear yield strength S_{sy} is calculated by:

$$FS = \frac{S_{sy}}{\tau_{ts.int}} \quad (5.14)$$

Installation torque necessary to achieve the desired preload in the bolt is calculated using:

$$T = K_t F_{PL} d_{maj.} \quad (5.15)$$

Here, K_t is the coefficient of friction between the internal and external threads. This coefficient varies depending on the surface finish and accuracy of the bolt, as well as any applied lubricants. Torque coefficient based on the condition of the bolt can be found in table Table 23.

Table 23: Torque Factors K_t [88]

Bolt Condition	K_t
Nonplated or Black Oxide	0.30
Zinc-plated	0.20
Lubricated	0.18
Anti-Seize	0.12

The bearing area under the bolt head A_{bear} can be found using equation (5.16). Here, d_o is the bolt head outer diameter and d_h is the through-hole diameter.

$$A_{bear} = \frac{\pi}{4} (d_o^2 - d_h^2) \quad (5.16)$$

The stress in the bearing material can be found using the total tensile force on a bolt F_{bt} and the bearing area

$$\sigma_{bear} = \frac{F_{bt}}{A_{bear}} \quad (5.17)$$

Finally, bearing material safety factor can be calculated using the tensile yield stress of the bearing material S_{by} .

$$FS_{bear} = \frac{S_{by}}{\sigma_{bear}} \quad (5.18)$$

This section gives a general overview of bolted joint analysis methods, for further detail and insight of application specific assumptions; the cited sources should be reviewed. These calculations can be rigorous and time consuming, especially on systems with numerous bolted joints. For this reason the subscription based bolted joint analysis software from MechaniCalc [103] was utilized for most of the exoskeleton and actuator development. However, a keen understanding of how the result are produced is necessary, given the assumptions used to produce the joint consent C .

6. Conclusion

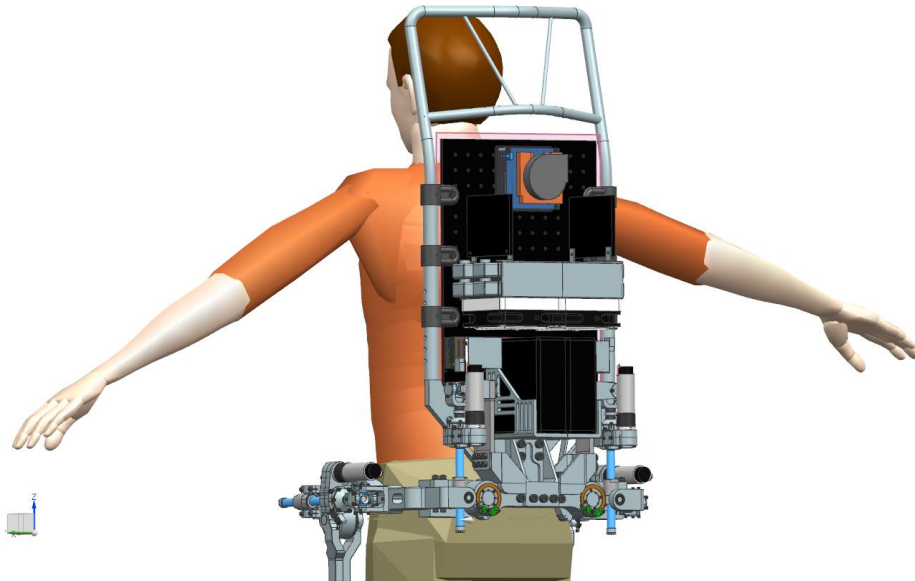


Figure 62: OLL-E Hip Joints Incorporating MKIV LSEA's and Hardware Backpack

In order to develop actuators of the fully self-balancing exoskeleton OLL-E, an analytical and requirements driven design approach was undertaken. These requirements were developed by examining the human gait and humanoid bipedal walking. Using these requirements, many different actuator configurations and components were examined. Reviewing the trade-offs between the potential configurations, a linear series elastic actuator that utilizes a ball screw was selected as the final configuration. An analytical model was then used to select all of the necessary gear-train components and predict the performance of the actuator. Using the selected components from these analyses, four different LSEA's were designed to meet the various joint power requirements. This included a dual-motor liquid-cooled actuator capable of producing a peak force of 8500N with a maximum travel speed of 0.267m/s, a single-motor liquid-cooled actuator capable of producing up to 2350N of force continuously with a maximum travel speed of 0.767m/s, and two different variations of a single motor actuator incorporating a planetary gear box to produce up to 2450N of force continuously with a maximum travel speed of 0.16m/s. This performance would not be possible without the centralized cooling system incorporated into to the OLL-E. With an on-limb mass of 2.6kg to 1.8kg, these actuators have a superior power-to-weight and force-to-weight ratios when compared to the previous generations of LSEA's developed at Virginia Tech. The MKIV Gear Flip actuator has already been implement in the 3-DoF hip joints [96] of the OLL-E, which can be seen Figure 62

6.1. Recommendations

During component fitment checks, it was discovered that the lower and upper radial bearings of the bearing stack did not fit on the ball screw. While the upper bearing was a tight transition fit that could still be assembled by hand, the lower bearing would not install. The witness marks seen on the shaft in Figure 63 suggest an interference fit. The simplest and most cost-effective solution to this issue was to hone the inner race of the bearing to increase the tolerance. This was achieved using a 12mm 240grit Flex-Hone® from Brush Research Manufacturing Co., Inc. A custom laser-cut jig was used to hold the inner race and protect the bearing from honing particulates. While this method was successful, it is not a recommend as a standard practice. If done improperly, microscopic metal particles can inundate the bearing and ruin it. This issue should be brought to THK attention so future ball screw orders can have the shaft tolerance adjusted accordingly. A tight transition fit would maintain axial alignment while allowing the bearing to be hand assembled.



Figure 63: Ball Screw Lower Bearing Fitment Issues (Left) Honing of Inner Race (Right)

With the first MKIII Lite prototyped mounted on the test stand, another potential issue was discovered. Between 0.2mm to 0.5mm (0.010” to 0.020”) of play was measured in the U-Joint trunnion and bearing assembly. This play was measured with a dial indicator against the yoke, as shown in Figure 64. The u-joint trunnion and bearing assembly is a \$5 OTS automotive steering column component produce by [104]. This appears to be the standard tolerance of the bearings after measuring the play of several u-joint assemblies. While this amount of play is acceptable for automotive applications, the sensitive control systems of the exoskeleton will detect and have to

reject this play. To reduce or remove this play, the u-joint trunnion and bearings will have to be replaced. This can be done by finding another OTS u-joint with higher tolerances or custom matching the components, as was done on THOR and ESCHER. If the components are to be custom machined, several design options are available that would otherwise not be possible with OTS components. Several actuators on THOR and ESCHER integrated the load cell directly into the u-joint [40]. This has the advantage of reducing the overall length of the actuator. An example of this u-joint configuration can be seen in Figure 65.



Figure 64: Significant Play Found In U-Joint Trunnion and Bearing

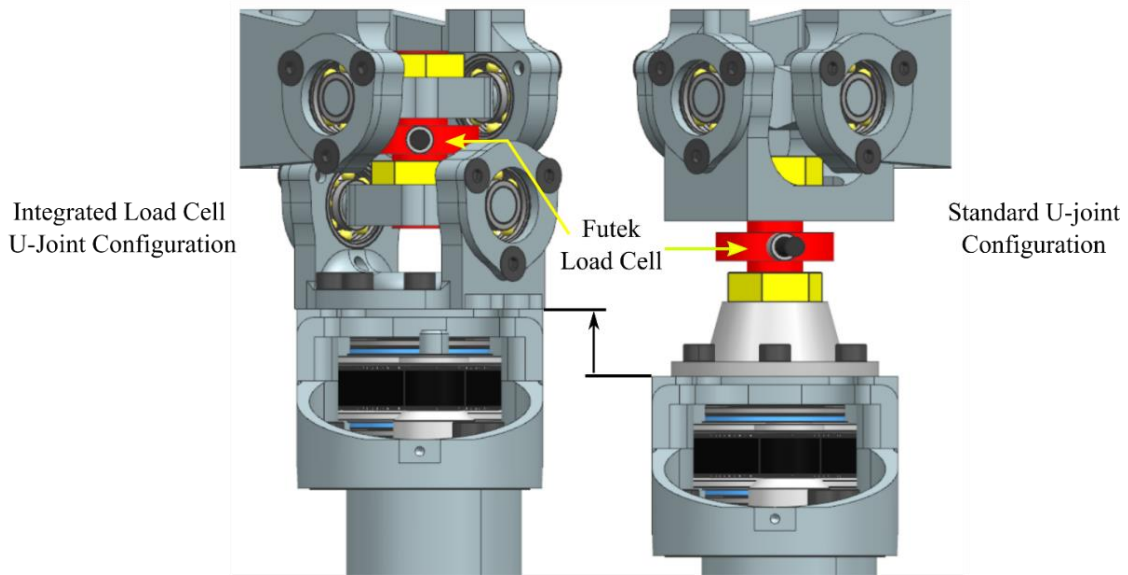


Figure 65: Load Cell Integrate Into U-Joint for Reduced Length [40]

As the design of the cooling jacket evolved, several prototypes were produced. The earliest design of the jacket was 3-D printed for fitment testing and then machined from Aluminum. These aluminum jackets were assembled and leak tested. After several days of pressurized testing and several months of sitting filled with water, no leaks were detected. Since then, the design of the jacket has been modified to reduce weight and integrate directly into the housing. These jackets were designed with the mindset that the final product could be machined or 3D printed. If the aluminum jacket with fins shows no increase in cooling effectiveness, the jackets should be made from a lighter material to save weight. In this case, it is recommended the cooling jacket components be machined from Delrin®. This material can be easily machined, withstands temperatures up to 120°C, and has high rigidity. The jackets could also be 3-D printed, but several issues must be explored first. The printed material should be capable of handling high temperatures and chemically resistant to water additives such as ethylene glycol. One potential material candidate that meets these criteria is Teflon™. Another issue with 3D printing is the rough surface finish produced by the layering processes. This surface finish may affect the performance of the gaskets and O-rings. Extensive leak testing will be required to ensure this surface finish has no effect on seal performance.

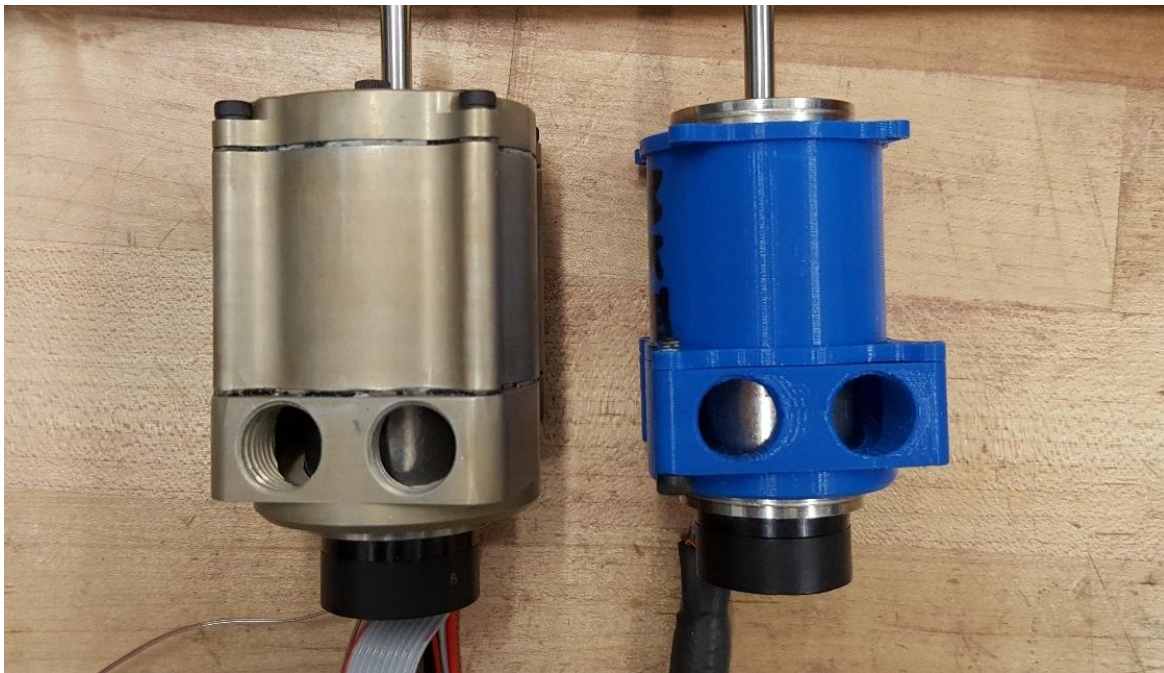


Figure 66: Early Aluminum Prototype (Left) Finalized Design Prototype (Right)

6.2. Future Work

While large strides have been made since the invention of the SEA, there are still many avenues of research and improvements to be explored. This includes further enhancements in the performance of and control of SEA's. To validate the performance of the LSEA's discussed in this thesis; the custom test stand seen in Figure 67 was developed. This test stand also allows the actuators, power electronic, sensors, and controls software to be tested independent of the exoskeleton. The test stand utilizes many of the same features used on the pervious stand to conduct the system identification earlier generation of actuators [42]. The test stand can be configured to support a variety of experiments and test configurations.



Figure 67: Custom Actuator Test Stand with MKIII Lite Mounted

Another area of further exploration is the use of liquid cooled motors for robotics. There are very few papers that discuss the use of OTS motors retrofitted with liquid cooling for use in robotics, and fewer still that discuss the effectiveness or experimental results of liquid cooled motors. While the current housing design may be adequate, the performance of the motor can likely be significantly increased with further refinement of the cooling jacket through testing. In order to experimentally determine the effectiveness of the cooling jacket, a custom motor test stand was developed. This test stand, shown in Figure 68, includes a custom built dynamometer and liquid-cooling system. The dynamometer utilizes a large brushless DC motor as a brake. This motor is mounted inside a large cross-roller bearing that allows it to freely rotate. A lever arm is mounted to the motor and a Futek load cell, so the output torque of the motor can be measure directly. The

cooling system incorporates numerous sensors, allowing the full system performance to be characterized. This includes sensors to measure air temperatures, motor surface temperature, fluid inlet/outlet temperatures, power consumption, flow rate, and pressure drop across the cooling jacket. These metrics will not only characterize the performance of the cooling system but also give insight into the scalability of the cooling system as more motors are placed on the same cooling loop. The data gathered from this test stand will greatly further the understanding of the advantages and limitations of retrofitted liquid cooled motors for robotic applications.

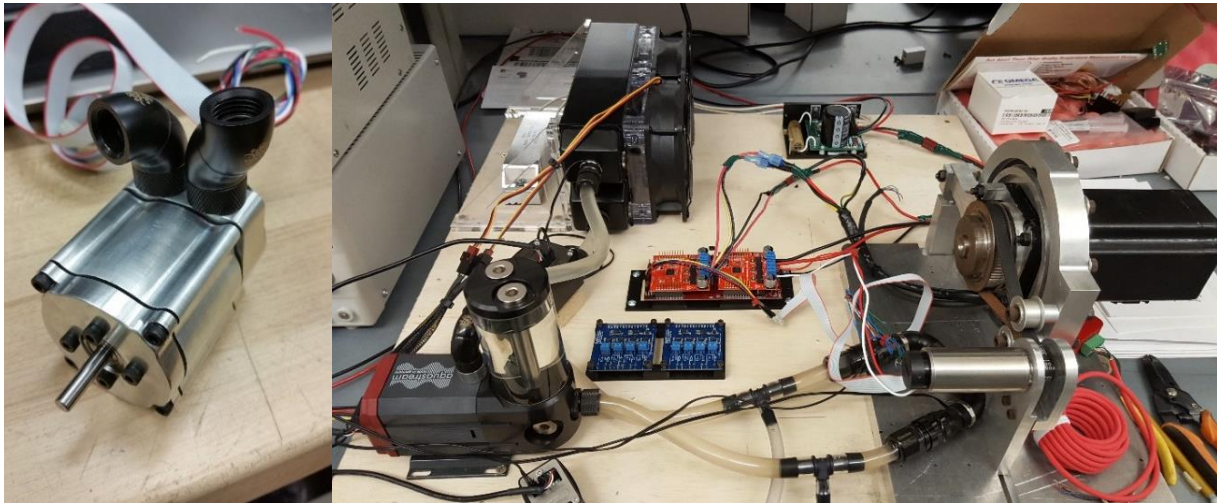


Figure 68: Custom Motor Dynamometer and Liquid Cool Jacket Test Stand

Finally, further analyses can be conducted on the leaf springs to gain a more comprehensive understanding of the spring's performance. While the stresses induced in the leaf springs were analyzed, the fatigue life of the spring was not. The springs will be constantly subjected to cyclical loading that can lead to weakening of the spring material. This weakening is the result of localized failures that can lead to crack initiation, crack growth, and finally failure. Further refinements can be made to the design of the spring if the estimated fatigue life is found to be lower than desired.

References

- [1] H. Kazerooni, “Exoskeletons for human power augmentation,” in *2005 IEEE/RSJ International Conference on Intelligent Robots and Systems*, 2005, pp. 3459–3464.
- [2] “HULC™ | Berkeley Robotics & Human Engineering Laboratory.” [Online]. Available: <http://bleex.me.berkeley.edu/research/exoskeleton/hulc/>. [Accessed: 14-Jan-2018].
- [3] S. Karlin, “Raytheon Sarcos’s Exoskeleton Nears Production,” *IEEE Spectrum: Technology, Engineering, and Science News*, 29-Jul-2011. [Online]. Available: <https://spectrum.ieee.org/at-work/innovation/raytheon-sarcoss-exoskeleton-nears-production>. [Accessed: 14-Jan-2018].
- [4] “Lokomat®,” *Hocoma*. [Online]. Available: <https://www.hocoma.com/us/solutions/lokomat/>. [Accessed: 14-Jan-2018].
- [5] “Rex Bionics - Step into the future,” *Rex Bionics*. [Online]. Available: <https://www.rexbionics.com/>. [Accessed: 13-Jan-2018].
- [6] “ReWalk™ Personal 6.0,” *ReWalk – More Than Walking*. [Online]. Available: <http://rewalk.com/rewalk-personal-3/>. [Accessed: 14-Jan-2018].
- [7] A. Tsukahara, Y. Hasegawa, and Y. Sankai, “Gait support for complete spinal cord injury patient by synchronized leg-swing with HAL,” in *2011 IEEE/RSJ International Conference on Intelligent Robots and Systems*, 2011, pp. 1737–1742.
- [8] “Products,” *Ekso Bionics*. [Online]. Available: <https://eksobionics.com/ekshealth/products/>. [Accessed: 14-Jan-2018].
- [9] “NSCISC Application.” [Online]. Available: <https://www.nscisc.uab.edu/>. [Accessed: 21-Feb-2018].
- [10] J. Wall and T. Colley, “Preventing pressure ulcers among wheelchair users: preliminary comments on the development of a self-administered risk assessment tool,” *J. Tissue Viability*, vol. 13, no. 2, p. 48–50, 52–54, 56 passim, Apr. 2003.
- [11] H. K. Uthoff and Z. F. Jaworski, “Bone loss in response to long-term immobilisation,” *Bone Jt. J.*, vol. 60–B, no. 3, pp. 420–429, Aug. 1978.
- [12] E. G. Pearson, P. W. Nance, W. D. Leslie, and S. Ludwig, “Cyclical etidronate: Its effect on bone density in patients with acute spinal cord injury,” *Arch. Phys. Med. Rehabil.*, vol. 78, no. 3, pp. 269–272, Mar. 1997.
- [13] A. Esquenazi, M. Talaty, A. Packel, and M. Saulino, “The ReWalk powered exoskeleton to restore ambulatory function to individuals with thoracic-level motor-complete spinal cord injury,” *Am. J. Phys. Med. Rehabil.*, vol. 91, no. 11, pp. 911–921, Nov. 2012.
- [14] K. A. Curtis, G. A. Drysdale, R. D. Lanza, M. Kolber, R. S. Vitolo, and R. West, “Shoulder pain in wheelchair users with tetraplegia and paraplegia,” *Arch. Phys. Med. Rehabil.*, vol. 80, no. 4, pp. 453–457, Apr. 1999.
- [15] M. Vukobratovic, D. Hristic, and Z. Stojiljkovic, “Development of active anthropomorphic exoskeletons,” *Med. Biol. Eng.*, vol. 12, no. 1, pp. 66–80, Jan. 1974.
- [16] K. Gilbert, “Exoskeleton prototype project: Final report on phase I.” General Electric Company, U.S. Department of Commerce, National Technical Information Service, 1966.
- [17] Y. Sankai, “Leading Edge of Cybernetics: Robot Suit HAL,” in *2006 SICE-ICASE International Joint Conference*, 2006, p. P-1-P-2.

- [18] Y. Sankai, "HAL: Hybrid Assistive Limb Based on Cybernetics," in *Robotics Research*, Springer, Berlin, Heidelberg, 2010, pp. 25–34.
- [19] H. Kawamoto and Y. Sankai, "Comfortable power assist control method for walking aid by HAL-3," in *IEEE International Conference on Systems, Man and Cybernetics*, 2002, vol. 4, p. 6 pp. vol.4-.
- [20] H. Kawamoto and Y. Sankai, "Power assist method based on phase sequence driven by interaction between human and robot suit," in *RO-MAN 2004. 13th IEEE International Workshop on Robot and Human Interactive Communication (IEEE Catalog No.04TH8759)*, 2004, pp. 491–496.
- [21] T. Hayashi, H. Kawamoto, and Y. Sankai, "Control method of robot suit HAL working as operator's muscle using biological and dynamical information," in *2005 IEEE/RSJ International Conference on Intelligent Robots and Systems*, 2005, pp. 3063–3068.
- [22] S. Lee and Y. Sankai, "Power assist control for walking aid with HAL-3 based on EMG and impedance adjustment around knee joint," in *IEEE/RSJ International Conference on Intelligent Robots and Systems*, 2002, vol. 2, pp. 1499–1504 vol.2.
- [23] A. Chu, H. Kazerooni, and A. Zoss, "On the Biomimetic Design of the Berkeley Lower Extremity Exoskeleton (BLEEX)," in *Proceedings of the 2005 IEEE International Conference on Robotics and Automation*, 2005, pp. 4345–4352.
- [24] A. B. Zoss, H. Kazerooni, and A. Chu, "Biomechanical design of the Berkeley lower extremity exoskeleton (BLEEX)," *IEEEASME Trans. Mechatron.*, vol. 11, no. 2, pp. 128–138, Apr. 2006.
- [25] H. Kazerooni, J. L. Racine, L. Huang, and R. Steger, "On the Control of the Berkeley Lower Extremity Exoskeleton (BLEEX)," in *Proceedings of the 2005 IEEE International Conference on Robotics and Automation*, 2005, pp. 4353–4360.
- [26] J. Ghan and H. Kazerooni, "System identification for the Berkeley lower extremity exoskeleton (BLEEX)," in *Proceedings 2006 IEEE International Conference on Robotics and Automation, 2006. ICRA 2006.*, 2006, pp. 3477–3484.
- [27] A. Zoss, H. Kazerooni, and A. Chu, "On the mechanical design of the Berkeley Lower Extremity Exoskeleton (BLEEX)," in *2005 IEEE/RSJ International Conference on Intelligent Robots and Systems*, 2005, pp. 3465–3472.
- [28] K. Amundson, J. Raade, N. Harding, and H. Kazerooni, "Hybrid hydraulic-electric power unit for field and service robots," in *2005 IEEE/RSJ International Conference on Intelligent Robots and Systems*, 2005, pp. 3453–3458.
- [29] G. Colombo, M. Wirz, and V. Dietz, "Driven gait orthosis for improvement of locomotor training in paraplegic patients," *Spinal Cord*, vol. 39, no. 5, pp. 252–255, May 2001.
- [30] "[Parker Indego." [Online]. Available: <http://www.indego.com/indego/en/Indego-Personal>. [Accessed: 14-Jan-2018].
- [31] A. J. Kozlowski, T. N. Bryce, and M. P. Dijkers, "Time and Effort Required by Persons with Spinal Cord Injury to Learn to Use a Powered Exoskeleton for Assisted Walking," *Top. Spinal Cord Inj. Rehabil.*, vol. 21, no. 2, pp. 110–121, 2015.
- [32] Y. He, D. Eguren, T. P. Luu, and J. L. Contreras-Vidal, "Risk management and regulations for lower limb medical exoskeletons: a review," *Med. Devices Auckl. NZ*, vol. 10, pp. 89–107, May 2017.
- [33] J. L. Contreras-Vidal and R. G. Grossman, "NeuroRex: A clinical neural interface roadmap for EEG-based brain machine interfaces to a lower body robotic exoskeleton," in *2013 35th*

- Annual International Conference of the IEEE Engineering in Medicine and Biology Society (EMBC)*, 2013, pp. 1579–1582.
- [34] “ARKE™ :: Bionik Laboratories Corp. (BNKL).” [Online]. Available: <https://www.bioniklabs.com/research-development/arke>. [Accessed: 14-Jan-2018].
- [35] “Phoenix | suitX.” [Online]. Available: <http://www.suitx.com/phoenix>. [Accessed: 14-Jan-2018].
- [36] D. Lahr, V. Orekhov, B. Lee, and D. Hong, “Early Developments of a Parallely Actuated Humanoid, SAFFiR,” p. V06BT07A054, Aug. 2013.
- [37] D. Lahr, “Design and control of a bipedal robot.” Ph.D. dissertation, Virginia Polytechnic Institute and State University, 2014.
- [38] V. Orekhov, D. Lahr, B. Lee, and D. Hong, “Configurable Compliance for Series Elastic Actuators,” p. V06BT07A021, Aug. 2013.
- [39] B. K. T.-S. Lee, “Design of a Humanoid Robot for Disaster Response,” Thesis, Virginia Tech, 2014.
- [40] C. S. Knabe, “Design of Linear Series Elastic Actuators for a Humanoid Robot,” Thesis, Virginia Tech, 2015.
- [41] C. Knabe, B. Lee, V. Orekhov, and D. Hong, “Design of a Compact, Lightweight, Electromechanical Linear Series Elastic Actuator,” p. V05BT08A014, Aug. 2014.
- [42] V. L. Orekhov, “Series Elasticity in Linearly Actuated Humanoids,” Jan. 2015.
- [43] V. L. Orekhov, C. S. Knabe, M. A. Hopkins, and D. W. Hong, “An unlumped model for linear series elastic actuators with ball screw drives,” in *2015 IEEE/RSJ International Conference on Intelligent Robots and Systems (IROS)*, 2015, pp. 2224–2230.
- [44] C. S. Knabe, V. Orekhov, M. A. Hopkins, B. Y. Lattimer, and D. W. Hong, “Two configurations of series elastic actuators for linearly actuated humanoid robots with large range of motion,” in *2014 IEEE-RAS International Conference on Humanoid Robots*, 2014, pp. 1096–1096.
- [45] C. Knabe *et al.*, “Design of a series elastic humanoid for the DARPA Robotics Challenge,” in *2015 IEEE-RAS 15th International Conference on Humanoid Robots (Humanoids)*, 2015, pp. 738–743.
- [46] C. Knabe *et al.*, “Team VALOR’s ESCHER: A Novel Electromechanical Biped for the DARPA Robotics Challenge,” *J. Field Robot.*, vol. 34, no. 5, pp. 912–939, Aug. 2017.
- [47] J. M. Seminatore, “Upper Body Design of a Humanoid Robot for the DARPA Robotics Challenge,” Thesis, Virginia Tech, 2016.
- [48] G. A. Pratt and M. M. Williamson, “Series elastic actuators,” in *Proceedings 1995 IEEE/RSJ International Conference on Intelligent Robots and Systems. Human Robot Interaction and Cooperative Robots*, 1995, vol. 1, pp. 399–406 vol.1.
- [49] D. W. Robinson, J. E. Pratt, D. J. Paluska, and G. A. Pratt, “Series elastic actuator development for a biomimetic walking robot,” in *1999 IEEE/ASME International Conference on Advanced Intelligent Mechatronics (Cat. No.99TH8399)*, 1999, pp. 561–568.
- [50] J. Pratt, B. Krupp, and C. Morse, “Series elastic actuators for high fidelity force control,” *Ind. Robot*, vol. 29, no. 3, pp. 234–241, Jun. 2002.
- [51] J. Pratt and B. T. Krupp, “Series Elastic Actuators for legged robots,” *Proc. SPIE - Int. Soc. Opt. Eng.*, Sep. 2004.
- [52] J. W. Hurst, A. A. Rizzi, and D. Hobbelen, “Series Elastic Actuation: Potential and Pitfalls.” International Conference on Climbing and Walking Robots, 2004.

- [53] H. Herr, “The effect of series elasticity on actuator power and work output: Implications for robotic and prosthetic joint design,” *MIT Media Lab*. [Online]. Available: <https://www.media.mit.edu/publications/the-effect-of-series-elasticity-on-actuator-power-and-work-output-implications-for-robotic-and-prosthetic-joint-design/>. [Accessed: 15-Jan-2018].
- [54] N. Paine and L. Sentis, “A new prismatic series elastic actuator with compact size and high performance,” in *2012 IEEE International Conference on Robotics and Biomimetics (ROBIO)*, 2012, pp. 1759–1766.
- [55] N. Paine, S. Oh, and L. Sentis, “Design and Control Considerations for High-Performance Series Elastic Actuators,” *IEEEASME Trans. Mechatron.*, vol. 19, no. 3, pp. 1080–1091, Jun. 2014.
- [56] J. Pratt and B. Krupp, “Design of a bipedal walking robot,” presented at the Unmanned Systems Technology X, 2008, vol. 6962, p. 69621F.
- [57] E. CHAI MIN-WUI, “Rotary elastic actuator,” Thesis, 2004.
- [58] K. Kong, J. Bae, and M. Tomizuka, “A Compact Rotary Series Elastic Actuator for Human Assistive Systems,” *IEEEASME Trans. Mechatron.*, vol. 17, no. 2, pp. 288–297, Apr. 2012.
- [59] D. Accoto, G. Carpino, F. Sergi, N. L. Tagliamonte, L. Zollo, and E. Guglielmelli, “Design and Characterization of a Novel High-Power Series Elastic Actuator for a Lower Limb Robotic Orthosis,” *Int. J. Adv. Robot. Syst.*, vol. 10, no. 10, p. 359, Oct. 2013.
- [60] G. A. Day, “Synthesis and Design of a Bimodal Rotary Series Elastic Actuator,” Thesis, Virginia Tech, 2016.
- [61] S. Wolf and G. Hirzinger, “A new variable stiffness design: Matching requirements of the next robot generation,” in *2008 IEEE International Conference on Robotics and Automation*, 2008, pp. 1741–1746.
- [62] J. W. Hurst, J. E. Chestnutt, and A. A. Rizzi, “The Actuator With Mechanically Adjustable Series Compliance,” *IEEE Trans. Robot.*, vol. 26, no. 4, pp. 597–606, Aug. 2010.
- [63] B. Vanderborght *et al.*, “Variable impedance actuators: A review,” *Robot. Auton. Syst.*, vol. 61, no. 12, pp. 1601–1614, Dec. 2013.
- [64] C.-M. Chew, G.-S. Hong, and W. Zhou, “Series damper actuator: a novel force/torque control actuator,” in *4th IEEE/RAS International Conference on Humanoid Robots, 2004.*, 2004, vol. 2, p. 533–546 Vol. 2.
- [65] M. Laffranchi, N. Tsagarakis, and D. G. Caldwell, “A compact compliant actuator (CompAct #x2122;) with variable physical damping,” in *2011 IEEE International Conference on Robotics and Automation*, 2011, pp. 4644–4650.
- [66] S. A. Migliore, E. A. Brown, and S. P. DeWeerth, “Biologically Inspired Joint Stiffness Control,” in *Proceedings of the 2005 IEEE International Conference on Robotics and Automation*, 2005, pp. 4508–4513.
- [67] D. Kim, O. Campbell, J. Ahn, L. Sentis, and N. Paine, “Investigations of viscoelastic liquid cooled actuators applied for dynamic motion control of legged systems,” in *2017 IEEE-RAS 17th International Conference on Humanoid Robotics (Humanoids)*, 2017, pp. 710–717.
- [68] R. V. Ham, T. G. Sugar, B. Vanderborght, K. W. Hollander, and D. Lefeber, “Compliant actuator designs,” *IEEE Robot. Autom. Mag.*, vol. 16, no. 3, pp. 81–94, Sep. 2009.
- [69] K. W. Hollander, T. G. Sugar, and D. E. Herring, “Adjustable robotic tendon using a ‘Jack Spring’ trade;,” in *9th International Conference on Rehabilitation Robotics, 2005. ICORR 2005.*, 2005, pp. 113–118.

- [70] A. Krause, “A Compact Series Elastic Actuator for Bipedal Robots with Human-Like Dynamic Performance,” *The Robotics Institute Carnegie Mellon University*. .
- [71] I.-W. Park, J.-Y. Kim, J. Lee, and J.-H. Oh, “Mechanical design of humanoid robot platform KHR-3 (KAIST Humanoid Robot 3: HUBO),” in *5th IEEE-RAS International Conference on Humanoid Robots, 2005.*, 2005, pp. 321–326.
- [72] H. Lee and Y. Choi, “A New Actuator System Using Dual-Motors and a Planetary Gear,” *IEEEASME Trans. Mechatron.*, vol. 17, no. 1, pp. 192–197, Feb. 2012.
- [73] Y. Ito *et al.*, “Development and verification of life-size humanoid with high-output actuation system,” in *2014 IEEE International Conference on Robotics and Automation (ICRA)*, 2014, pp. 3433–3438.
- [74] J. Urata, Y. Nakanishi, K. Okada, and M. Inaba, “Design of high torque and high speed leg module for high power humanoid,” in *2010 IEEE/RSJ International Conference on Intelligent Robots and Systems*, 2010, pp. 4497–4502.
- [75] J. Falconer, “Japanese Robot SCHAFT Shows Off Its Strong Limbs,” *IEEE Spectrum: Technology, Engineering, and Science News*, 10-Apr-2013. [Online]. Available: <https://spectrum.ieee.org/automaton/robotics/humanoids/japanese-schaft-robot>. [Accessed: 18-Jan-2018].
- [76] N. Paine and L. Sentis, “Design and Comparative Analysis of a Retrofitted Liquid Cooling System for High-Power Actuators,” *Actuators*, vol. 4, no. 3, pp. 182–202, Aug. 2015.
- [77] J. Urata, T. Hirose, Y. Namiki, Y. Nakanishi, I. Mizuuchi, and M. Inaba, “Thermal control of electrical motors for high-power humanoid robots,” in *2008 IEEE/RSJ International Conference on Intelligent Robots and Systems*, 2008, pp. 2047–2052.
- [78] J. Perry, S. T. K, and J. R. Davids, “Gait Analysis: Normal and Pathological Function,” *J. Pediatr. Orthop.*, vol. 12, no. 6, p. 815, Dec. 1992.
- [79] C. L. Vaughan, B. L. Davis, and J. C. O’Connor, *Dynamics of human gait*. Human Kinetics Publishers, 1992.
- [80] M. Hartmann, F. Kreuzpointner, R. Haefner, H. Michels, A. Schwirtz, and J. P. Haas, “Effects of Juvenile Idiopathic Arthritis on Kinematics and Kinetics of the Lower Extremities Call for Consequences in Physical Activities Recommendations,” *International Journal of Pediatrics*, 2010. [Online]. Available: <https://www.hindawi.com/journals/ijpedi/2010/835984/>. [Accessed: 31-Dec-2017].
- [81] C. Mummolo, L. Mangialardi, and J. H. Kim, “Quantifying Dynamic Characteristics of Human Walking for Comprehensive Gait Cycle,” *J. Biomech. Eng.*, vol. 135, no. 9, pp. 091006-091006-10, Jul. 2013.
- [82] C. Lasance, “Technical Data column,” *Electron. Cool.*, Jan. 1997.
- [83] P. H. Oosthuizen and D. Naylor, *An Introduction to Convective Heat Transfer Analysis*. WCB/McGraw Hill, 1999.
- [84] A. S. of H. Engineers Refrigerating and Air-Conditioning, *2001 ASHRAE Handbook: Fundamentals*. ASHRAE, 2001.
- [85] D. O. Stemme and P. Wolf, *Principles and Properties of Highly Dynamic DC Miniature Motors*. Sachseln, Switzerland: Maxon Motor, 1994.
- [86] T. L. Bergman, F. P. Incropera, and A. S. Lavine, *Fundamentals of Heat and Mass Transfer*. John Wiley & Sons, 2011.
- [87] R. C. Juvinall and K. M. Marshek, *Fundamentals of Machine Component Design, 5th Edition*. Wiley Global Education, 2011.

- [88] R. Budynas and K. Nisbett, *Shigley's Mechanical Engineering Design*. McGraw-Hill Education, 2010.
- [89] B. Lee, C. Knabe, V. Orekhov, and D. Hong, "Design of a Human-Like Range of Motion Hip Joint for Humanoid Robots," p. V05BT08A018, Aug. 2014.
- [90] A. De and U. Tasch, "A two-DOF manipulator with adjustable compliance capabilities and comparison with the human finger," *J. Robot. Syst.*, vol. 13, no. 1, pp. 25–34, Jan. 1996.
- [91] T. Morita and S. Sugano, "Design and development of a new robot joint using a mechanical impedance adjuster," in *Proceedings of 1995 IEEE International Conference on Robotics and Automation*, 1995, vol. 3, pp. 2469–2475 vol.3.
- [92] J. Choi, S. Hong, W. Lee, S. Kang, and M. Kim, "A Robot Joint With Variable Stiffness Using Leaf Springs," *IEEE Trans. Robot.*, vol. 27, no. 2, pp. 229–238, Apr. 2011.
- [93] R. J. Wang and H. P. Huang, "AVSER #x2014; Active variable stiffness exoskeleton robot system: Design and application for safe active-passive elbow rehabilitation," in *2012 IEEE/ASME International Conference on Advanced Intelligent Mechatronics (AIM)*, 2012, pp. 220–225.
- [94] "Why choose a Machined Spring," *Machined Springs*. [Online]. Available: <http://machinedsprings.com/why-choose-a-machined-spring/>. [Accessed: 19-Jan-2018].
- [95] "AISI Grade 18Ni (300) Maraging Steel, Aged, sheet, tested transverse, 6 mm." [Online]. Available: <http://www.matweb.com/search/DataSheet.aspx?MatGUID=550702a40aa64761b8296d5fffc47c7>. [Accessed: 20-Jan-2018].
- [96] X. Li, "Structural Design of a 6-DoF Hip Exoskeleton using Linear Series Elastic Actuators," Thesis, Virginia Tech, 2017.
- [97] "Titanium Ti-6Al-4V (Grade 5), Annealed." [Online]. Available: <http://www.matweb.com/search/DataSheet.aspx?MatGUID=a0655d261898456b958e5f825ae85390>. [Accessed: 19-Jan-2018].
- [98] J. Brown, "Characterization of MSC/NASTRAN & MSC/ABAQUS Elements for Turbine Engine Blade Frequency Analysis." Proc. MSC Aerospace Users' Conference, 1997.
- [99] S. Selamet and M. Garlock, "Guidelines for modeling three dimensional structural connection models using finite element methods." International Symposium: Steel Structures: Culture & Sustainability, 2010.
- [100] E. Q. Sun, "Shear locking and hourglassing in msc nastran, abaqus, and ansys." Msc software users meeting, 2006.
- [101] "O-Ring Gland Calculator - Engineering Tool for Dynamic Applications | Apple Rubber Products." [Online]. Available: <http://www.applerubber.com/oring-gland-calculator/>. [Accessed: 30-Jan-2018].
- [102] E. Oberg, *Machinery's Handbook, 30th Edition, Toolbox Edition*. Industrial Press, 2016.
- [103] "Bolted Joint Analysis | MechaniCalc." [Online]. Available: <https://mechanicalcalc.com/reference/bolted-joint-analysis>. [Accessed: 31-Jan-2018].
- [104] "Hangzhou Speedway Import & Export Co., Ltd.-Hangzhou Speedway Import & Export Co., Ltd." [Online]. Available: <http://www.cnspeedway.com/>. [Accessed: 03-Feb-2018].

Appendix A

This appendix contains all of the plots generated from the 140 kg human and ESCHER simulations.

Gait Data for Human Hip, Knee, and Ankle

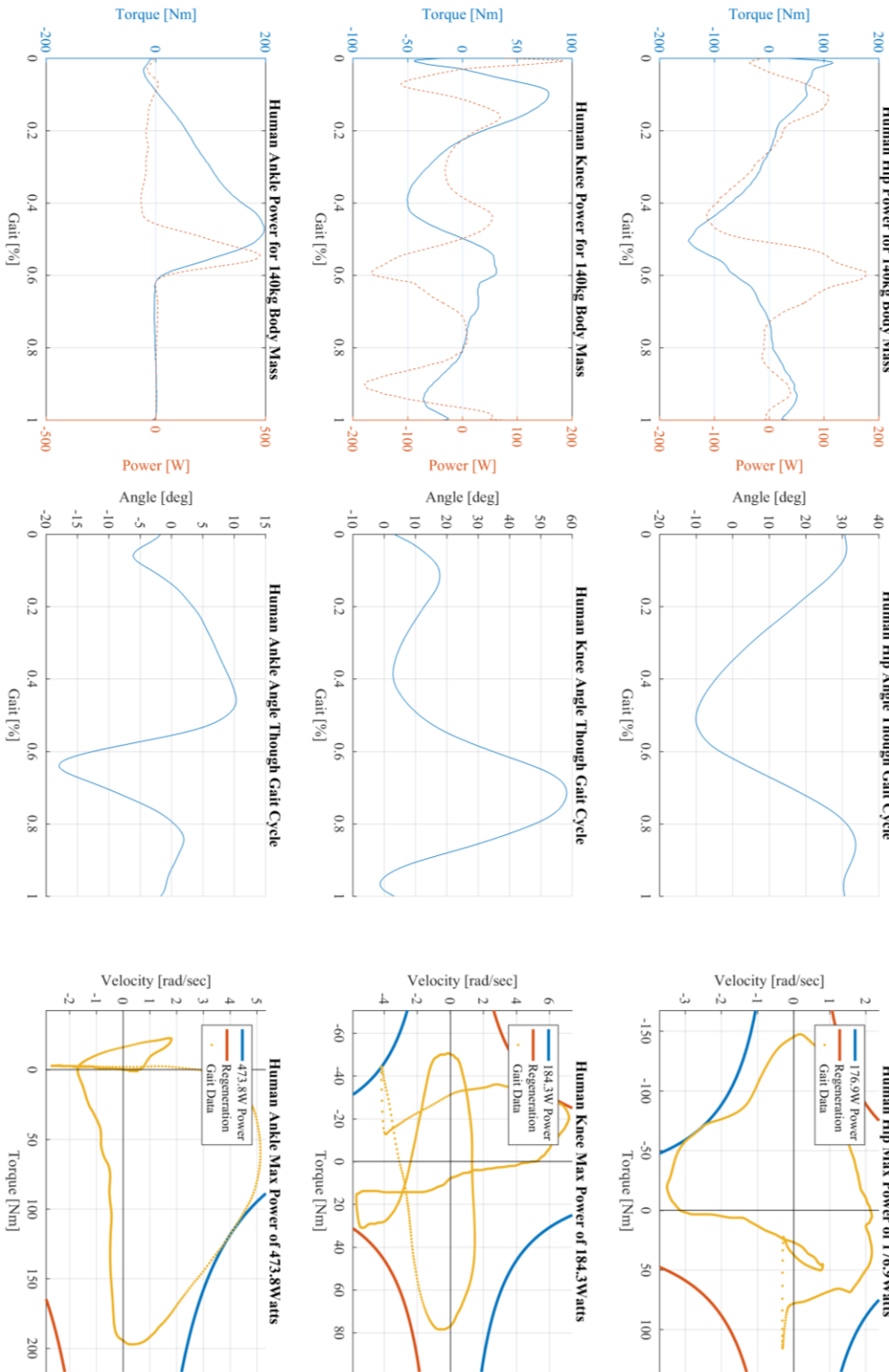


Figure A 1: Summary of Human Gait Data

ESCHER Left Leg Data Walking at 0.48 m/s

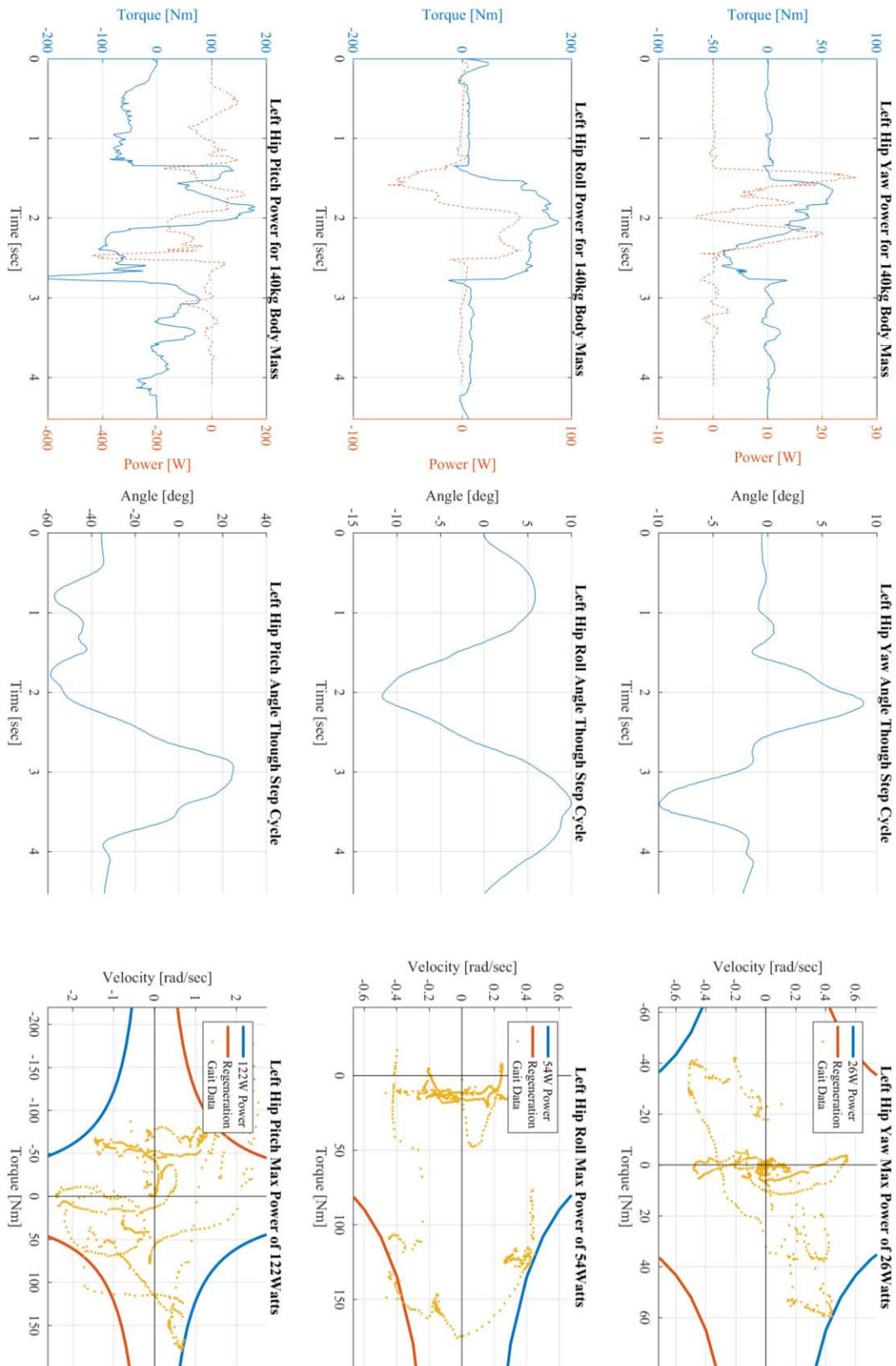


Figure A2: ESCHER Left Leg Data Walking at 0.48 m/s

ESCHER Left Leg Data Walking at 0.48 m/s

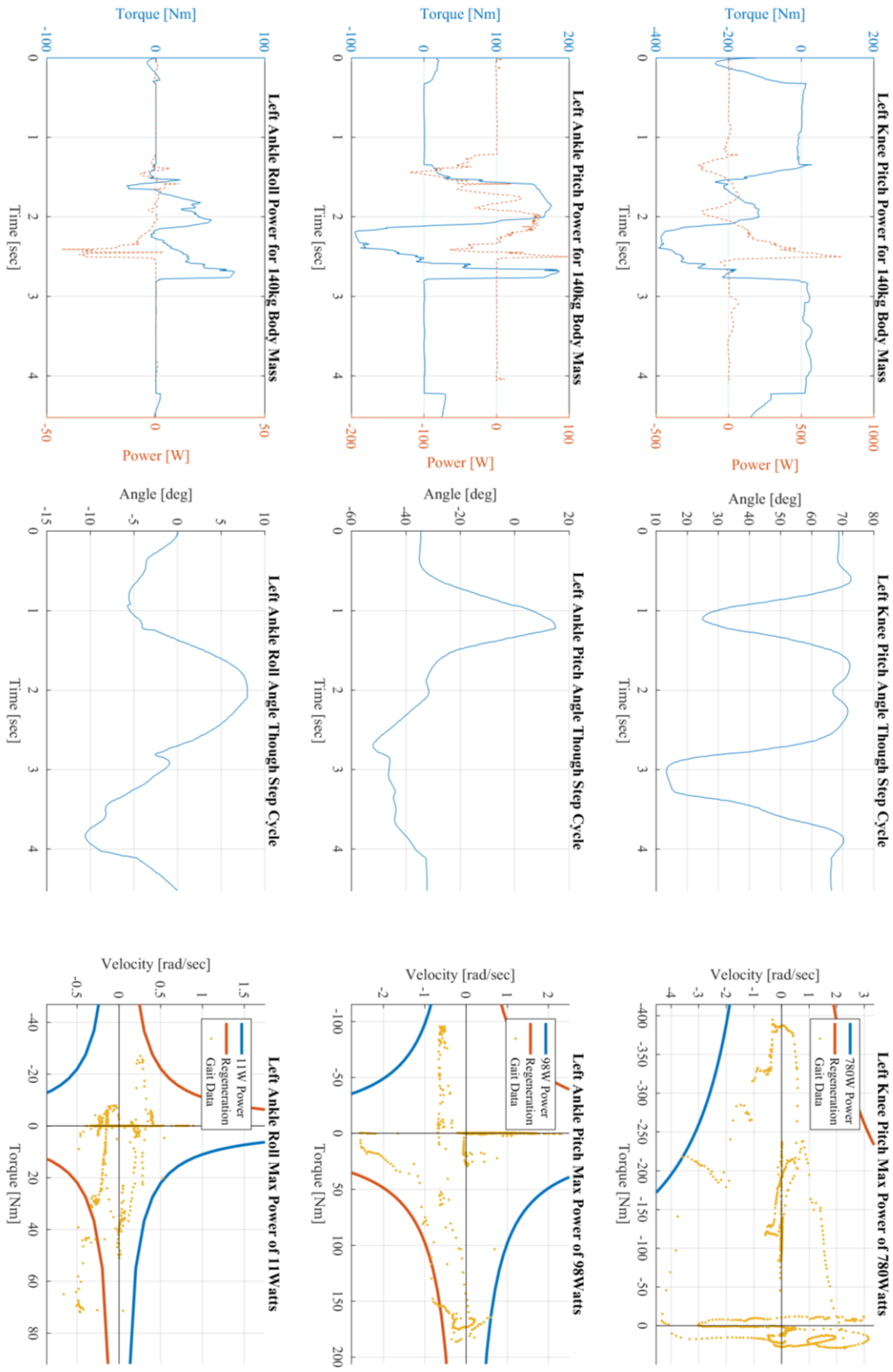


Figure A3: ESCHER Left Leg Data Walking at 0.48 m/s

ESCHER Right Leg Data Walking at 0.48 m/s

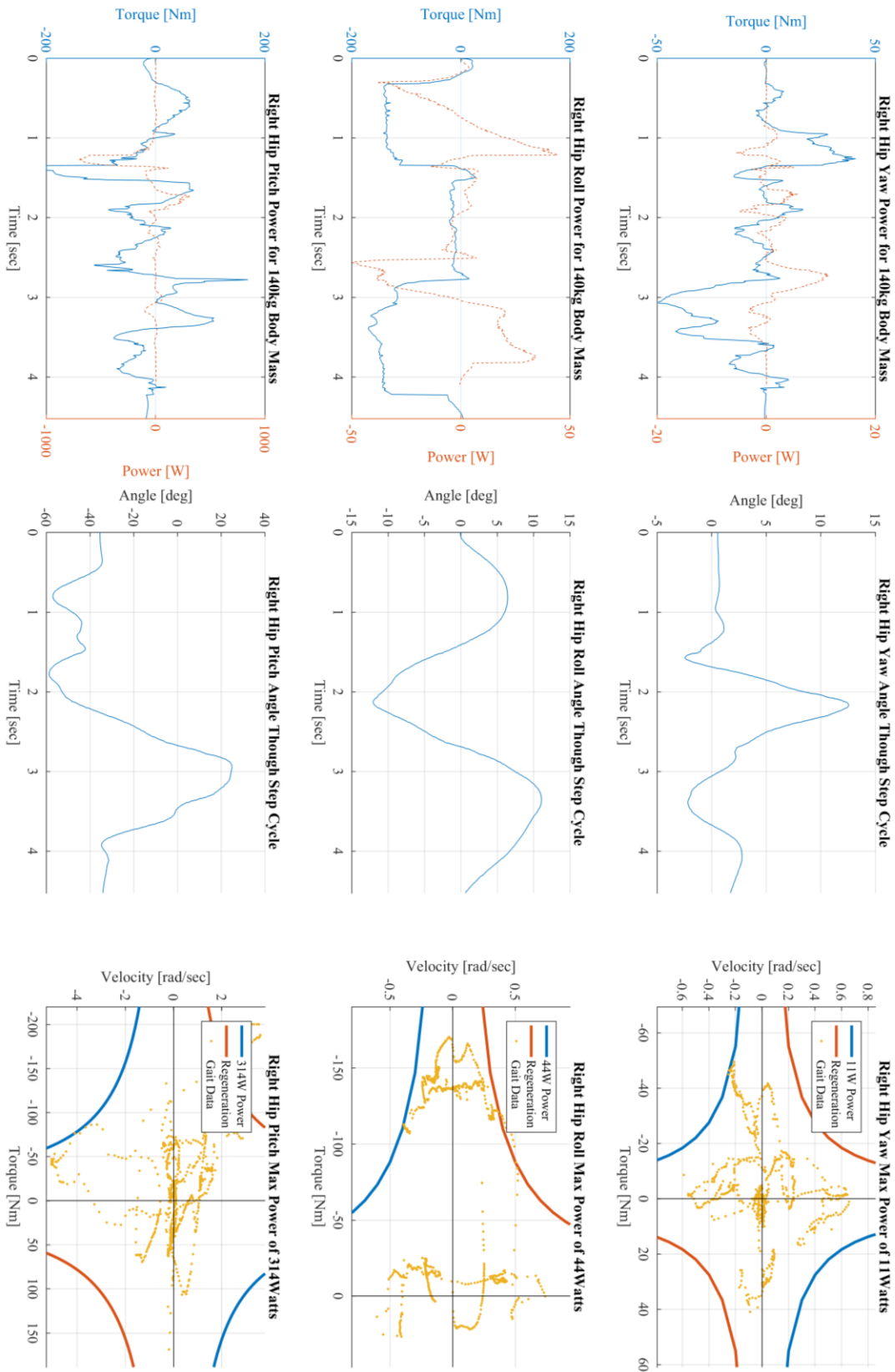


Figure A4: ESCHER Right Leg Data Walking at 0.48 m/s

ESCHER Right Leg Data Walking at 0.48 m/s

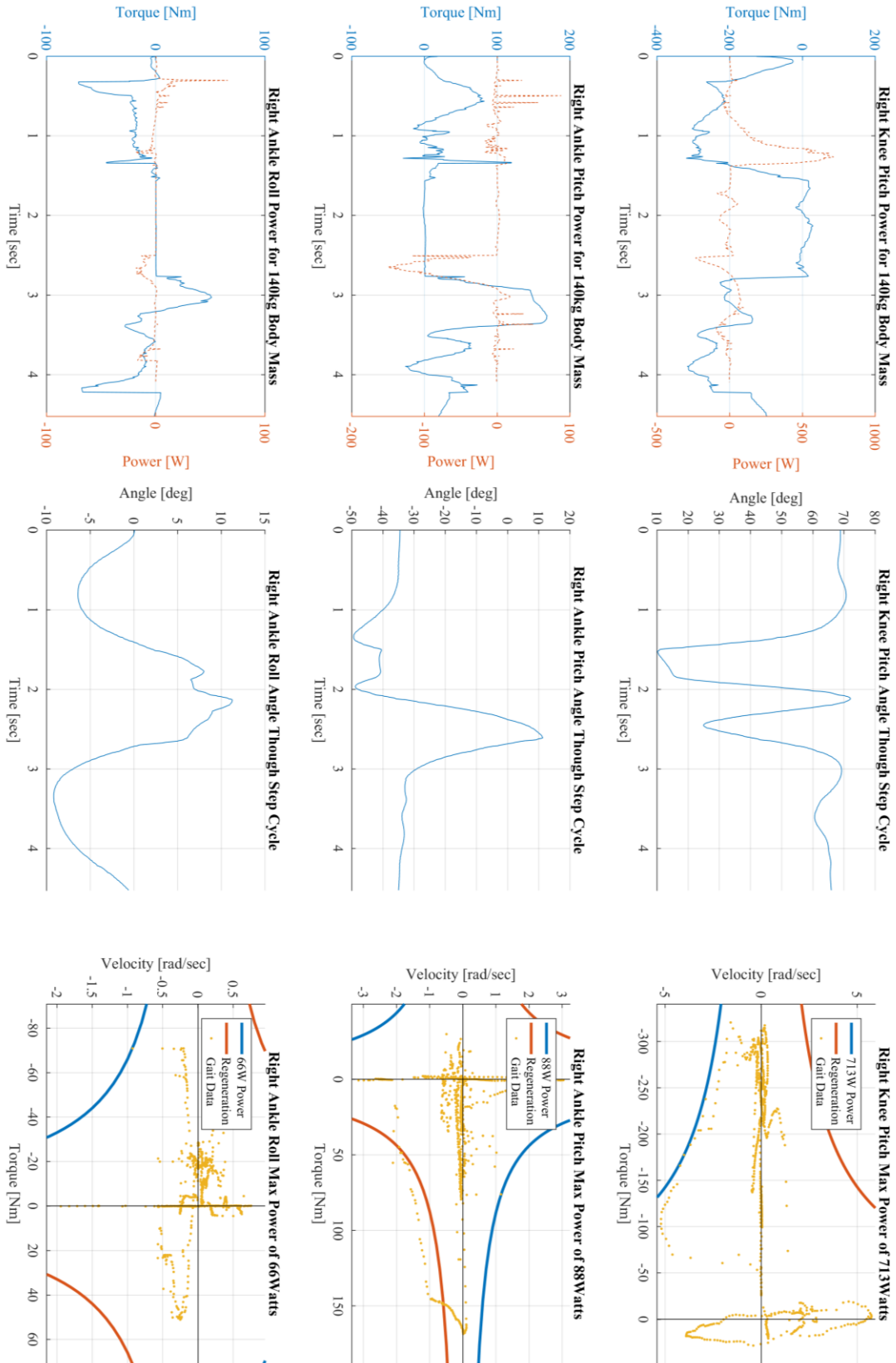


Figure A5: ESCHER Right Leg Data Walking at 0.48 m/s

ESCHER Left Leg Data Walking at 0.20 m/s

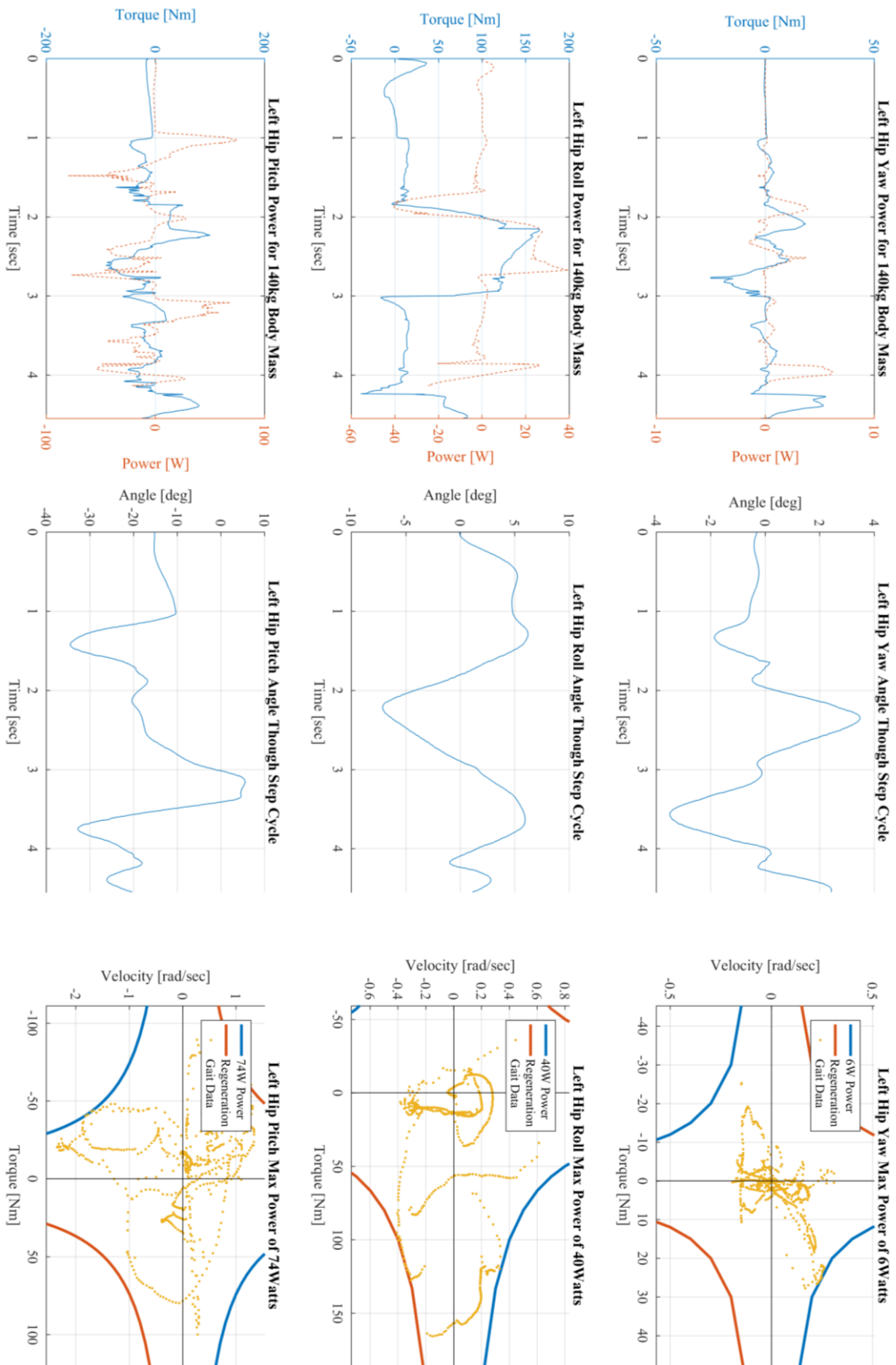


Figure A6: ESCHER Left Leg Data Walking at 0.20 m/s

ESCHER Left Leg Data Walking at 0.20 m/s

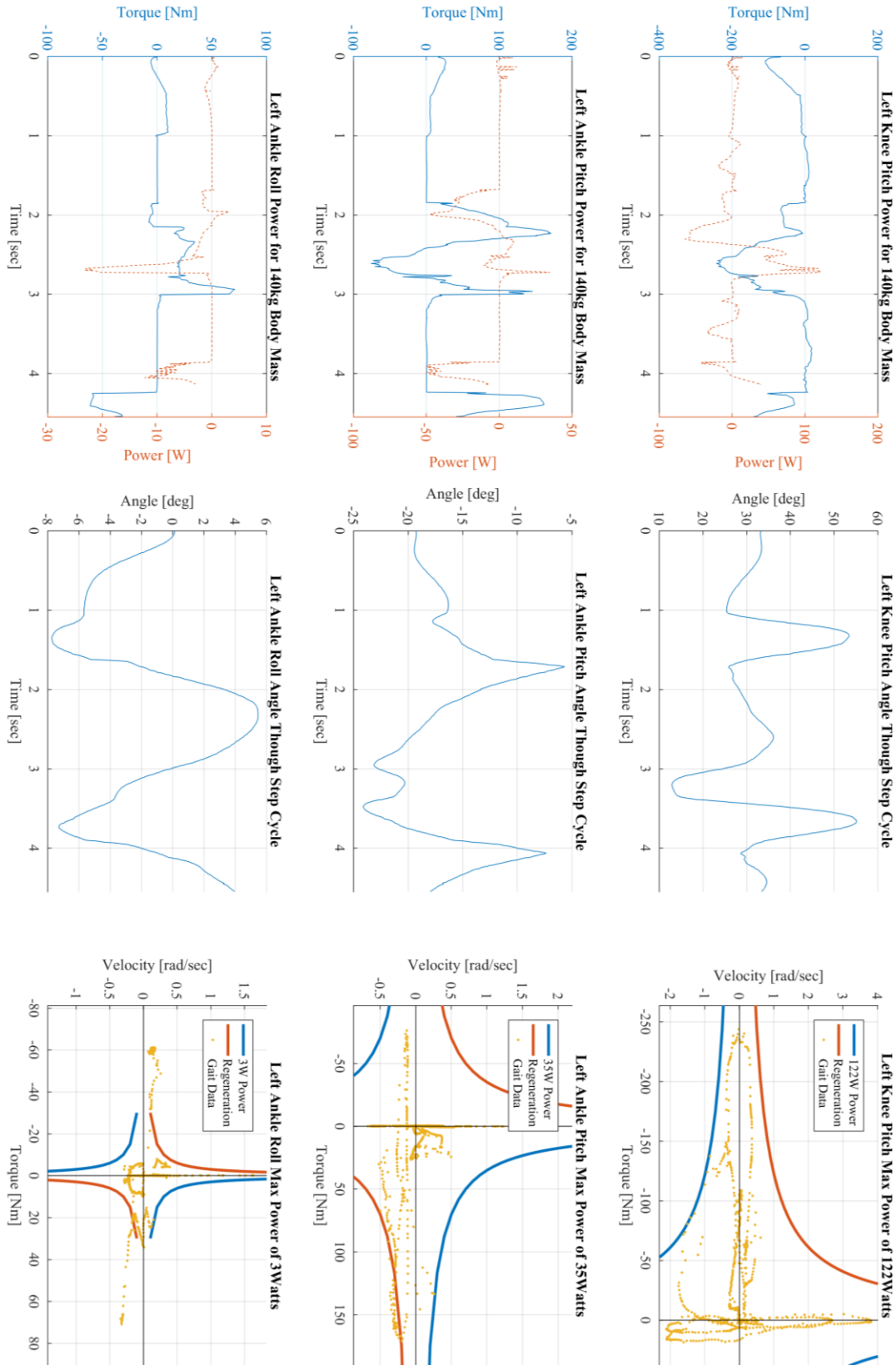


Figure A7: ESCHER Left Leg Data Walking at 0.20 m/s

ESCHER Right Leg Data Walking at 0.20 m/s

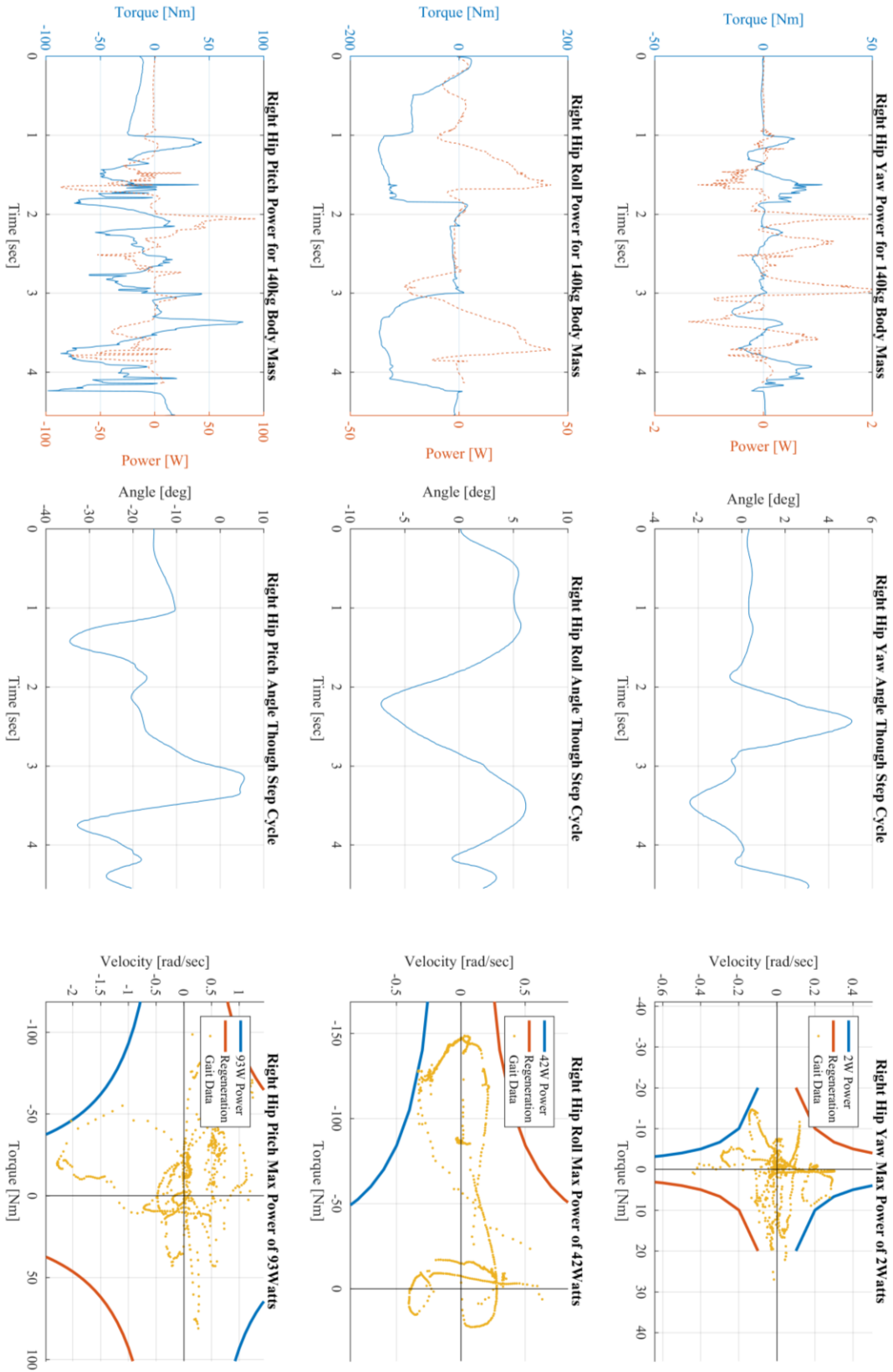


Figure A8: ESCHER Right Leg Data Walking at 0.20 m/s

ESCHER Right Leg Data Walking at 0.20 m/s

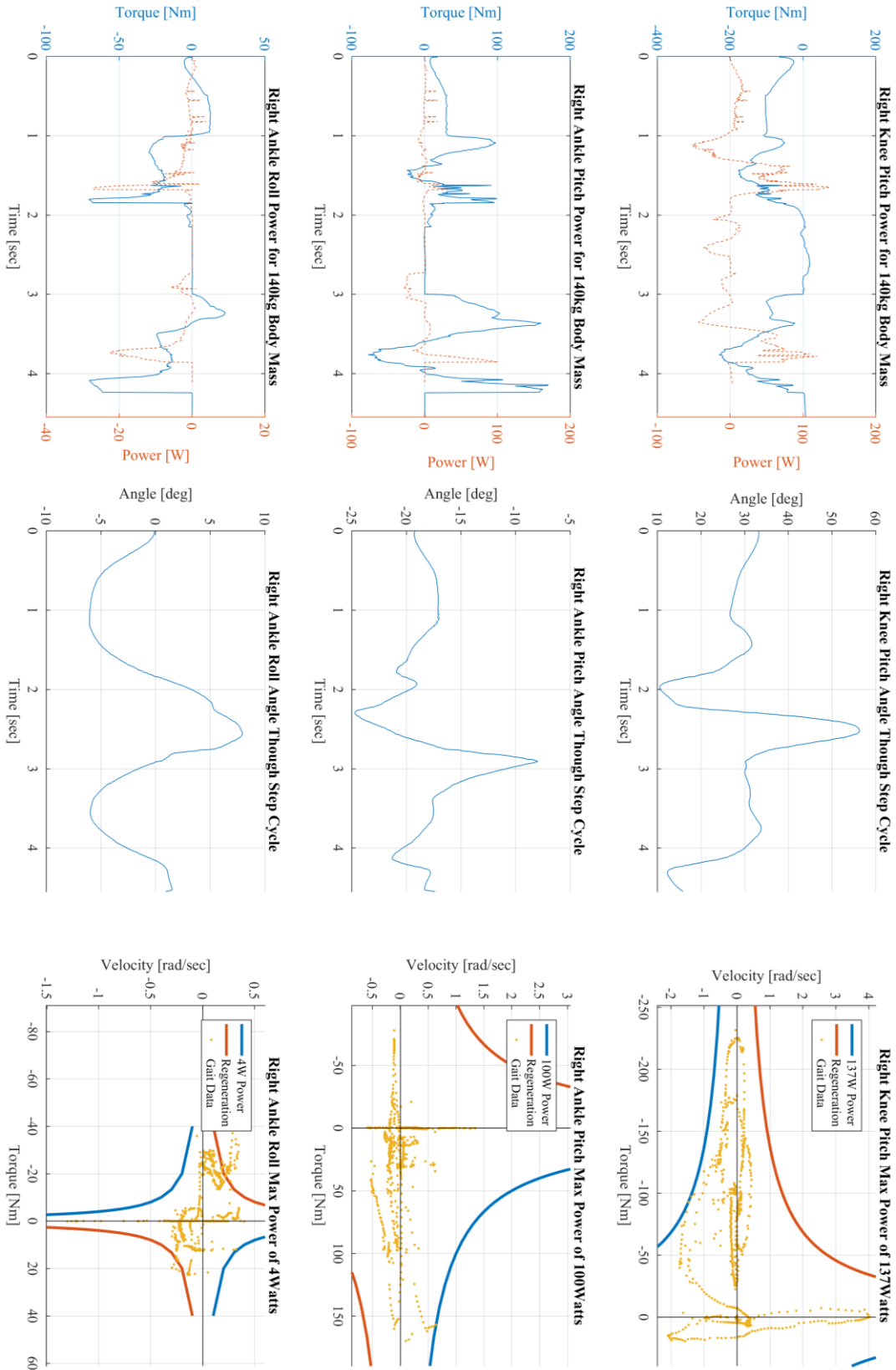


Figure A9: ESCHER Right Leg Data Walking at 0.20 m/s

ESCHER Left Leg Data Walking up Stairs

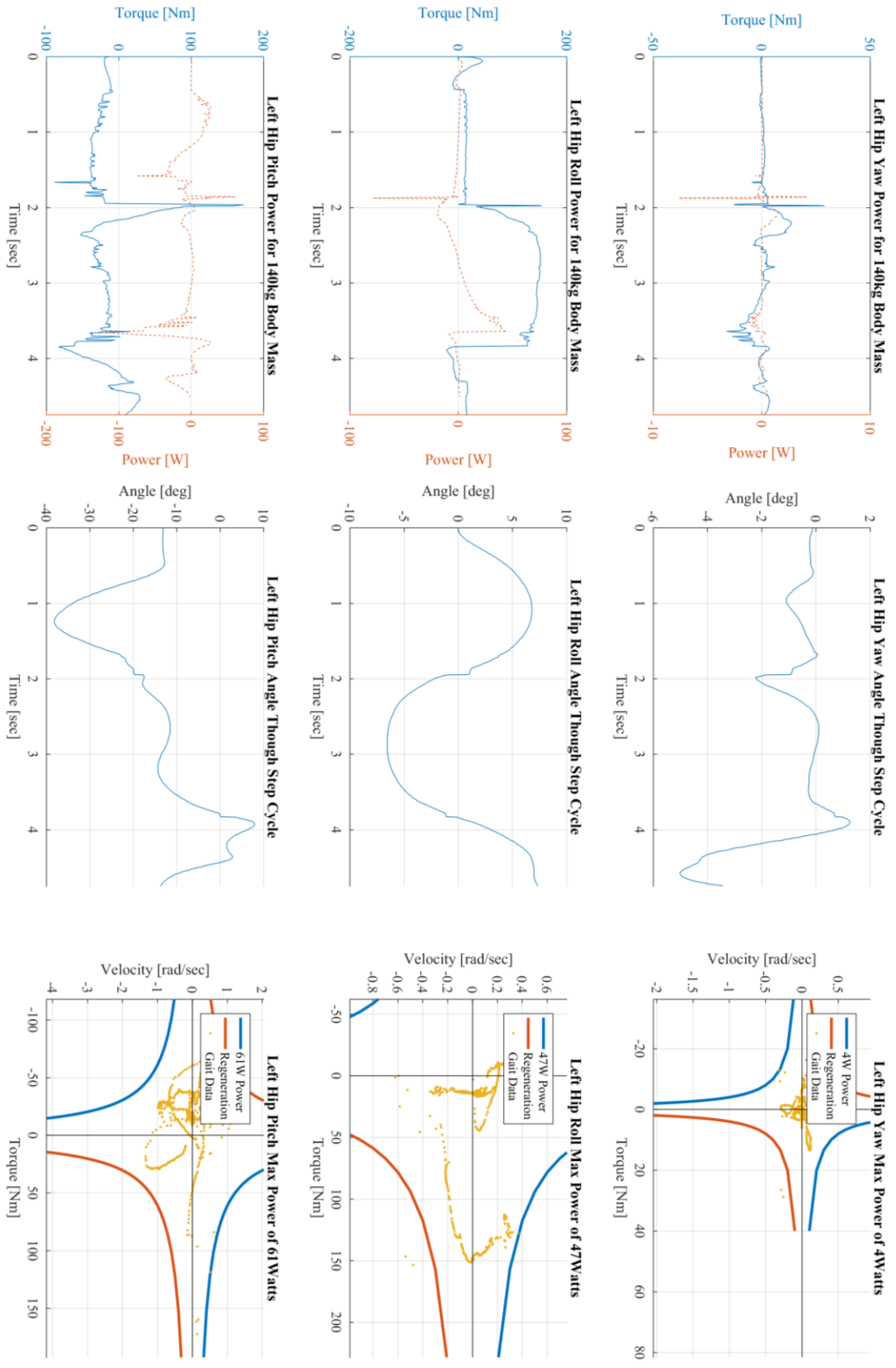


Figure A10: ESCHER Left Leg Data Walking Up Stairs

ESCHER Left Leg Data Walking up Stairs

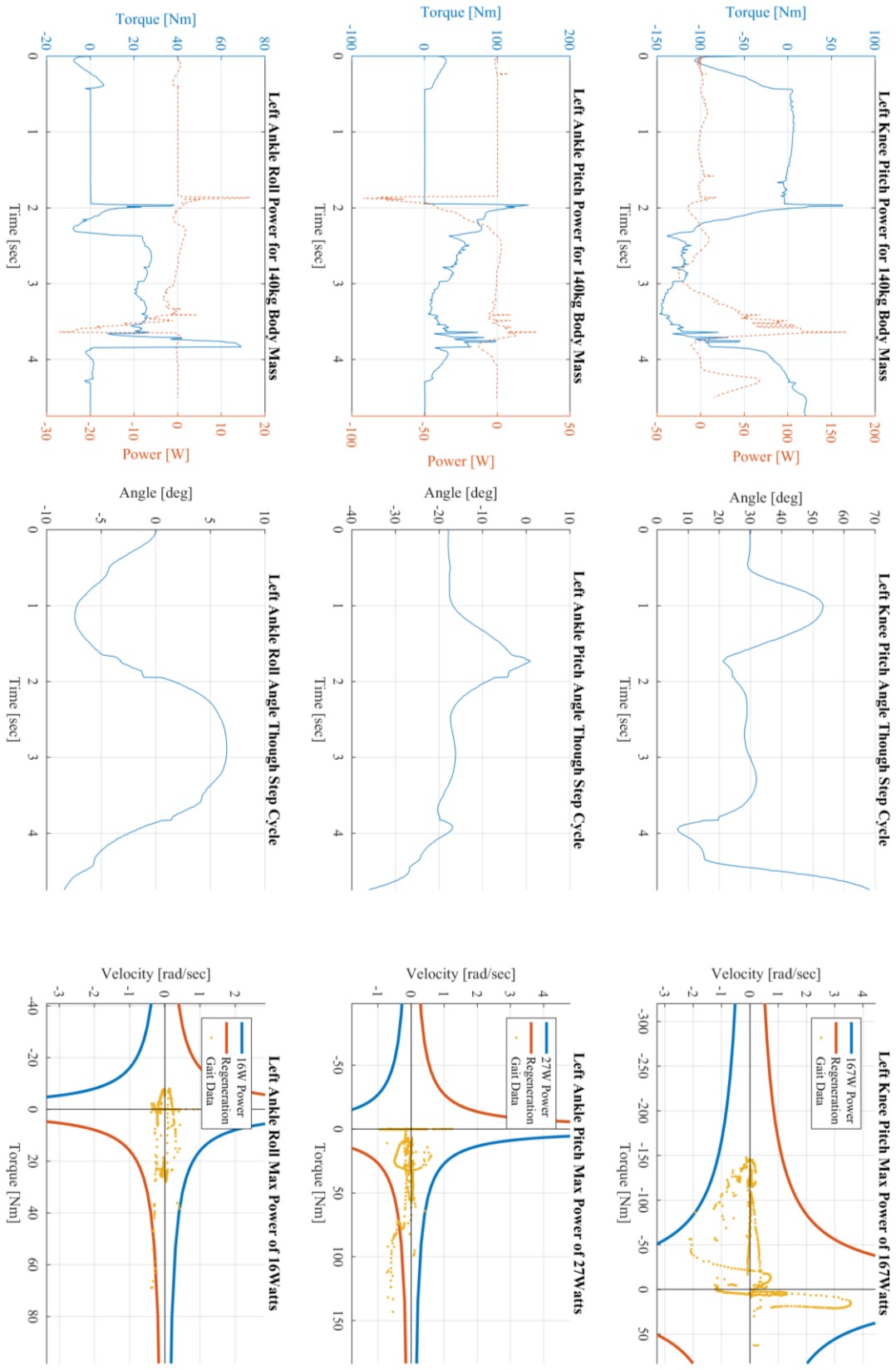


Figure A11: ESCHER Left Leg Data Walking Up Stairs

ESCHER Right Leg Data Walking up Stairs

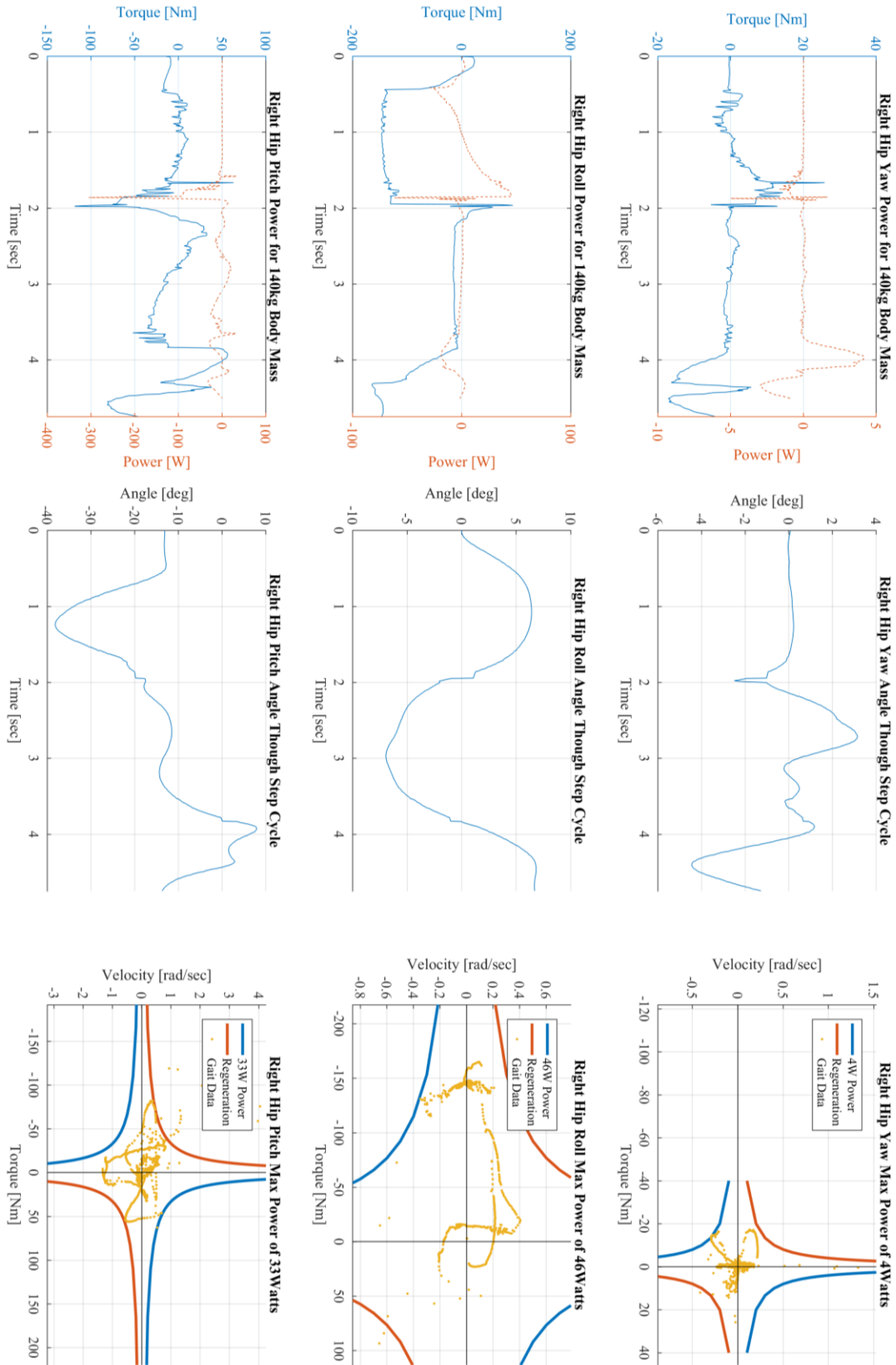


Figure A12: ESCHER Right Leg Data Walking Up Stairs

ESCHER Right Leg Data Walking up Stairs

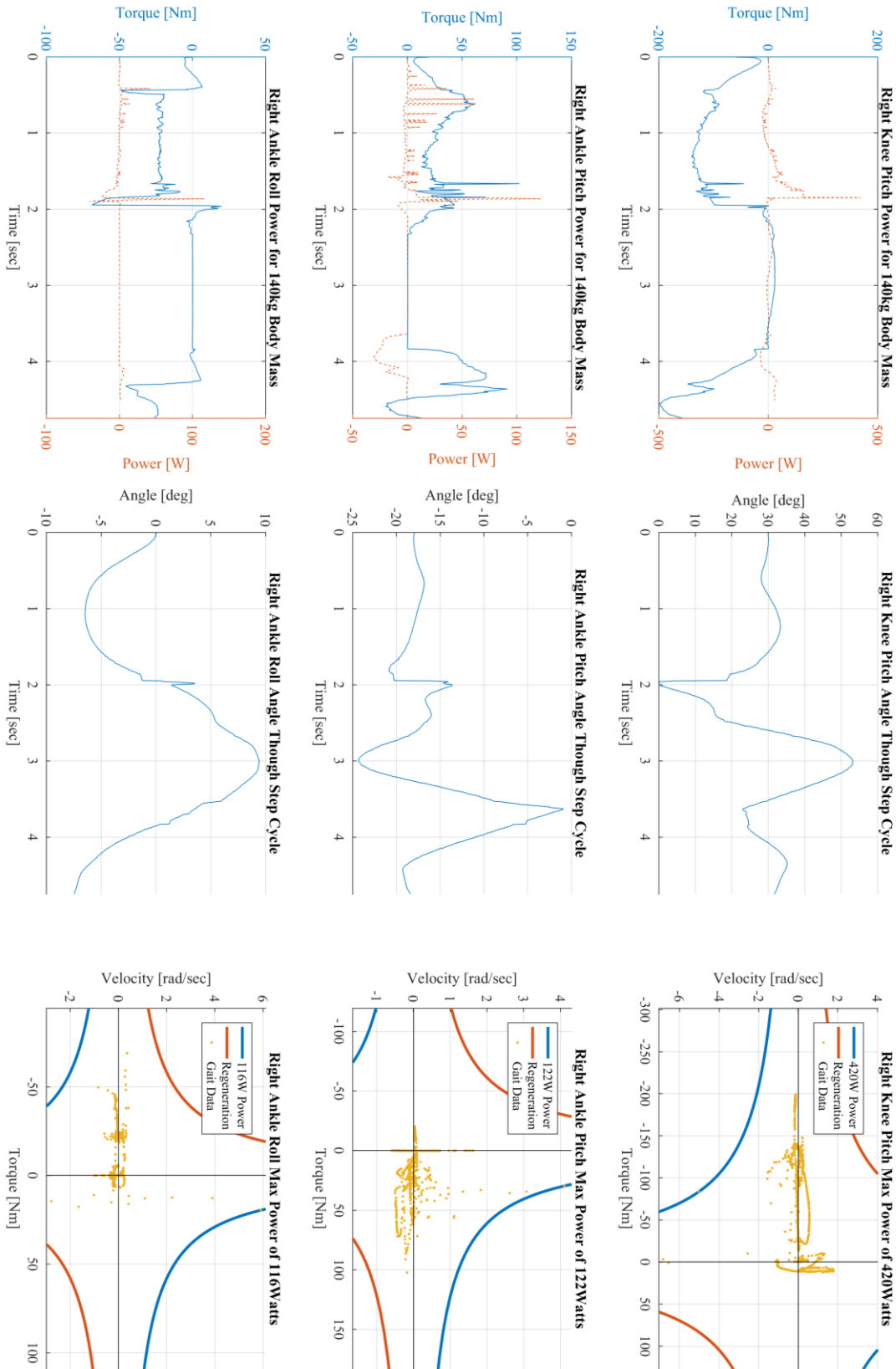


Figure A13: ESCHER Right Leg Data Walking Up Stairs

Appendix B

This appendix contains all of the peak data points generated from the 140 kg Human [78] and ESCHER data. The ESCHER simulations included walking at 0.48m/s, 0.20m/s, and up stairs.

Table B1: 140kg Human Gait Peak Power and Corresponding Values

Joint Name	Peak Power [W]	Torque @ Peak [Nm]	Velocity @ Peak [rad/s]
Human Hip	161.45	-72.91	2.36
Human Knee	160.26	30.92	5.36
Human Ankle	515.92	138.85	-3.22

Table B2: 140kg Human Gait Peak Torque and Corresponding Values

Joint Name	Peak Torque [Nm]	Velocity @ Peak [rad/s]	Power @ Peak [W]
Human Hip	147.41	-0.18	-21.81
Human Knee	78.41	0.65	-53.65
Human Ankle	197.17	-0.33	130.26

Table B3: 140kg Human Gait Peak Velocity and Corresponding Values

Joint Name	Peak Velocity [rad/s]	Torque @ Peak [Nm]	Power @ Peak [W]
Human Hip	3.51	-19.29	79.47
Human Knee	7.17	-20.77	-100.20
Human Ankle	5.13	60.01	261.86

Table B4: Peak Power, 140kg ESCHER Walking at 0.48 m/s

Joint	Peak Power [W]	Torque @ Peak [Nm]	Velocity @ Peak [rad/s]
Left Hip Yaw	26.22	59.50	0.44
Left Hip Roll	69.06	148.85	-0.46
Left Hip Pitch	439.21	-194.63	2.26
Left Knee	780.04	-217.48	-3.59
Left Ankle Pitch	120.09	148.03	-0.81
Left Ankle Roll	43.09	65.04	-0.66
Right Hip Yaw	11.49	-46.39	-0.25
Right Hip Roll	49.89	-106.12	0.47
Right Hip Pitch	707.48	-200.00	3.54
Right Knee	713.17	-177.26	-4.02
Right Ankle Pitch	150.41	142.18	-1.06
Right Ankle Roll	65.75	-70.83	-0.93

Table B5: Peak Torque, 140kg ESCHER Walking at 0.48 m/s

Joint	Peak Torque [Nm]	Velocity @ Peak [rad/s]	Power @ Peak [W]
Left Hip Yaw	59.63	0.42	25.33
Left Hip Roll	175.80	-0.03	-5.07
Left Hip Pitch	200.00	2.08	-415.87
Left Knee	394.66	-0.33	130.53
Left Ankle Pitch	186.25	-0.25	-47.43
Left Ankle Roll	71.96	-0.46	-33.42
Right Hip Yaw	49.42	-0.21	10.45
Right Hip Roll	170.24	-0.03	4.65
Right Hip Pitch	200.00	2.96	-592.64
Right Knee	320.26	-1.59	510.29
Right Ankle Pitch	168.62	0.01	1.74
Right Ankle Roll	70.83	-0.93	65.75

Table B6: Peak Velocity, 140kg ESCHER Walking at 0.48 m/s

Joint	Peak Velocity [rad/s]	Torque @ Peak [Nm]	Power @ Peak [W]
Left Hip Yaw	0.54	-1.56	-0.84
Left Hip Roll	0.48	-15.68	-7.48
Left Hip Pitch	2.54	-109.00	-276.50
Left Knee	4.34	-6.45	27.99
Left Ankle Pitch	2.58	-0.21	0.54
Left Ankle Roll	1.55	0.05	0.07
Right Hip Yaw	0.65	1.13	0.74
Right Hip Roll	0.74	0.19	0.14
Right Hip Pitch	5.08	-43.97	223.26
Right Knee	5.74	-3.44	-19.74
Right Ankle Pitch	3.15	0.79	-2.50
Right Ankle Roll	1.95	0.18	-0.35

Table B7: Peak Power, 140kg ESCHER Walking at 0.20 m/s

Joint	Peak Power [W]	Torque @ Peak [Nm]	Velocity @ Peak [rad/s]
Left Hip Yaw	6.20	25.03	0.25
Left Hip Roll	73.30	141.74	-0.52
Left Hip Pitch	80.28	-72.89	1.10
Left Knee	121.83	-85.85	-1.42
Left Ankle Pitch	77.69	57.48	1.35
Left Ankle Roll	28.97	69.43	-0.42
Right Hip Yaw	4.80	-20.98	-0.23
Right Hip Roll	42.26	-128.06	-0.33
Right Hip Pitch	92.79	-45.62	-2.03
Right Knee	136.59	-92.88	-1.47
Right Ankle Pitch	138.74	100.76	1.38
Right Ankle Roll	27.23	-69.15	0.39

Table B8: Peak Torque, 140kg ESCHER Walking at 0.20 m/s

Joint	Peak Torque [Nm]	Velocity @ Peak [rad/s]	Power @ Peak [W]
Left Hip Yaw	27.76	0.17	4.64
Left Hip Roll	165.91	-0.15	-25.59
Left Hip Pitch	100.01	0.28	27.80
Left Knee	243.60	-0.02	5.38
Left Ankle Pitch	171.03	-0.20	-33.87
Left Ankle Roll	70.94	-0.12	-8.72
Right Hip Yaw	27.00	-0.02	-0.43
Right Hip Roll	148.45	0.03	-3.99
Right Hip Pitch	98.49	0.15	-15.08
Right Knee	231.51	-0.04	9.88
Right Ankle Pitch	169.95	0.10	16.74
Right Ankle Roll	71.02	0.32	-22.94

Table B9: Peak Velocity, 140kg ESCHER Walking at 0.20 m/s

Joint	Peak Velocity [rad/s]	Torque @ Peak [Nm]	Power @ Peak [W]
Left Hip Yaw	0.37	0.11	-0.04
Left Hip Roll	0.63	23.43	14.78
Left Hip Pitch	2.35	-20.24	47.66
Left Knee	3.81	0.34	1.28
Left Ankle Pitch	1.99	0.08	0.15
Left Ankle Roll	1.63	-0.10	-0.17
Right Hip Yaw	0.44	0.78	-0.34
Right Hip Roll	0.66	-15.88	10.45
Right Hip Pitch	2.29	-19.66	44.95
Right Knee	4.01	-0.60	-2.42
Right Ankle Pitch	2.85	-0.09	-0.27
Right Ankle Roll	1.30	0.13	-0.17

Table B 10: Peak Power, 140kg ESCHER Walking Up Stairs

Joint	Peak Power [W]	Torque @ Peak [Nm]	Velocity @ Peak [rad/s]
Left Hip Yaw	21.56	39.92	0.54
Left Hip Roll	78.97	146.65	-0.54
Left Hip Pitch	191.42	-58.75	-3.26
Left Knee	248.47	-227.40	-1.09
Left Ankle Pitch	182.99	100.86	1.81
Left Ankle Roll	78.01	70.20	1.11
Right Hip Yaw	63.62	-93.39	-0.68
Right Hip Roll	67.97	-119.46	0.57
Right Hip Pitch	481.93	200.00	-2.41
Right Knee	420.10	-83.44	-5.03
Right Ankle Pitch	220.29	155.90	-1.41
Right Ankle Roll	116.25	19.71	5.90

Table B 11: Peak Torque, 140kg ESCHER Walking Up Stairs

Joint	Peak Torque [Nm]	Velocity @ Peak [rad/s]	Power @ Peak [W]
Left Hip Yaw	61.60	0.08	5.18
Left Hip Roll	208.50	-0.16	-32.85
Left Hip Pitch	172.57	0.13	22.95
Left Knee	300.00		
Left Ankle Pitch	163.67	0.32	51.84
Left Ankle Roll	78.24	0.17	13.06
Right Hip Yaw	101.87	-0.32	32.80
Right Hip Roll	197.41	0.02	-3.84
Right Hip Pitch	200.00	-2.14	-428.14
Right Knee	281.74	0.01	-2.65
Right Ankle Pitch	163.78	-1.21	-198.13
Right Ankle Roll	89.55	-0.27	-24.14

Table B 12: Peak Velocity, 140kg ESCHER Walking Up Stairs

Joint	Peak Velocity [rad/s]	Torque @ Peak [Nm]	Power @ Peak [W]
Left Hip Yaw	1.85	-0.18	0.34
Left Hip Roll	0.79	6.28	-4.93
Left Hip Pitch	3.98	-29.78	118.39
Left Knee	4.23	22.44	94.83
Left Ankle Pitch	4.60	0.15	0.69
Left Ankle Roll	3.16	-4.32	13.64
Right Hip Yaw	1.33	0.41	0.54
Right Hip Roll	0.66	93.48	-61.52
Right Hip Pitch	4.04	-75.52	-305.27
Right Knee	6.85	-3.10	21.26
Right Ankle Pitch	4.10	29.73	121.86
Right Ankle Roll	5.90	19.71	116.25

Appendix C

	Product #	Voltage(V)	Power (W)	Torque Cont. (Nm)	Torque Peak (Nm)	Rated Speed (rpm)	Width (mm)	Weight (kg)	Size (mm*3)	Cost (\$)
Maxon	353297	48	250	0.746	17.1	3480	65	2.48	760500	\$993.63
	167132	48	400	0.747	11.8	5370	60	2.45	468000	\$989.70
	167131	48	400	0.83	6.82	3100	60	2.45	468000	\$989.70
	136212	48	250	0.316	6.11	10000	45	1.15	205537.5	\$633.90
	136209	48	250	0.347	3.53	5490	45	1.15	205537.5	\$633.90
	305015	48	200	0.093	3.43	16000	30	0.3	57600	\$887.00
	426450	48	240	0.149	0.46	12900	22	0.21	37752	N/A
	393879	48	220	0.339	3.35	6470	32	0.73	145408	\$4,500.00
	397800	48	480	0.961	3.35	6420	32	0.73	145408	\$4,500.00
	BLY342S-48v	48	220	0.71	N/A	3200	85.9	1.85	523157.629	231
Anatehm Automation	BLY343S-48v	48	440	1.33	N/A	3200	85.9	2.6	714268.808	379
	BLY344S-48v	48	660	2.1	N/A	3200	85.9	4	922351.25	536
	BLK321S-48v	48	690	2.07	N/A	3000	80	3.27	846720	358
	BLK322S-48v	48	840	2.67	N/A	3000	80	3.7	941440	462
	BSG34-35AC	28	729	2.1	13.7	3409	86.36	2.1	663766.4144	N/A
	BSG43-35AD-05LHEB	28	875	3.08	13.77	3639	86.36	2.1	976155.7716	2250
	BSG34-35A	28	729	3.13	6.50	3960	86.36	2.1	1119557.658	N/A
	BN42-23AF-02	50	497	1.1	4.3	5950	105.41	1.846	648898.057	N/A
	BN42-33AF-02	50	690	1.9	8.8	4710	105.41	2.95	931124.2668	N/A
	BN42-43AF-02	50	824	2.8	13.5	3840	105.41	4.06	1213350.477	N/A
Framed Moog	BN42-53AF-02	50	861	3.6	18.1	2820	105.41	5.17	1495576.686	N/A
	BN42-53ELU-011H	24	993	3.26	18.7	4520	105	4.2	1488375	685
	BN42-53AD-04CHE	160	1345	4.15	18.6	4774	107.95	5.47	1650151.74	N/A
	BN42-53AE-05CHE	128	2280	5.2	19.9	6352	107.95	5.47	1650151.74	N/A
	5922	48	3000	4.1	7	7000	138	3.3	2218626	1500
	5924	48	5000	8	14	6000	160	3.7	3609600	1500
	RS340CR1	53	N/A	0.98	N/A	3000	68	2	649672	N/A
	RS430FR2	43	N/A	1.3	N/A	2000	83	2.4	933459.5	N/A
	F12M4	43	N/A	0.77	N/A	3000	140	3.85	1401400	N/A
	N/A	48	300	1.05	2.59	3000	N/A	0.467	N/A	700
Frameless Kollmorgen	N/A	48	480	2.42	6.11	3000	N/A	1.05	N/A	700
	N/A	48	1000	4.1	16.1	2640	130	1.79	2163200	700
	BD-3730-B5-1-E5	230	N/A	N/A	1.26	N/A	94.742	0.32	136794.9496	N/A
	BDE-2000-H-1E5	230	N/A	N/A	2.66	N/A	50.8	0.96	222536.3291	N/A
Frameless Moog	BD-2000-H-1E5	230	N/A	N/A	2.66	N/A	50.8	0.94	222536.3291	N/A
	BD-3000-K-1E5	230	N/A	N/A	6.42	N/A	76.2	0.88	316445.1736	1503
	BD-3000-L-1E5	230	N/A	N/A	8.57	N/A	76.2	1.16	395993.4016	1751

Figure C1: Brushless Motor Comparison Table